



**DISSIPATIVE PARTICLE DYNAMICS WITH
PREDETERMINED INPUT PARAMETERS
FOR PARTICULATE SUSPENSIONS**

A Thesis submitted by

THI YEN NGOC NGUYEN

M.S., Applied Mathematics

B.S., Mathematics and Computer Science

For the award of the degree of

Doctor of Philosophy

2021

Abstract

This PhD project reports a new Dissipative Particle Dynamics (DPD) scheme for numerically investigating the behaviour of complex fluids at the mesoscale. Its attractive features include (i) the input parameters are directly determined from the physical fluid properties: the mass density, water compressibility, time-scale ratio, viscosity and dynamic response; and (ii) the transport coefficients are also considered as functions of the wavelengths and frequencies of thermal fluctuations (i.e. generalised hydrodynamics). With its pre-determined input parameters, the proposed DPD is shown to possess a consistent scaling of thermal fluctuations and produce similar behaviours of the flow at different levels of coarse-graining. With its generalised hydrodynamic regime employed, the proposed DPD method is shown to have the ability to model a viscoelastic fluid using a single set of particles, and the ability to take into account size effects caused by suspended objects. Compressibility is also studied, and a simple approach based on the time-scale ratio is proposed and shown to be effective. Improved results have been achieved in the simulation of viscometric and non-viscometric flows of simple (single phase) and complex (multiphase) fluids.

Certification of Thesis

This Thesis is entirely the work of Thi Yen Ngoc NGUYEN except where otherwise acknowledged. The work is original and has not previously been submitted for any other award, except where acknowledged.

Principal Supervisor: Prof. Nam MAI-DUY

Associate Supervisor: Prof. Thanh TRAN-CONG

Student and supervisors signatures of endorsement are held at the University.

Dedicated to

my parents

second parents

family

professors

friends

and a special friend

Acknowledgements

First of all, my special heartfelt thanks go to my amazing supervisors, Prof. Thanh TRAN-CONG and Prof. Nam MAI-DUY, and to Prof. Nhan PHAN-THIEN. Thank you very much for your wholehearted guidance, support, inspiration and encouragement during my doctoral years.

I acknowledge to University of Southern Queensland (USQ), the Faculty of Health, Engineering and Science (HES) and the former Computational Engineering and Science Research Centre (CESRC) for offering me a PhD position with a USQ Postgraduate Research Scholarship. Great thanks go to the Centre for Future Materials (CFM) for offering me a study space in the centre. I also greatly appreciate the invaluable help of the USQ team, as well as the staff of the Graduate Research School (GRS), in particular the Associate Dean (Graduate Research School) and Mr. Charlie Nelson (Graduate Research Student Officer), who have supported me to have chances to extend and complete my PhD program. I am also very grateful to the USQ ICT team for helping me to deal with computer-related issues. And thank you very much to the USQ Security team for being on duty 24/7 to insure security so that I can study with peace of mind, day or night.

Next, I would love to express my deepest heartfelt gratitude to my parents who have the merit of giving birth and nurturing - "A father's goodness is higher than the mountain, a mother's goodness deeper than the sea". Besides, I would also love to send this thankfulness to whom I consider as my second parents, who have always cared to care for, protect and guide me since I first came to Australia.

I would like to send my sincere thanks to all my family, relatives, former professors, domestic and foreign friends, who have always encouraged me through the years. They have supported me so much spiritually. Thanks to their enthusiastic encouragement and help, I have had more much strength and energy to overcome challenges.

Actually, I am very lucky to have you all in my life. Thank you all from the bottom of my heart.

Ngoc T.Y. Nguyen
Toowoomba, QLD 4350, Australia
February 2021

Papers Resulting From The Research

Journal Papers

1. N. Phan-Thien, N. Mai-Duy and T.Y.N. Nguyen. A note on dissipative particle dynamics (DPD) modelling of simple fluids. *Computers and Fluids*, 176:97-108, 2018.

Computers and Fluids: Q1 Journal, H-Index: 98, Impact Factor: 2.399

2. N. Mai-Duy, T.Y.N. Nguyen, K. Le-Cao and N. Phan-Thien. Investigation of particulate suspensions in generalised hydrodynamic dissipative particle dynamics using a spring model. *Applied Mathematical Modelling*, 77:652-662, 2020.

Applied Mathematical Modelling: Q1 Journal, H-Index: 103, Impact Factor: 3.633

3. N. Mai-Duy, N. Phan-Thien, T.Y.N. Nguyen and T. Tran-Cong. Coarse graining, compressibility and thermal fluctuation scaling in Dissipative Particle Dynamics employed with physical input parameters. *Physics of Fluids*, 32(5):053313, 2020.

The editors have considered this paper as one of the journal's best and promoted it as a Featured Article

Physics of Fluids: Q1 Journal, H-Index: 166, Impact Factor: 3.514

Conference Presentation

4. T.Y.N. Nguyen, N. Mai-Duy and T. Tran-Cong. A Dissipative Particle Dynamics Model for Bingham-type Two-phase Flows. *The 2nd International Conference on Advances in Computational Mechanics (ACOME 2017)*, Phu Quoc Island, Vietnam, 02-04 August 2017.

Papers To Be Submitted

5. T.Y.N. Nguyen, N. Mai-Duy, N. Phan-Thien and T. Tran-Cong. DPD modeling of dense colloidal suspensions and yield-stress fluids. *Journal of Rheology*.

Contents

Abstract	i
Certification of Thesis	ii
Dedication	iii
Acknowledgements	iv
Papers Resulting From The Research	vi
List of Figures	xix
List of Tables	xx
Nomenclature	xxi
Abbreviations and Acronyms	xxiii
Chapter 1 Introduction	1
1 Overview	1
1.1 Macroscale	1
1.2 Microscale/Nanoscale	6
1.3 Mesoscale	7
2 Research gap and motivation	9
3 Objectives of the thesis	10
4 Outline of the thesis	11

Chapter 2	DPD for Particulate Suspensions	12
1	Particulate suspensions	12
1.1	Introduction	12
1.2	Numerical modelling of particulate suspensions	13
2	Review of DPD	15
2.1	Brief introduction	15
2.2	Formulation	17
2.2.1	DPD equation	17
2.2.2	Conservative properties	20
2.2.3	Calculation of stress tensor	20
2.2.4	Time scales	21
2.2.5	Input parameters for the original DPD	21
2.2.6	Block diagram for the DPD simulation	23
2.3	Numerical modelling of particulate suspensions	23
2.3.1	Frozen DPD particles based model	24
2.3.2	Single-paricle based model	24
2.3.3	Spring model for suspended particles in DPD	25
2.4	Summary and implication for DPDs	27
Chapter 3	Proposed DPD method in the hydrodynamic limit	28
1	Introduction	29
2	DPD with explicit input parameters	32
3	Coarse graining and scaling	35
3.1	Simple fluids	40
3.2	Particulate suspensions	41
4	Flows of the model fluid at different coarse-graining levels	45
4.1	Double Poiseuille flows	46
4.2	Flow past a periodic square array of fixed cylinders	48

5	Reducing unwanted compressibility effects	54
5.1	The mass approach	54
5.2	The time-scale ratio approach	55
6	Concluding remarks	59
 Chapter 4 Proposed DPD method in generalised hydrodynamics		 60
1	Introduction	61
2	Transverse current autocorrelation functions (TCAFs)	63
3	Analytic solutions for simple shear flows of linear viscoelastic fluids	65
4	Generalised DPD transport coefficients	66
4.1	Newtonian fluids	67
4.2	Linear viscoelastic fluids	69
5	Imposition of fluid properties	71
6	Numerical results	73
6.1	Newtonian fluids	74
6.2	Linear viscoelastic fluids	77
6.2.1	Wavelength- and frequency-dependent transport coefficients	77
6.2.2	Linear viscoelastic effect	80
7	Concluding remarks	85
 Chapter 5 Application of the proposed DPD to particulate suspensions		 87
1	Introduction	88
2	Particulate suspensions	90
2.1	Spring model for suspended particles	91

2.2	Finding a length scale introduced into the solvent system due to the presence of suspended particles	92
2.2.1	Approach 1	92
2.2.2	Approach 2	93
2.2.3	Approach 3: TCAF	93
2.3	Effect of the repulsion coefficient	96
2.4	Numerical results	97
3	Concluding remarks	100
Chapter 6	Conclusion and future work	101
References		104

List of Figures

2.1	Computational processing of a DPD simulation.	23
2.2	A solid particle can be modeled by four constituent particles which are basic DPD particles. The reference sites are supposed to move as a solid body.	25
3.1	Simple fluid with water-like compressibility, $\alpha = 1$, $\eta = 30$ and $\rho = mn = 8$; $L_x \times L_y \times L_z = 15 \times 15 \times 15$; $s = 0.5$; $k_B T = 1$; and $\Delta t = 0.001$: Probability density function (PDF) of v_x of a DPD particle at 3 different coarse-graining levels ($n = \{8, 6, 4\}$; $r_c = \{1, 1.1006, 1.2599\}$; $m = \{1, 4/3, 2\}$). Thermal fluctuations are reduced (variance: 1.0272, 0.7546, 0.5054) with larger particle size.	40
3.2	Suspension with water-like compressibility, $\alpha = 1$, $\eta = 30$ and $\rho = 8$ for the solvent phase; constant volume fraction for the suspended phase; $L_x \times L_y \times L_z = 15 \times 15 \times 15$; $k_B T = 1$; and $\Delta t = 0.001$: Probability density function (PDF) of v_x of a single colloidal particle in the solvent employed at 3 different coarse-graining levels ($n = \{8, 6, 4\}$; $r_c = \{1, 1.1006, 1.2599\}$; $m = \{1, 4/3, 2\}$). Its computed variances are similar (0.1318, 0.1247, 0.1321).	42

3.3	Suspension with the solvent phase: water-like compressibility, $\alpha = 1$, $\eta = 30$, $\rho = mn = 8$ and $S_c = 600$; $L_x \times L_y \times L_z = 15 \times 15 \times 15$; $k_B T = 1$; and $\Delta t = 0.001$: Probability density function (PDF) of v_x of a single colloidal particle employed with 3 different sizes at the same solvent coarse graining level ($n = 8$, $r_c = 1$, $m = 1$). Thermal fluctuations of the colloid are reduced (variance: 0.1790, 0.1109, 0.0912) with its larger size.	43
3.4	Probability density function (PDF) of v_x of a single colloidal particle employed with 3 different sizes at the same solvent coarse graining level by the standard (top) and present (bottom) DPDs. It can be seen that the two methods produce similar behaviours. When the size of the colloidal particle is increased, thermal fluctuations of the colloid are reduced (variance: 0.1643, 0.0867 and 0.0493 for the standard DPD and 0.1661, 0.0812, 0.0492 for the present DPD).	44
3.5	Poiseuille flow: Some typical results by the present DPD at $n = \{8, 6, 4\}$. Theoretical values for velocity and shear stress are also included.	47
3.6	Modelling of the fixed cylinder with the surrounding fluid defined by $\{\eta = 100, n = 8, r_c = 2, m = 0.5, k_B T = 1, \alpha = 1\}$: Reference sites of constituent particles of the cylinder (top), its repulsion force field in the radial direction (middle) and fluid-cylinder radial distribution function at no-flow conditions (bottom). Note that, for both constituent and fluid particles, $F_{ij,C} = 23.96(1 - r/r_c)^{6.67}$	49

3.7	Flows past a periodic array of fixed cylinders: Fluid-fluid (left) and fluid-cylinder (right) radial distribution functions for different number densities at no-flow conditions: By defining the exclusion zone as an area where the RDF values are less than 0.01, the cylinders for different resolutions are of similar sizes (about 0.47), and the fluid particle sizes can be negligible.	50
3.8	Flows past a periodic array of cylinders, $n = 8$: Fluid-fluid (left) and fluid-cylinder (right) radial distribution functions for different imposed body forces $F_e = (0, 0.01, 0.02, \dots, 0.10, 0.12, \dots, 0.30)$. Their sizes are generally well maintained over the range of the body force applied.	51
3.9	Flows past a periodic array of cylinders: Drag forces against the mean flow velocity U for three coarse-graining levels with the body forces imposed as $F_e = (0.01, 0.02, \dots, 0.10, 0.12, \dots, 0.30)$. The three cases have similar behaviours in trend and their values are in better agreement as U is reduced.	52
3.10	Flows past a periodic array of cylinders, $n = 10$: Distribution of the number density in a cell for 3 typical values of the imposed body force ($F_e = 0$ top; $F_e = 0.1$ middle, and $F_e = 0.3$ bottom). Attention is needed with increasing F_e due the effects of compressibility of the model fluid.	53

3.11	Couette flows, $\eta = 100$, $n = 10$, $\Delta t = 0.0001$, $L_x \times L_y = 10 \times 10$, $U = 1$, $r_c = 1.6$, $k_B T = 1$, 100 bins per unit area and 10^6 time steps: Density residual against time-scale ratio for 3 typical values of m . Values of α used are $(10^{-2}, 5 \times 10^{-2}, 10^{-1}, 5 \times 10^{-1}, \dots, 10^2)$. Results with the standard repulsion are also included. Changing the value of α can lead to a significant improvement in the distribution of number density over the flow domain.	56
3.12	Flows past a periodic square of cylinders, $\eta = 100$, $n = 10$, $\Delta t = 0.0001$, $L_x \times L_y = 10 \times 10$, $F_e = 0.3$, $r_c = 1.6$, $k_B T = 1$, 100 bins per unit area and 10^6 time steps: Density residual against time-scale ratio for 3 typical values of m . Values of α used are $(10^{-2}, 5 \times 10^{-2}, 10^{-1}, 5 \times 10^{-1}, \dots, 10^2)$. Results with the standard repulsion are also included. Changing the value of α can lead to a significant improvement in the distribution of number density over the flow domain.	57
3.13	Density residual against time-scale ratio for Couette flows ($U = 1$) and flows past a periodic square array of cylinders ($F_e = 0.3$) with $\eta = 100$, $n = 10$, $\Delta t = 0.0001$, $L_x \times L_y = 10 \times 10$, $r_c = 1.6$, $k_B T = 1$, 100 bins per unit area and 10^6 time steps. Values of α used are $(10^{-2}, 5 \times 10^{-2}, 10^{-1}, 5 \times 10^{-1}, \dots, 10^2)$. The two flows have similar optimal values of α	58
4.1	Newtonian fluids: Calculated values of TCAF and their curve fits (solid lines) by using (4.30) for the four smallest k values.	75
4.2	Newtonian fluids: Several data sets are used for obtaining the viscosity. Its deviation is generally reduced with increasing k value (i.e. top to bottom).	76
4.3	Newtonian fluids: Viscosity as a function of the wave number. . .	76

4.4	Viscoelastic fluids: The decay constant of the relaxation modulus and the viscosity as functions of the wave number. When k decreases, the decay constant has the tendency to increase quickly and is expected to reach its maximum in the hydrodynamic limit. For the shear viscosity η_k , the change is seen to be slow as $k \rightarrow 0$.	78
4.5	Viscoelastic fluids: Storage modulus and viscosity as functions of the frequency for the smallest wave number (i.e. $k = k_1 = 0.4189$). The system responses like a fluid at small values of the frequency (i.e. large observation time scale) and like a solid at large values of the frequency. The storage modulus provides a convenient means of quantifying the level of elasticity of the fluid.	79
4.6	Viscoelastic fluids: Viscosity as a function of the frequency for the first four values of k (i.e. 0.4189, 0.8378, 1.2566 and 1.6755). It can be seen that $\eta' \rightarrow \eta_k$ (i.e. 28.8930, 28.3227, 26.8364, 25.0198) as $\omega \rightarrow 0$ and $\eta' \rightarrow 0$ as $\omega \rightarrow \infty$	79
4.7	Viscoelastic fluids: Storage modulus as a function of the frequency for the first four values of k (i.e. 0.4189, 0.8378, 1.2566 and 1.6755). It can be seen that $G' \rightarrow 0$ as $\omega \rightarrow 0$ and $G' \rightarrow \eta_k/\tau_k$ (i.e. $1.4175 \times 10^3, 1.5283 \times 10^4, 5.0473 \times 10^4, 6.6011 \times 10^4$) as $\omega \rightarrow \infty$. In computing these limit values, the corresponding Maxwell relaxation times are $\tau_k = (2.0383 \times 10^{-2}, 1.8532 \times 10^{-3}, 5.3170 \times 10^{-4}, 3.7902 \times 10^{-4})$.	80

4.8	Viscoelastic fluids: As the wave number k is reduced, the relaxation times τ_k corresponding to different values of the particle diffusion time τ_P apparently converge. At finite k , the obtained results indicate that an increase in τ_P results in a decrease in τ_k . It can also be seen that a change in τ_P can affect the estimated viscosity at the hydrodynamic limit. All cases take $\rho = 4$, $S_c = 500$ and $\eta = 30$	82
4.9	Viscoelastic fluids: As the wave number k is reduced, the relaxation times τ_k corresponding to different values of the imposed (limit) viscosity η apparently converge. At finite k , the obtained results indicate that a decrease in η results in a decrease in τ_k . All cases take $\rho = 4$, $S_c = 500$ and $k_B T = 1$	83
4.10	Viscoelastic fluids: As the wave number k is reduced, the relaxation times τ_k corresponding to different values of the imposed (limit) Schmidt number S_c apparently converge. At finite k , the obtained results indicate that an increase in S_c results in a decrease in τ_k . It can also be seen that a change in S_c can affect the estimated viscosity at the hydrodynamic limit. All cases take $\rho = 4$, $\eta = 30$ and $k_B T = 1$	84
5.1	Solvent phase ($a_{ij} = 3.53$ (water compressibility), $n = 4$, $m = 1$, $k_B T = 1$, $r_c = 1.5$, $\eta = 30$, $S_c = 500$): the viscosity is a decreasing function of the wave number k (or an increasing function of the wavelength $\lambda = 2\pi/k$).	91

5.2	Process of finding a new length scale that is introduced into the solvent system due to the presence of suspended particles. For a given volume fraction, two corresponding systems (one without any spring constraints and the other with some spring constraints as a model for suspension) are considered; they have the same total numbers of the base particles and employ the same associated DPD parameters. The two systems are assumed to represent simple fluids; through the TCAF approach, their viscosities are shown to depend on the wave numbers (wavelengths). Extrapolations are then conducted to obtain the viscosities in the hydrodynamic limit ($k \rightarrow 0$). With springs, the effective length scale of the constrained system is less than the system size L , and its viscosity is seen to be lower. The constrained system in the hydrodynamic limit can be considered as the free system at the wave number (wavelength) that corresponds to the hydrodynamic-limit viscosity of the constrained system. This wavelength is taken as a new length scale in the solvent phase.	94
5.3	Diffusion coefficient against time for several values of the repulsion. For $a_{ij} = (3.53, 6.50)$, the diffusion coefficients are observed to stay constant at large times. For larger a_{ij} , there is some reduction in the coefficient and no significant diffusion at $a_{ij} = 500$	96

5.4	<p>Reduced viscosity by original and generalised hydrodynamic DPD using the same repulsion $a_{ij} = 3.53$ (water compressibility). The latter (TCAF) is seen to have a better performance than the former in the dilute ($\phi \lesssim 0.02$, linear dependence), semi-dilute ($\phi \lesssim 0.25$, visible higher-order effects) and concentrated ($\phi \gtrsim 0.25$, rapid growth) regimes. It appears that the generalised hydrodynamic DPD based on sphere/cube mean distance overestimates the reduced viscosity in every regime. Theoretical results in the dilute regime (Einstein, 1906) and empirical results (Quemada, 1977), which have found widespread application, are also included for comparison purposes.</p>	98
5.5	<p>Reduced viscosity by original and generalised hydrodynamic DPD using the same repulsion $a_{ij} = 6.50$ (a fluid is less compressible than water). The latter (TCAF) is seen to have a better performance than the former in the dilute ($\phi \lesssim 0.02$, linear dependence), semi-dilute ($\phi \lesssim 0.25$, visible higher-order effects) and concentrated ($\phi \gtrsim 0.25$, rapid growth) regimes. It appears that the generalised hydrodynamic DPD based on sphere/cube mean distance overestimates the reduced viscosity in every regime. Theoretical results in the dilute regime (Einstein, 1906) and empirical results (Quemada, 1977), which have found widespread application, are also included for comparison purposes.</p>	99

List of Tables

3.1	Couette flows, $U = 1, \eta = 100, n = 10, r_c = 1.6, k_B T = 1, \alpha = 10, L_x \times L_y = 10 \times 10$, 100 bins per unit area and 10^6 time steps: Comparison of the mean thermal energy of the velocity-Verlet and SETD schemes for $m = 0.01$. The former fails to converge at $\Delta t \geq 2.5 \times 10^{-4}$	55
4.1	Values of the input viscosity and Schmidt number, and the corresponding original DPD parameters for ($m = 1, n = 4, k_B T = 1, r_c = 1.5$).	81
5.1	Effective wavelength of the solvent phase against volume fraction of the suspended phase by the three approaches. Compressibility of the solvent is matched to that of water, i.e. $a_{ij} = 3.53$, and the simulation box is taken as $15 \times 15 \times 15$ (in DPD units).	95
5.2	Effective wave number, wavelength and viscosity of the solvent phase against volume fraction of the suspended phase by the TCAF approach. Compressibility of the solvent is matched to that of water, i.e. $a_{ij} = 3.53$, and the simulation box is taken as $15 \times 15 \times 15$ (in DPD units).	95

Nomenclature

Latin letters

N	number of DPD particles
Pe	Peclet number
Re	Reynolds number
S_c	Schmidt number
a_{ij}	repulsive coefficient between particles i and j
$k_B T$	Boltzmann temperature
m	mass of a DPD particle
n	number density
r_c	cut-off radius
w	weighting function
\mathbf{e}	unit vector
\mathbf{r}	position vector
\mathbf{v}	velocity vector
\mathbf{F}	force vector
\mathbf{S}	stress tensor

Subscripts

C	denotes <i>Conservative</i> force term
D	denotes <i>Dissipative</i> force term
R	denotes <i>Random</i> force term
e	<i>external</i>

Greek letters

γ	coefficient reflecting the strength of dissipative/drag force
σ	coefficient reflecting the strength of random force
μ	dynamic viscosity
ρ	mass density
η	viscosity
κ	isothermal compressibility
α	time-scale radio
τ	relaxation time scale
τ_I	inertia time scale

Mathematical operators

$\langle \cdot \rangle$	the average operation
$[R^2 w_D]_R$	$\int d\mathbf{R} R^2 w_D(R)$

Abbreviations and Acronyms

BDS	Brownian Dynamics Simulation
BEM	Boundary Element Method
DPD	Dissipative Particle Dynamics
FDM	Finite Difference Method
FEM	Finite Element Method
FVM	Finite Volume Method
LBM	Lattice Boltzmann Method
LGA	Lattice-Gas Automata
MC	Monte Carlo
MD	Molecular Dynamics
NS	Navier-Stokes
PDEs	Partial Differential Equations
PDF	Probability Density Function
RBFs	Radial Basis Functions
RDF	Radial Distribution Function
SD	Stokesian Dynamics
SDPD	Smoothed Dissipative Particle Dynamics
SETD	Stochastic Exponential Time Differencing
SPH	Smooth-particle Hydrodynamics
TCAF	Transverse-current Auto-correlation Function

Chapter 1

Introduction

1 Overview

Fluids exist around us and we can see many different types of fluid flows. Most of fluid flow problems cannot be simulated in an analytic/exact manner, and one should rely on numerical methods to obtain their approximate solutions. The numerical methods can be classified into three groups corresponding to the following three groups of length scales: macroscale (continuum media, length scale bigger than 10^{-4}m), mesoscale (length scale ranging from 10^{-7}m to 10^{-4}m) and microscale/nanoscale (length scale ranging from 10^{-8}m to 10^{-6}m for microscale and from 10^{-9}m to 10^{-7}m for nanoscale) [Liu and Liu (2016)].

1.1 Macroscale

The behaviour of a fluid system on macroscale can be mathematically described by the Navier-Stokes equations which is a well-known model in partial differential equations (PDEs). Various numerical methods have been developed to solve the PDEs. Their common features are (i) to reduce the infinite degrees of freedom of a continuous system to a finite set; and (ii) to convert the PDEs into sets of algebraic equations, from which a computer solution to the Navier-Stokes

equation can be obtained.

Based on the criterion of discretisation, numerical methods can be divided into two groups: Mesh/grid-based methods and meshless methods.

- **Mesh/grid-based methods**: Typical mesh/grid-based methods include the finite difference methods (FDMs), finite element methods (FEMs), finite volume methods (FVMs), boundary element methods (BEMs) and spectral methods.

- **FDM** is considered to be the simplest and oldest method for solving differential equations. The original FDM (in one dimension of space) was originated probably in 1768 [Alik Ismail-Zadeh (2010), Blazek (2015)], the time of Leibniz and Euler, and was extended to two-dimensional space by C. Runge in 1908 [Alik Ismail-Zadeh (2010)]. The principle of FDMs is to approximate the derivatives in differential equations by linear combinations of function values at grid points. Over time, FDMs have been developed to deal with complex problems of science and technology (e.g., Özişik et al. (2017), Guo et al. (2018), Jamelot et al. (2019), Gu et al. (2019), Wang et al. (2020a), Wang et al. (2020c), Brachet and Croisille (2021), Lindeberg et al. (2021), Gregor et al. (2021)). Although high-order finite difference schemes can achieve high resolution and reasonable accuracy on coarse grids, one is also interested in a reasonable increase of grid points and computational cost, especially for models relative to three dimensions or non-linear. Nevertheless, FDMs are less flexible to adapt to awkward geometries because they use regular elements (e.g., cubes, squares, . . .). Moreover, they are prone to numerical instability, most notably the models involving singularities such as turbulence.

- **FEM** was first found in the 1940s with the publications of Hrennikoff

(1941) and Courant (1943). At first, it was originated for solving problems in solid mechanics. Then it has been expanded to areas of computational physics and engineering including CFD. As time goes on, the FEM has been developed rapidly with strong developments came from Argyris and Kelsey (1960), Argyris and Scharpf (1969), Argyris and Scharpf (1969), Zienkiewicz and Taylor (2000a), Zienkiewicz and Taylor (2000b), Zienkiewicz and Taylor (2000c), Zienkiewicz et al. (2013), Zienkiewicz et al. (2014).

In contrast to approximate differentials in FDMs, the FEM is based on the weak form of differential equations, i.e. it investigates the integral of differential equations. The basic principle of the FEM is to divide the global domain into individual small patches, called finite elements, and then locally approximate the weak form of differential equations within the boundary of each patch; the global solution is finally obtained by stitching the individual solutions on these patches back together. The meanings of subdividing the global region are to (i) accurately represent complex geometry, (ii) include dissimilar properties, (iii) easily represent the total solution, and (iv) capture local effects. The advantages featured of FEMs are flexible to adapt to arbitrarily shaped regions, to utilise structured or unstructured meshes, and deal with a large class of differential equations. Consequently, it is widely applicable in solving differential equations [e.g., Reddy and Gartling (2010), Zienkiewicz et al. (2013), Zienkiewicz et al. (2014), Rao (2018), Gibson et al. (2019), Lu et al. (2020), Schröder and de Matos Pimenta (2020), Mulligan et al. (2020)].

- **Spectral methods** have been utilized since the late 1960s and early 1970s [Deville et al. (2002)], and proposed for applications in practi-

cal flow simulations due to their high order of accuracy [Gottlieb and Orszag (1977), Canuto et al. (1988), Deville et al. (2002), Ma et al. (2021)]. These methods are global, because the value of a derivative at a given point in space depends not only on the solution at neighbouring points, but also on the solution from the entire domain. Their basic concept is to expand the flow solution as coefficients for ansatz/trial functions, take the exact derivative of these functions, and then truncate to a finite set of ansatz functions/coefficients. The coefficients corresponding to ansatz functions are considered as a spectrum of the solution. Although spectral methods usually have a very high order of accuracy on ground of their global nature, they are geometrically less flexible and more complicated than other methods. In addition, the spectral representation of the solution containing non-smooth gradients (e.g. problems relative to shocks or discontinuities) is tough. Spectral methods are therefore adapted and efficient for the problems in simple geometries.

- **BEM** emerged in the late 1970s [Cheng and Cheng (2005)]. The first conference on BEM at Southampton University in 1978 marked the birth of BEM [Brebbia (2017)]. It is estimated as a robust technique with outstanding features versus FEM such as (i) dimensionality reduction making coding easier, (ii) dealing with moving boundaries in the elegant way with better accuracy, and (iii) taking account of infinite domains without the need of artificial boundaries. BEM has been successfully undertaking since 1978 and reached a real state of maturity until now with resolving large structural problems oriented towards industrial applications [Brebbia et al. (1984), Brebbia and Wrobel (1992), Brebbia and Katsikadelis (2006), Brebbia et al. (2007),

Kirkup (2007), Brebbia and Skerget (2008), Brebbia (2010), Brebbia and Popov (2011), Brebbia and Poljak (2012), Telles (2012), Gwinner and Stephan (2018), Beer et al. (2020)].

- **FVM** was first known in the 1970s with works of Rizzi (1976) and Jameson and Caughey (1977). It is especially proposed for the differential equations arising from physical conservation laws and principally used in CFD. The basic concept of the FVM is to subdivide the whole domain into smaller and simpler mesh elements called control volumes, then integrate these volume elements. Based on the divergence theorem, these volume integrals are converted to surface integrals, and they are investigated as fluxes at the surfaces of each control volume. A notable point in FVMs is local conservation because the flux from a given volume element to its neighbour is identical. Similar to FEMs, the FVM is also flexible to adapt to arbitrary geometries and use structured or unstructured meshes. Because of its attractive properties, the FVM is also widely applicable [e.g., LeVeque (2002), Petrova (2012), Vázquez-Cendón (2015), Kempe and Hantsch (2017), Liu et al. (2019), Terekhov and Vassilevski (2019), Kitamura (2020)].

Although these methods have been widely employed to model engineering problems in complex geometries, they require extensive meshing and complexity in discretization and programming.

- ***Meshless methods***: Meshless methods belong to the class of techniques for dealing with boundary/initial value partial differential equations where discretization is principally based on nodes or particles. The meshless method was marked by the emergence of Smooth-particle Hydrodynamics (SPH) in 1977. There are several meshless methods such as kernel meth-

ods, moving least square method, Petrov-Galerkin, Radial Basis Functions (RBFs), Smooth-particle Hydrodynamics (SPH). The methods featured in this class are Radial Basis Functions (RBFs), Smooth-particle Hydrodynamics (SPH). The meshless method is considered a particularly attractive method by virtue of no numerical integration, no domain or surface discretization, and ease in programming.

However, it is the fact that the macroscopic methods could not model the statics and dynamics of the fluid system at length and time scales, where the effect of Brownian motions takes place, and thus do not have the ability to capture the microstructure of the complex fluids.

1.2 Microscale/Nanoscale

The behaviour of a fluid system on these length scales can be mathematically described by Newton's equations of motion in classical theory. Two groups of methods developed for solving such systems are Monte Carlo (MC) and Molecular Dynamics (MD).

- **MC method** was modified by Metropolis et al. (1953) to simulate the interaction of individual molecules. MC method utilises a certain stochastic law to track microscopic states, and thus it is inapplicable to dynamic systems dependent on time, only applicable to thermodynamic equilibrium phenomena [Satoh (2010)]. As time passes, however, the MC method has been developed to apply to science and engineering [Binder et al. (1995), Mordechai (2011), Seco and Verhaegen (2013), Mazhdakov et al. (2018), Morin (2019), Bidokhti (2019), Barbu and Zhu (2020), Sowers et al. (2020)].
- **MD method** was first originated in the late 1950s to study the interactions of hard spheres with the publications of Alder and Wainwright (1957) and

Alder and Wainwright (1959). Rahman (1964) marked a major advance of MD method by utilising a realistic potential in simulating molecular dynamics in liquid argon. The first application of MD method to simulate a realistic system, liquid water, was publicised by Stillinger and Rahman (1974). And the first protein simulations were done by McCammon et al. (1977). In contrast to MC methods, the movement of particles in MD simulations is tracked by Newton’s equations of motion, therefore it is suitable for both thermodynamic equilibrium and nonequilibrium phenomena. Although MD has evolved and expanded to be broadly applicable to physical chemistry, biology, geology, condensed matter physics and materials science, it requires an extremely large number of particles to obtain collective behaviour [Hernández (2008), Luckhurst and Veracini (2012), Wang (2012), Ciccotti et al. (2014), Ganesan et al. (2017), Vakhrushev (2018), Venable et al. (2019), Bedrov et al. (2019), Kamberaj (2020), Habasaki (2020), Deganutti et al. (2020), Galvin et al. (2021), Huang et al. (2021), Separdar et al. (2021), Kabedev et al. (2021)].

However, when investigating the fluid system at the mesoscopic and macroscopic length scales, their computational costs increase considerably since a huge number of time steps are required.

1.3 Mesoscale

There have been several numerical methods developed for simulation of mesoscopic problems. They include the Dissipative Particle Dynamics (DPD) [e.g. Hoogerbrugge and Koelman (1992), Koelman and Hoogerbrugge (1993), Español (1995), Español and Warren (1995)], smoothed Dissipative Particle Dynamics (SDPD) [e.g. Español and Revenga (2003)] and Lattice Boltzmann method (LBM) [e.g. McNamara and Zanetti (1988), Higuera and Jiménez (1989), Ladd

(1994)].

In LBM, the governing equations are derived from the Boltzmann kinetic equations. The method was originated to solve complex fluid systems, where several difficulties of macroscopic approaches are overcome. LBM has been applied successfully to many important applications such as the flow through porous media [e.g. Spaid and Phelan (1997), Yamamoto and Takada (2006), Doormaal and Pharoah (2009), Rong et al. (2011)], boiling dynamics [e.g. Yang et al. (2000)], dendrite formation [e.g. Ludwig et al. (2014), Sun et al. (2016)], suspensions [Sivadasan et al. (2019)], etc.

In DPD, one only needs to solve Newton's equations of motion, which is in contrast to continuum methods, where a set of PDEs are considered and to LBM, where the kinetic equations are considered. It is shown that DPD conserves mass and momentum. The method satisfies the Navier-Stokes equation in the mean and can thus be considered as a particle-based simulation scheme for macroscale fluid problems. An attractive feature of DPD is that the method can be extended to simulate complex-structure fluids in a straightforward way by constraining subsets of DPD particles in the system. The Newtonian fluid is made "complex" (i.e. non-Newtonian) by simply adding extra interactions between the DPD particles. By modifying the conservative interactions between the DPD particles, one can easily construct polymers, colloids, amphiphiles, mixtures, etc. For example, polymer chains are represented by connecting some fluid particles by some connector force laws (e.g. the FENE (Finitely Extendable Non-linear Elastic) dumbbell and the worm-like chain) [Fan et al. (2006)]. This will allow one to model any particular form of the suspension. There have been many successful applications of DPD, in monodispersed Newtonian suspensions [Boek et al. (1997), Pan et al. (2010b)], in polymer solutions [Fan et al. (2006)], in immiscible binary liquid mixtures [Novik and Coveney (1997)]; this list is not meant to be

exhaustive.

In SDPD, the formulation is derived from the Navier-Stokes equation (continuum mechanics equation) with the inclusion of thermal fluctuations. It is shown that SDPD has a consistent scaling of thermal fluctuations. When applied to macro fluid systems, like traditional methods, it possesses the property of mesh convergence. It can be seen that an SDPD solution to a mesoscopic problem is thus constructed from the top-down approach. On the other hand, DPD is a bottom-up approach, where the formulation is derived from Molecular Dynamics (MD). DPD is the only technique that does not require a-priori constitutive knowledge of the fluid, The constitutive framework is fully specified in the microstructure that goes into the description of the DPD model (the relevant constitutive law will result from the fluid description). This opens a new way to build up constitutive equations relating stress to rate of strain for complex suspensions, complementing traditional approaches of theories and experiments. DPD is the technique adopted in this study.

2 Research gap and motivation

An attractive feature of DPD over other mesoscopic simulation methods lies in its algorithmic simplicity. However, the original DPD suffers some drawbacks related to (i) equation of state, (ii) no formal way of deriving DPD from an atomistic system for simple fluids (unbonded atoms), (iii) energy equation, (iv) issues of thermal fluctuation scaling, and (v) specification of physical properties of fluids.

While there are many computational fluid dynamics schemes, there are problems for which existing methods are inadequate. In particular, these include the problems presented by suspensions of rigid particles in a fluid medium.

The main purposes of this research project we are aiming for are (i) to develop

a physical version of DPD to address issues of thermal fluctuation scaling and specification of physical properties of a model fluid, (ii) to extend DPD to its generalised hydrodynamics, and (iii) to produce improved results in analysis of complex fluids at the mesoscale.

3 Objectives of the thesis

The main objectives of the research are

- to express the original DPD input parameters as functions of the macroscopic properties of a model fluid,
- to examine the effect of the coarse-graining level on the behaviour of the single-phase and multi-phase systems,
- to examine the scaling of thermal fluctuations,
- to propose a new mechanism of promoting incompressibility,
- to express the transport coefficients as functions of the wavelengths and frequencies of thermal fluctuations (generalised hydrodynamics),
- to build up a mesoscopic computational model for multiphase fluids, where the suspending fluid phase and suspended solids are all represented by means of particles with appropriate interactions,
- to explore the possibility of using a single set of DPD particles to model a linear viscoelastic fluid,
- to study particulate suspensions in the generalised hydrodynamic regime, and the effect of the suspended object's size and the repulsion force's strength on the suspension viscosity.

4 Outline of the thesis

The thesis is made up of six chapters.

In Chapter 2, a review of the modelling of complex-structure materials such as particulate suspensions, and a review of the standard DPD formulation and its applications to complex fluids are given.

In Chapter 3, a physical version of DPD is presented. In this version, the input parameters are directly determined from the (physical) fluid properties such as mass density, compressibility and viscosity. It is shown that the method can achieve a consistent scaling of thermal fluctuations and produce similar flow behaviours at different coarse-graining levels.

In Chapter 4, DPD is developed to work on its generalised hydrodynamics. The transport properties are considered as functions of length and time scales. It is shown that a single set of DPD particles can be used to model a linear viscoelastic fluid. The effect of the length scale is studied by employing transverse current auto-correlation functions (TCAF) and the effect of the time scale is studied by using analytic expressions of the shear stress in a simple small amplitude oscillatory shear flow.

In Chapter 5, the proposed method is applied to simulate particulate suspensions. The spring model is utilised to model suspended spheres in 3D and cylinders in 2D. The viscosity estimation of the suspending/solvent phase is conducted taking into account size effects due to the presence of suspended objects. The effect of repulsive forces on the suspension viscosity is also studied.

In Chapter 6, conclusion remarks and future work are given.

Chapter 2

DPD for Particulate Suspensions

1 Particulate suspensions

1.1 Introduction

Suspensions, which are formed by rigid particles, droplets or gaseous bubbles suspended in a liquid, occur widely in nature and man-made products [Metzner (1985), Mewis and Wagner (2012), Phan-Thien and Mai-Duy (2017), Tanner (2000)]. Typical examples include foodstuffs, paints, blood, fluidised beds and bubble columns. The size of the suspended particles is an important consideration; when the particles are sufficiently small (typically $\lesssim 10\mu m$), they will undergo their Brownian motions, and one speaks of a colloidal suspension - otherwise, one has a non-colloidal suspension. In modelling suspensions, one usually starts with a Newtonian suspension of uniformly-sized suspended particles – a monodispersed Newtonian suspension; otherwise, one has a polydispersed suspension. In this project, by suspension, we restrict our focus to a suspension of rigid particles. Droplet and bubble suspensions will not be considered. The suspending liquid is Newtonian; the suspended particles are of spherical shape in 3 dimensions and of cylindrical shape in 2 dimensions. In flows, suspensions

behave in a non-Newtonian manner by virtue of their evolving microstructure (spatial arrangement of rigid particles, which is flow dependent). Typically, suspensions are characterised by the following properties [Phan-Thien and Mai-Duy (2017), Tanner (2000)]:

- a shear-rate dependent and highly concentration-dependent viscosity;
- non-zero normal stress differences - Investigations suggest that while the second normal stress difference, N_2 , is negative at all shear rates, the first normal stress difference, N_1 , is positive at low shear rates and high concentrations, and negative at high shear rates [Foss and Brady (2000)], and they are highly dependent on the nature of the solvent [Mall-Gleissle et al. (2002)];
- migration of particles from high to low shear region in an inhomogeneous shear flow.

The understanding of these issues is vital in the design and control of industrial particulate-flow processes. They have been extensively investigated theoretically, experimentally and numerically.

1.2 Numerical modelling of particulate suspensions

Computer simulations have emerged as a powerful tool to provide insight into the dynamics of suspensions, which complement experiments and analytical theories. Numerical techniques used can be classified into two groups. In the first group, hydrodynamic interactions are governed by the linearised Navier-Stokes equations in the limit of zero particles inertia. Analytic solutions of the Stokes flow around one and two interacting spheres are available; one can construct a grand resistance matrix, which relates the force/torque exerted by the fluid on the particles to the particle velocities. The simulation methods are known as

Stokesian Dynamics (SD) [Bossis and Brady (1984)]. An accelerated version of SD required only $O(N \log N)$ operations, where N is the number of spheres. On the other hand, SD methods encounter difficulties to model particles of arbitrary shape, non-zero particle Reynolds number, non-Newtonian suspending liquid, non-periodic boundary conditions, etc. In the second group, the suspending liquid is modelled explicitly. Hydrodynamic interactions are taken into account by solving the full set of hydrodynamic equations, and thus some of the difficulties associated with SD are eliminated. This group includes grid/mesh-based methods: the boundary-fitted mesh methods [Hu (1996)], fictitious domain methods [Glowinski et al. (2001)], etc., and particle-based methods: the smoothed particle hydrodynamics (SPH) [Ellero and Tanner (2005)], lattice Boltzmann methods [Ladd (1994)], dissipative particles dynamics (DPD) [Hoogerbrugge and Koelman (1992), Marsh (1998)], smooth dissipative particles dynamics (SDPD) [Español and Revenga (2003)], etc. For the former, there are grids/meshes involved and the resultant algebraic equations need be solved simultaneously. For the latter, the positions and velocities of the particles can be advanced individually, which facilitates large-scale simulations. DPD is the only technique that does not require a-priori constitutive knowledge of the fluid, and there have been many successful applications of DPD, in monodispersed Newtonian suspensions [Boek et al. (1997), Pan et al. (2010b)], in polymer solutions [Fan et al. (2006)], in immiscible binary liquid mixtures [Novik and Coveney (1997)]; this list is not meant to be exhaustive. DPD is the technique adopted in this study.

2 Review of DPD

2.1 Brief introduction

Dissipative Particle Dynamics (DPD), originally proposed by Hoogerbrugge and Koelman (1992) as a mesoscopic simulation technique for complex fluid systems, has received considerable attention in the last two decades. It is considered as an improvement over conventional Molecular Dynamics (MD) [Allen and Tildesley (1987), Rapaport (2004), Satoh (2010)] and Lattice-Gas Automata (LGA) [Frisch et al. (1986)]. Although MD method can be utilised to simulate some interesting physical phenomena [Dzwiniel et al. (1995), Herrmann (1999)], it requires an extremely large number of particles to obtain collective behaviour. Another popular particle-based method is Brownian Dynamics Simulation (BDS) (e.g., Fan et al. (1999)). However, BDS conserves particles (mass), but not momentum. In DPD, each particle represents a group of fluid molecules. DPD particles interact through a soft potential and thus the simulation can be carried out on length and time scales far beyond those of Molecular Dynamics. Hydrodynamic interactions are accounted for by employing velocity-dependent dissipative forces. DPD particles are not supposed to represent faithfully the original fluid volume; rather, they are a model of the fluid behaviour (viscous, or otherwise dictated by the specification of the microstructure connectivity).

It should be pointed out that ensemble-average quantities formed from the DPD particle configurations and velocities satisfy the conservation of mass and momentum [Español and Warren (1995), Phan-Thien and Mai-Duy (2017)], and thus the method is qualified as a particle-based method for solving continuum problems. Objects suspended in the fluid can also be represented by DPD particles with appropriate forms of interactions. These features make the DPD method (and its variants) very attractive in the modelling of complex fluid systems. On the

other hand, a DPD fluid is compressible in nature and has a slow dynamic response. The employment of small masses of particles was proposed to achieve low Reynolds numbers, higher sonic speeds (more incompressible) and higher Schmidt numbers (faster response) [Mai-Duy et al. (2013)]. This comes at the expense of solving stiff stochastic differential equations. DPD and its variants have been utilised successfully in the simulation of various classes of complex fluids, for examples, fluid mixtures [Novik and Coveney (1997), Laradji and Hore (2004), Liu et al. (2007)], flexible filament in biology [Anand et al. (2017)], polymer [Kong et al. (1997), Jiang et al. (2007), Nikunen et al. (2007), Litvinov et al. (2008), Zhou et al. (2017), Kobayashi and Arai (2018), Minkara et al. (2019), Zhang et al. (2020), Sengupta and Lyulin (2020)], red blood cell modelling [Pan et al. (2010a), Ye et al. (2013)], colloidal suspensions [Koelman and Hoogerbrugge (1993), Boek et al. (1997), Chen et al. (2006), Pan et al. (2010b), Bian et al. (2012), Phan-Thien et al. (2014a), Jamali et al. (2015), Wang et al. (2020b)], electric field [Deng et al. (2016), Gavrilov et al. (2016), Tran et al. (2019), Vaiwala et al. (2019), Waheed et al. (2020), Gavrilov (2020)], RDX decomposition [Lísal et al. (2019)], drug delivery applications [Yu et al. (2018), Catala (2019), Feng et al. (2020)], colloidal gels [Jamali et al. (2017), Boromand et al. (2017), Chen and Yong (2018), Song et al. (2018), Jamali et al. (2019), Palkar et al. (2020), Wang et al. (2020d), Lenzi et al. (2020)], surfactant systems [Panoukidou et al. (2019), Lavagnini et al. (2020)], etc.

2.2 Formulation

2.2.1 DPD equation

In the dissipative particle dynamics (DPD) [Marsh (1998)], the fluid is modelled by a system of particles undergoing their Newton 2nd law motions

$$m_i \ddot{\mathbf{r}}_i = m_i \dot{\mathbf{v}}_i = \sum_{j=1, j \neq i}^N (\mathbf{F}_{ij,C} + \mathbf{F}_{ij,D} + \mathbf{F}_{ij,R}) + \mathbf{F}_{i,e}, \quad (2.1)$$

where m_i , \mathbf{r}_i and \mathbf{v}_i represent respectively the mass, position and velocity vectors of a particle i , $i = \overline{1, N}$; N is the total number of particles, the superposed dot denotes a time derivative, and $\mathbf{F}_{i,e}$ is an external force on particle i . An example of the external force is gravity (body force), which is used to simulate the effect of a pressure gradient. The first three forces on the right side represent the conservative (subscript C), the dissipative (subscript D) and the random (subscript R) forces

$$\mathbf{F}_{ij,C} = a_{ij} w_C \mathbf{e}_{ij}, \quad (2.2)$$

$$\mathbf{F}_{ij,D} = -\gamma w_D (\mathbf{e}_{ij} \cdot \mathbf{v}_{ij}) \mathbf{e}_{ij}, \quad (2.3)$$

$$\mathbf{F}_{ij,R} = \sigma w_R \theta_{ij} \mathbf{e}_{ij}, \quad (2.4)$$

in which a_{ij} , γ and σ are the amplitudes; w_C , w_D and w_R the weighting functions, with $\mathbf{e}_{ij} = \mathbf{r}_{ij}/r_{ij}$ the unit vector from particle j to particle i ($\mathbf{r}_{ij} = \mathbf{r}_i - \mathbf{r}_j$, $r_{ij} = |\mathbf{r}_{ij}|$), $\mathbf{v}_{ij} = \mathbf{v}_i - \mathbf{v}_j$ the relative velocity vector and a Gaussian white noise $\theta_{ij}(t) = \theta_{ji}(t)$ with stochastic properties as follows

$$\langle \theta_{ij}(t) \rangle = 0, \quad \langle \theta_{ik}(t) \theta_{jl}(t') \rangle = (\delta_{ij} \delta_{kl} + \delta_{il} \delta_{jk}) \delta(t - t'), \quad i \neq k, \quad j \neq l.$$

The three interaction forces are pairwise, center-to-center, and zero outside a cut-off radius. The conservative force derived from a soft potential is used to model

local thermodynamics (i.e., equation of state). The dissipative/drag/friction force depending on the velocity difference between particles depicts the viscous resistance in the real fluids. The random/stochastic force describes the Brownian-like, fluctuating character of molecules, helps to maintain the temperature of the system and implements a viscous effect. Besides, the combination of dissipative and random forces assumes two main tasks: (1) to create a DPD thermostat in order for the system to reach a certain equilibrium, (2) to enable transport properties (e.g., velocity) to be adjusted without changing the equilibrium thermodynamics. The random force cannot be chosen independently to the dissipative force if the specified energy of the system (Boltzmann temperature $k_B T$) is to be maintained, which is the essence of the fluctuation-dissipation theorem. According to the fluctuation-dissipation theorem for the method [Español and Warren (1995)], the detailed balance constraint is as follows

$$w_R = \sqrt{w_D}, \quad \sigma = \sqrt{2\gamma k_B T}. \quad (2.5)$$

In the usual way [Groot and Warren (1997), Fan et al. (2006), Phan-Thien and Mai-Duy (2017)], the weighting functions are of the form

$$w_C(r_{ij}) = 1 - \frac{r_{ij}}{r_c}, \quad (2.6)$$

$$w_D(r_{ij}) = \left(1 - \frac{r_{ij}}{r_c}\right)^s, \quad (2.7)$$

where s is a positive value ($s = 2$ for standard value and $s = 1/2$ for modified value) and r_c the force cut-off radius beyond which the weighting function vanishes.

In general, any modification of the input DPD parameters can result in a change in the physical properties (e.g. viscosity) of the model fluid. In particular, by changing n while keeping all the other variables unchanged, the resultant DPD

systems represent different fluids, which makes the characteristic study of DPD (*e.g.* the scaling of the thermal fluctuations) difficult.

It is noted that for a particle, apart from the velocities, its diffusivity and its exclusion zone are also important properties. Below are formulas that can be used to measure the size and average travel distance of a DPD particle.

The effective size of the solvent particles (and also for the suspended particles) can be estimated using the radial distribution function (RDF) defined as Reichl (2016),

$$g(r) = \frac{1}{N/A} \frac{s}{2\pi r \Delta r} \quad (\text{for 2D}), \quad (2.8)$$

$$g(r) = \frac{1}{N/V} \frac{s}{4\pi r^2 \Delta r} \quad (\text{for 3D}), \quad (2.9)$$

where A/V is the area/volume of the domain containing N particles, s is the number of particles in a circular/spherical shell of width $(r - \Delta r) \rightarrow r$ at a distance r from the centre of the particle. The function states that there is no neighbouring particle at the distance r if $g(r) = 0$ and vice-versa. It is expected that (i) function $g(r)$ approaches zero as the distance q is reduced, and (ii) the value of r , where $g(r)$ approaches zero, for the colloidal particle is larger than that for the solvent particle. The RDF has a direct physical interpretation for spherical particles only.

Remarks: (i) cut-off radius of conservative force and dissipative force can be different; (ii) weighting function of conservative and dissipative forces also can be different.

2.2.2 Conservative properties

Based on the system state (positions and velocities of DPD particles), one can define the local fluid density as follows

$$\rho(\mathbf{r}, t) = \left\langle \sum_i m \delta(\mathbf{r} - \mathbf{r}_i) \right\rangle = mn(\mathbf{r}, t),$$

where $n(\mathbf{r}, t)$ is the number density, $\langle \dots \rangle$ is an ensemble average.

The local linear momentum are calculated by

$$\rho(\mathbf{r}, t)\mathbf{u}(\mathbf{r}, t) = \left\langle \sum_j m\mathbf{v}_j \delta(\mathbf{r} - \mathbf{r}_j) \right\rangle.$$

These quantities have been shown to satisfy conservation laws (Español (1995), Marsh et al. (1997), Phan-Thien and Mai-Duy (2017))

$$\frac{\partial}{\partial t} \rho(\mathbf{r}, t) + \nabla \cdot (\rho(\mathbf{r}, t)\mathbf{u}(\mathbf{r}, t)) = 0, \quad \nabla = \frac{\partial}{\partial \mathbf{r}}, \quad (2.10)$$

and

$$\frac{\partial}{\partial t} (\rho\mathbf{u}) + \nabla \cdot (\rho\mathbf{u}\mathbf{u}) = \nabla \cdot \mathbf{S}. \quad (2.11)$$

Hence, DPD can be considered as a particle-based method for solving continuum flow problems (2.10)-(2.11), a bottom up approach to solve Navier-Stokes equations..

2.2.3 Calculation of stress tensor

The flow domain is divided into grids and local data are collected in each bin. The flow properties (*e.g.* number density, fluid density and linear momentum) are calculated by averaging over all sampled data in each bin. The stress tensor is calculated according to the expression of Irving and Kirkwood (1950) [Phan-

Thien and Mai-Duy (2017)]

$$\mathbf{S} = -\frac{1}{V} \left[\sum_i m \mathbf{V}_i \mathbf{V}_i + \frac{1}{2} \sum_i \sum_{j \neq i} \mathbf{r}_{ij} \mathbf{F}_{ij} \right] = -n \left(\langle m \mathbf{V} \mathbf{V} \rangle + \frac{1}{2} \langle \mathbf{r} \mathbf{F} \rangle \right), \quad (2.12)$$

where $\mathbf{V}_i = \mathbf{v}_i - \mathbf{u}(\mathbf{r})$ is the peculiar velocity of particle i (i.e. the fluctuation velocity of particle i with respect to the mean field velocity), V is the volume of bin. The first term on the right side of (2.12) denotes the contribution to the stress from the momentum (kinetic) transfer of DPD particles and the second term from the interparticle forces.

The constitutive pressure is determined from the trace of the stress tensor

$$p = -\frac{1}{3} \text{tr} \mathbf{S}. \quad (2.13)$$

2.2.4 Time scales

There are three time scales in the stochastic differential equation (2.1) [Phan-Thien and Mai-Duy (2017)]:

- a fluctuation time scale τ_R of the random force, which is arbitrarily small,
- an inertia time scale $\tau_I = O(m\gamma^{-1})$,
- and a relaxation time scale $\tau = O(\gamma H^{-1})$, where H is the stiffness of the system, $H = O(|\partial_r F_C|) = O(a_{ij} r_c^{-1})$.

2.2.5 Input parameters for the original DPD

According to the virial theorem [Irving and Kirkwood (1950)], the pressure is computed as

$$p = \frac{\rho}{m} k_B T + \frac{1}{2d} \left(\frac{\rho}{m} \right)^2 \int r F_{ij}^C(r) g(r) dr = n k_B T + \frac{n^2}{2d} \int r F_{ij}^C(r) g(r) dr, \quad (2.14)$$

where $g(r)$ is RDF, $\rho = mn$ mass density, m mass of a DPD particle, n number density, d the flow dimensionality. For simplicity, we take $g(r) = 1$ corresponding to an infinite number of DPD particles.

For case of 2D,

$$p = nk_B T + \frac{\pi}{2} a_{ij} n^2 \int r^2 w^C(r) dr . \quad (2.15)$$

For case of 3D,

$$p = nk_B T + \frac{2\pi}{3} a_{ij} n^2 \int r^3 w^C(r) dr . \quad (2.16)$$

Based on the Weeks-Chandler-Anderson perturbation theory of liquids, the isothermal compressibility can be represented through the dimensionless parameter as follows

$$\kappa^{-1} = \frac{1}{nk_B T \kappa_T} = \frac{1}{k_B T} \left(\frac{\partial p}{\partial n} \right)_T , \quad (2.17)$$

where κ_T is the usual isothermal compressibility.

For water at room temperature (300K), the value of the dimensionless compressibility is $\kappa^{-1} \approx 15.9835$. With w_C is given as (2.6), from (2.15) and (2.17) yields

$$a_{ij} \approx \frac{57.23 k_B T}{n r_c^3} \quad \text{for 2D} , \quad (2.18)$$

and

$$a_{ij} \approx \frac{72 k_B T}{n r_c^4} \quad \text{for 3D} . \quad (2.19)$$

For 3D, Groot and Warren (1997) recommended

$$a_{ij} \approx \frac{75 k_B T}{n r_c^4} . \quad (2.20)$$

In simulation, the DPD input parameters include s , a_{ij} , σ , $k_B T$, m , r_c and the particle density n . A standard choice for σ is 3, i.e. $\gamma = 4.5$.

In practice, equations of motion (2.1) are solved with their quantities in reduced units; one can take, for example, $m = 1$, $r_c = 1$ and $k_B T = 1$. In this way,

equations of motion (2.1) are dimensionless.

2.2.6 Block diagram for the DPD simulation

Procedure of a standard DPD simulation is detailed in Fig.2.1, where "Thermodynamic equilibrium" is process for the system to reach equilibrium before collecting data, and "Flow simulation" is period of collecting data.

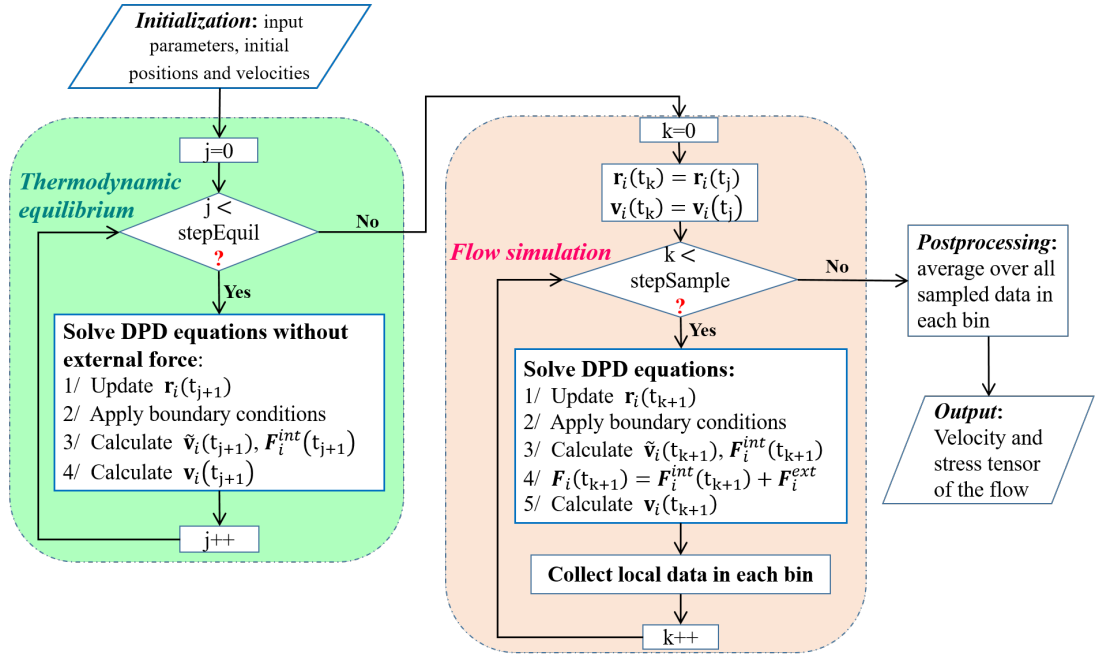


Figure 2.1: Computational processing of a DPD simulation.

2.3 Numerical modelling of particulate suspensions

In the context of DPD, a suspended particle can be modeled in three ways: frozen DPD particles[Koelman and Hoogerbrugge (1993), Boek et al. (1997), Martys (2005), Chen et al. (2006)], single DPD particle [Dzwiniel and Yuen (2000), Pryamitsyn and Ganesan (2005), Pan et al. (2008), Pan et al. (2010b), Whittle and Travis (2010), Groot (2012), Mai-Duy et al. (2013)], or spring model [Phan-Thien et al. (2014a)]. Each scheme has particular disadvantages and advantages.

2.3.1 Frozen DPD particles based model

The concept of the frozen-particle model is to represent a suspended particle by a subset of the same DPD particles, but they remain at a fixed relative position and interact with other particles. The velocity and position of a suspended particle is derived from the sums of forces and torques acting on it. The featured strength of this model resides in the capacity to model an arbitrary shape and size suspended particle. Nevertheless, due to the frozen characteristic of the constituent particles, the dissipative forces between themselves vanish, and it is tough to sustain a specified constant temperature (specific kinetic energy) throughout the simulation domain. In addition, it requires a significant number (a few hundreds) of basic DPD particles to model a spherical particle [Martys (2005), Chen et al. (2006)], and thus the computational effort increases considerably and the difference in mass density between solvent and suspended phases is too large.

2.3.2 Single-particle based model

The single-particle model is more simple than the frozen-particle because it uses a single DPD particle to represent a suspended particle, and thus updating velocity and position is based on its DPD equations and the computational expense do not increase considerably. However, the model has drawbacks such as (i) the interaction between particles is classified into three types: solvent-solvent (S-S), solvent-colloidal (S-C), and colloidal-colloidal (C-C); (ii) it requires more effort in adjusting parameters between the forms of interactions; (iii) the model is restricted to spherical (3D) and circular (2D) suspended particles; and (iv) it is tough to model the mass density of suspended phase in physics.

2.3.3 Spring model for suspended particles in DPD

For the spring model, only a few basic DPD particles are utilised to construct a suspended particle. It is proposed to relict the shortcomings of the frozen particle models (e.g. large systems, tough in maintaining the temperature of system), and the single particle models (e.g. complex interactions, spherical/circular shape limitations). Moreover, it has the ability to address issues related to number density and volume fraction.

Consider the k^{th} suspended particle represented by a few basic DPD particles, associated with the reference sites (on that colloidal particle) by linear springs of very large stiffness (e.g., Fig. 2.2). The suspended particles move as a rigid body

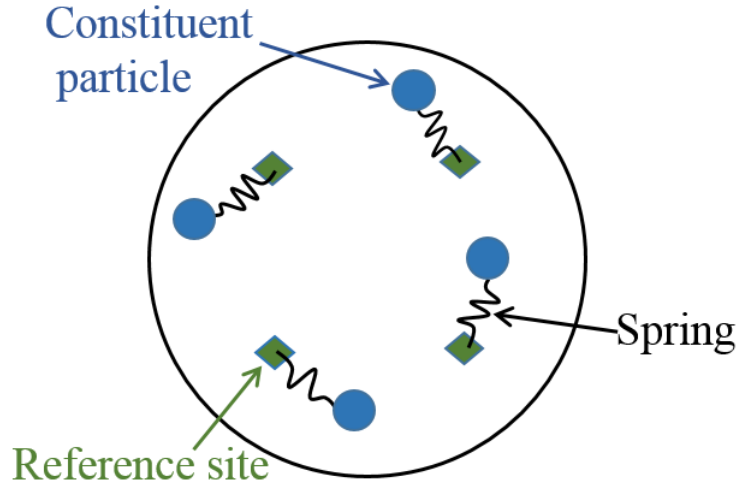


Figure 2.2: A solid particle can be modeled by four constituent particles which are basic DPD particles. The reference sites are supposed to move as a solid body.

motion according to their Newton-Euler equations, using data from the previous time step,

$$M_c^k \frac{d\mathbf{V}_c^k}{dt} = \mathbf{F}^k(t), \quad (2.21)$$

$$\mathbf{I}^k \frac{d\boldsymbol{\omega}^k}{dt} = \mathbf{T}^k(t) + \boldsymbol{\omega}^k \times \mathbf{L}^k \quad (2.22)$$

where M_c^k , \mathbf{V}_c^k , \mathbf{I}^k , \mathbf{L}^k and ω^k are the total mass, centre-of-mass velocity, moment of inertia tensor, angular momentum and angular velocity of the k^{th} suspended particle, respectively. The total mass of the k^{th} suspended particle $M_c^k = \sum_{i=1}^{n_{cp}} (m_i^k + \bar{m}_i^k)$, in which m_i^k is the mass of constituent particle i , \bar{m}_i^k the mass of reference site i .

The net force \mathbf{F}^k and torque \mathbf{T}^k (also moment or moment of force) on the k^{th} colloidal particle are expressed as

$$\mathbf{F}^k(t) = \sum_{i=1}^{n_{cp}} \sum_{j=1, j \neq i}^N [\mathbf{F}_{ij,C}^k(t) + \mathbf{F}_{ij,D}^k(t) + \mathbf{F}_{ij,R}^k(t)] , \quad (2.23)$$

$$\mathbf{T}^k(t) = \sum_{i=1}^{n_{cp}} (\mathbf{r}_i^k(t) - \mathbf{R}_c^k(t)) \times \sum_{j=1, j \neq i}^N [\mathbf{F}_{ij,C}^k(t) + \mathbf{F}_{ij,D}^k(t) + \mathbf{F}_{ij,R}^k(t)] , \quad (2.24)$$

where n_{cp} is the number of constituent particles of the k^{th} colloidal particle; $N = N^s + N^c$ is the total number of DPD particles, including the number of solvent particles N^s and constituent particles N^c ; \mathbf{R}_c^k is the center of mass of the k^{th} colloidal particle

$$\mathbf{R}_c^k = \frac{1}{M_c^k} \sum_{i=1}^{n_{cp}} (m_i^k \mathbf{r}_i^k + \bar{m}_i^k \bar{\mathbf{r}}_i^k) . \quad (2.25)$$

The reference sites are advanced according to

$$\frac{d\bar{\mathbf{r}}_i^k}{dt} = \mathbf{V}_c^k + \omega^k \times (\bar{\mathbf{r}}_i^k - \mathbf{R}_c^k) , \quad i = \overline{1, n_{cp}} . \quad (2.26)$$

Updating the information for the constituent particles is performed similarly to the solvent particles, where the total force on the constituent particle is

$$\mathbf{F}_i^k(t) = \sum_{j=1, j \neq i}^N [\mathbf{F}_{ij,C}^k(t) + \mathbf{F}_{ij,D}^k(t) + \mathbf{F}_{ij,R}^k(t)] + \mathbf{F}_{i,S}^k(t) , \quad (2.27)$$

with $\mathbf{F}_{i,S}^k(t) = -H [\mathbf{r}_i^k(t) - \bar{\mathbf{r}}_i^k(t)]$ being the spring force, H is the stiffness of the spring.

Remark: (i) conditions for a spherical suspended particle include the requirement that reference sites should be located regularly, (ii) number density of solvent is kept unchanged as the colloidal particles are added.

2.4 Summary and implication for DPDs

There are still many challenges for the DPD, which include (i) equation of state, (ii) no formal way of deriving DPD from an atomistic system for simple fluids (unbonded atoms), (iii) energy equation, (iv) issues of thermal fluctuation scaling, (v) specification of physical properties of fluids, and (vi) boundary conditions.

In this project we have attempted to address the issues related to thermal fluctuation scaling and specification of physical properties of a model fluid. Apart from those, we have extended DPD to its generalised hydrodynamics, and improved numerical results for the investigation of complex fluids, in particular the prediction of viscosities of particulate suspensions.

Chapter 3

Proposed DPD method in the hydrodynamic limit

In this chapter, a Dissipative Particle Dynamics (DPD) method is employed with its input parameters directly determined from the (physical) fluid properties such as the mass density, water compressibility and viscosity. The investigation of thermal fluctuation scaling requires the fluid properties be constant, and the physical input version of DPD is shown to meet this requirement. Its numerical verifications in simple or complex fluids and in viscometric or non-viscometric flows indicate respectively that (i) the level of thermal fluctuations in the DPD model for both types of fluids is consistently reduced with increasing coarse-graining level; and (ii) viscometric or non-viscometric flows of a model fluid at different coarse-graining levels have a similar behaviour. Furthermore, to reduce the compressibility effects of the DPD fluid in simulating incompressible flows, a new simple treatment is presented and shown to be very effective.

1 Introduction

Dissipative particle dynamics (DPD) is a simulation technique designed for modelling complex fluids, primarily in the mesoscale domains [Hoogerbrugge and Koelman (1992), Español and Warren (1995), Español (1995), Marsh (1998)]. In this scheme, the system is thermally equilibrated through a thermostat formed by the dissipative and random forces. DPD conserves momentum locally and therefore preserves hydrodynamics. The method has been used to simulate various fluid systems, for example, particulate suspensions [Pan et al. (2010b), Panchenko et al. (2018), Nie et al. (2019)], microfluidic systems [Li et al. (2013)], red blood cells [Ye et al. (2014)], thixotropic materials [Le-Cao et al. (2017)], polymer solutions [Kong et al. (1997)], etc. In DPD, the solvent phase is simply modelled by a set of particles (called DPD particles) under their Newton second law motions, while the suspended phases (*e.g.*, solid particles, droplets, bubbles and polymer chains) can all be constructed from the DPD particles through appropriate constraints. With its simplicity, there are several issues in the DPD method related to (i) a fixed equation of state; (ii) no formal way of deriving DPD from an atomistic system for simple fluids (unbonded atoms); (iii) energy equation; (iv) issues of thermal fluctuation scaling; and (v) fluid properties specification [Liu et al. (2015), Español and Warren (2017), Ellero and Español (2018)]. There have been many attempts made to improve the standard DPD formulation. For example, the many-body DPD was introduced in Pagonabarraga and Frenkel [Pagonabarraga and Frenkel (2001)] to produce an arbitrary equation of state. To deal with non-isothermal problems, the energy conserving DPD was developed by Bonet Avalos and Mackie [Avalos and Mackie (1997)] and Español [Español (1997)] independently. Mai-Duy *et al.* [Mai-Duy et al. (2017b), Mai-Duy et al. (2017a)] made use of analytic expressions from the kinetic theory due to [Marsh (1998)] (see also [Phan-Thien and Mai-Duy (2017)]) to derive good estimates for the fluid

viscosity, its compressibility, its time-scale ratio and its dynamic response – these physical fluid properties can now be specified as input parameters to the DPD fluid. Note that the viscosity and mass density here are defined in terms of DPD units which are the mass of a single DPD particle (\bar{m}), force cut-off radius (\bar{r}_c) and thermal energy ($\overline{k_B T}$).

As a particle-based method, DPD may suffer from the effect of compressibility. The compressibility of a DPD fluid was investigated in several works. For example, in [Kim and Phillips (2004)], it was observed that, due to the compressibility effect, the DPD prediction of the drag force acting on a sphere is no longer accurate when the Reynolds number is greater than 100. In [van de Meent et al. (2008)], the coherent structures of the transition to turbulence in compressible shear flows with DPD was investigated, where the speed of sound in a DPD fluid is obtained by measuring the speed of propagation of a density pulse. In [Pan et al. (2013)], two test models were proposed, where both the density and the divergence of the velocity field are considered. It was reported that the condition of constant density and divergence-free of velocity can be approximately achieved at large values of the repulsion parameter. In [Phan-Thien et al. (2014b)], reducing the particles' mass was shown to be an effective way to induce an incompressible slow viscous flow in a DPD fluid and simultaneously enhance its dynamic response.

DPD is a coarse-graining technique for the simulation of fluids at the mesoscale, where hydrodynamics and thermos fluctuations have a role. There was concern that the process of coarse-graining in DPD has its upper limit that would prevent the method from widespread use. By taking into account the dependence of the parameters in the model on the level of coarse-graining, the DPD and the many-body DPD were shown to be truly mesoscopic methods in [Füchslin et al. (2009)] and [Arienti et al. (2011)], respectively. With the scaling schemes presented in

[Füchslin et al. (2009),Arienti et al. (2011)], the DPD methods can be applied to any desired length scale, where different physical systems can share some physical properties such as compressibility (but not viscosity, to be discussed later).

It should be pointed out that the DPD can be employed in its generalised hydrodynamic regime, where the transport coefficients are dependent on the wavelengths and frequencies of thermal fluctuations and through which finite-size effects can be taken into account [Ripoll et al. (2001),Phan-Thien et al. (2018),Mai-Duy et al. (2020)].

In this chapter, we will examine numerically the “physical input” version of DPD, and focus on its coarse graining and scaling, and its compressibility. In the study of thermal fluctuation scaling, the fluid properties (e.g., mass density, compressibility and viscosity) should remain invariant with respect to the coarse-graining level. We will show that this requirement can be met by scaling the original DPD inputs in a way that can make the pre-determined input values unchanged. It is observed that the thermal fluctuations reduce in magnitude with higher coarse-graining levels, and the flows of a model fluid at different coarse-graining levels are demonstrated to have similar behaviours. In our study, compressibility of the model fluid is also matched to that of water. To reduce unwanted compressibility effects, a simple way based on the time-scale ratio is proposed and shown to be very effective.

The remainder of the chapter is organised as follows. A brief review of DPDs with classical and explicit input parameters is given in Section 2. In section 3, the coarse graining process is shown to achieve a consistent thermal fluctuation scaling. Its flow behaviour and some means of reducing unwanted compressibility effects of the DPD fluid are presented and discussed in sections 4 and 5, respectively. Section 6 gives some concluding remarks.

2 DPD with explicit input parameters

One main drawback of the classical DPD formulation is that there is no direct link between the DPD input parameters and the macroscopic properties of the fluid. In the DPD adopted here, the fluid viscosity, compressibility, dynamics response and time-scale ratio can be specified in advance, as discussed in [Mai-Duy et al. (2017b), Mai-Duy et al. (2017a)]. Expressions for the conservative and dissipative forces are designed to have two free parameters. For the conservative force, the two parameters are used to match the time-scale ratio and compressibility. For the dissipative force, they are used to match the fluid density and dynamic response. When the physical fluid properties can be demonstrated to remain constant, we can investigate the effects of the number density, thermal energy and cut-off radius on the flow behaviour.

The weighting functions for the conservative force are chosen as $w_C = (1 - r/r_c)^{\bar{s}}$. From the virial theorem, the equation of state relating the pressure with the particle number density can be derived as [Mai-Duy et al. (2017a)]

$$p = nk_B T + \frac{4\pi a_{ij} n^2 r_c^4}{(\bar{s} + 1)(\bar{s} + 2)(\bar{s} + 3)(\bar{s} + 4)}, \quad \text{for 3D space,} \quad (3.1)$$

$$p = nk_B T + \frac{\pi a_{ij} n^2 r_c^3}{(\bar{s} + 1)(\bar{s} + 2)(\bar{s} + 3)}, \quad \text{for 2D space.} \quad (3.2)$$

The two free parameters, a_{ij} and \bar{s} in function w_C , are designed to satisfy given values of the time-scale ratio α [Mai-Duy et al. (2017a)] and the isothermal compressibility κ [Groot and Warren (1997), Groot and Rabone (2001), Füchslin et al. (2009)], according to

$$\alpha = \frac{\tau}{\tau_I} = \frac{\gamma^2 r_c}{m a_{ij}}, \quad (3.3)$$

$$\kappa^{-1} = \frac{1}{k_B T} \frac{\partial p}{\partial n}, \quad (3.4)$$

In (3.3), τ and τ_I are the relaxation time and inertia time scales of the stochastic differential equation (2.1), respectively: $\tau = O(\gamma H^{-1}) = O(\gamma r_c a_{ij}^{-1})$ and $\tau_I = O(m\gamma^{-1})$, in which H is the stiffness defined as $H = O(|\partial_r F_C|) = O(a_{ij} r_c^{-1})$. The time-scale ratio α can be utilised to keep the dissipative and conservative forces balanced; its values can be acquired from some numerical experiments in simple flows, and the best α , according to numerical studies published in Mai-Duy et al. (2017a), is in the range of 10^{-1} to 10^{+1} . In (3.4), p is the pressure, $n = n_{phys}/\nu$ (n_{phys} : the molecular number density and ν : the number of molecules per DPD particle/the coarse-graining level) and $\kappa = 1/15.98$ for water. The system, (3.3) and (3.4), can be solved analytically for the two variables a_{ij} and \bar{s} , given α and κ , where

$$a_{ij} = \frac{1}{\alpha} \frac{\gamma^2 r_c}{m}, \quad (3.5)$$

and

$$\bar{s} = \frac{\sqrt{5 + 4\sqrt{C + 1}} - 5}{2}, \quad C = \frac{8\pi a_{ij} n r_c^4}{(\kappa^{-1} - 1)k_B T}, \quad (3.6)$$

for 3D space,

$$\bar{s} = \frac{1}{3B} + B - 2, \quad B = \left(\frac{C}{2} + \sqrt{\frac{C^2}{4} - \frac{1}{27}} \right)^{1/3}, \quad C = \frac{2\pi a_{ij} n r_c^3}{(\kappa^{-1} - 1)k_B T}, \quad (3.7)$$

for 2D space. It is noted that $\partial p/\partial n$ in (3.4) is explicitly expressed in terms of the cut-off radius, resulting in C as a function of r_c , and an appropriate choice of r_c can allow the DPD model to be applied at any high coarse-graining level (scale-free property/truly mesoscopic method) [Füchslin et al. (2009)]. For (3.6) and (3.7) to have a physical value ($\bar{s} > 0$), we require $C > 24$ and $C > 6$, respectively, which can be easily satisfied.

The weighting functions for the dissipative force are chosen as $w_D = (1 - r/r_c)^{1/2}$. From the kinetic theory, there are two contributions to the viscosity, the kinetic part (gaseous contribution) and the dissipative part (liquid contribution).

Here, we are interested in the case where the dissipative contribution is dominant (liquid-like behaviour). The input/specified viscosity, namely η , of the DPD system is imposed by enforcing the following constraint

$$\bar{\eta}_D = \frac{\gamma n^2 [R^2 w_D]_R}{2d(d+2)} = \eta, \quad (3.8)$$

in which $\bar{\eta}_D$ is the dissipative viscosity predicted by the kinetic theory, d is the dimension number (2 or 3) and $[R^2 w_D]_R \equiv \int d\mathbf{R} R^2 w_D(R)$ ($= 1024\pi r_c^5/3465$ for 3D space and $64\pi r_c^4/315$ for 2D space). This equation can be solved for the variable γ :

$$\gamma = \frac{51975\eta}{512\pi n^2 r_c^5}, \quad 3\text{D}, \quad (3.9)$$

$$\gamma = \frac{315\eta}{4\pi n^2 r_c^4}, \quad 2\text{D}. \quad (3.10)$$

If the Schmidt number/speed of sound is taken as an additional input to the DPD equation (2.1), the weighting functions for the dissipative force are employed in the form of $(1 - r/r_c)^s$. One can then use two parameters s and γ to match the viscosity and dynamic response

$$\bar{\eta}_D = \eta, \quad (3.11)$$

$$\frac{\bar{\eta}}{\rho D} = S_c, \quad D = \frac{2\bar{\eta}_K}{\rho}, \quad \bar{\eta} \simeq \bar{\eta}_D, \quad (3.12)$$

where S_c is the Schmidt number, and $\bar{\eta}_K$ and $\bar{\eta} = \bar{\eta}_K + \bar{\eta}_D$ are the kinetic viscosity and the viscosity predicted by the kinetic theory. In 3D space, the parameters s and γ take the form

$$s = \frac{-9 + \sqrt{1 + 4C}}{2}, \quad C = \frac{6S_c m k_B T n^2 r_c^2}{5\eta^2}, \quad (3.13)$$

$$\gamma = \frac{5\eta(s+1)(s+2)(s+3)(s+4)(s+5)}{16\pi n^2 r_c^5}. \quad (3.14)$$

Since $s > 0$, it requires

$$\eta < \sqrt{\frac{3S_c m k_B T n^2 r_c^2}{50}} \quad \text{for a given } S_c, \quad (3.15)$$

$$S_c > \frac{50\eta^2}{3m k_B T n^2 r_c^2} \quad \text{for a given } \eta. \quad (3.16)$$

In 2D, the two parameters are

$$s = \frac{-7 + \sqrt{1 + 4C}}{2}, \quad C = \frac{3S_c m k_B T n^2 r_c^2}{4\eta^2}, \quad (3.17)$$

$$\gamma = \frac{4\eta(s+1)(s+2)(s+3)(s+4)}{3\pi n^2 r_c^4}. \quad (3.18)$$

Since $s > 0$, it requires

$$\eta < \sqrt{\frac{S_c m k_B T n^2 r_c^2}{16}} \quad \text{for a given } S_c, \quad (3.19)$$

$$S_c > \frac{16\eta^2}{m k_B T n^2 r_c^2} \quad \text{for a given } \eta. \quad (3.20)$$

New features of the proposed DPD lie in converting the original input parameters (e.g. the strengths of the repulsion, dissipative and random forces) into the input parameters that have physical meanings (e.g. fluid compressibility, viscosity and Schmidt number). The computational part of the proposed DPD is the same as that of conventional DPDs. Since analytic expressions for the conversion for the input parameters are derived, there is not much difference in computational cost between the proposed and conventional DPDs.

3 Coarse graining and scaling

In Füchslin *et al.* [Füchslin et al. (2009)], a physical system represented by N_{phys} molecular particles is to be scaled (coarse-grained) at different levels ν so

that one deals with a smaller number of particles

$$N = \frac{N_{phys}}{\nu}, \quad (3.21)$$

in which $\nu = N_{phys}/N$ is referred to as the coarse-graining level. Two different coarse-graining levels are considered, ν and ν' (modelled by $\{N, k_B T, n, m, r_c, a, \gamma\}$ and $\{N', k_B T', n', m', r'_c, a', \gamma'\}$, respectively). It is noted that the upper-case N is used to denote the number of particles in the flow domain, while the lower-case n is used to denote the number particle density. Their relations in three dimensions are established as ($\phi = \nu'/\nu$ is the scaling)

$$\begin{aligned} N' &= \phi^{-1}N, & k_B T' &= \phi k_B T, & n' &= \phi^{-1}n, \\ m' &= \phi m, & r'_c &= \phi^{1/3}r_c, & \tau' &= \phi^{1/3}\tau, \\ a' &= \phi^{2/3}a, & \gamma' &= \phi^{2/3}\gamma, & \sigma' &= \phi^{5/6}\sigma, \end{aligned} \quad (3.22)$$

where τ and τ' are time scales. With these scalings, it can be shown that DPD is a scale-free (truly mesoscopic) method. In the DPD, one typically employs the mass of a single DPD particle, the force cut-off radius and thermal energy as the basic units. The time, mass, length and viscosity of the system are thus not defined explicitly but in terms of these DPD units. We use the superposed bar to denote a dimensional quantity and define the unit of mass, length and energy as \bar{m}/β_m , \bar{r}_c/β_r and $\bar{k_B T}/\beta_T$, respectively, where β_m , β_r and β_T are values of the cut-off radius, mass and thermal energy to be employed in the dimensionless system. If $\beta_m = \beta_r = \beta_T = 1$, one has a standard reduced unit system. When going from one coarse-graining level to the other, β_m , β_r and β_T will stay the same. One may rewrite the dimensionless stochastic equation (2.1) without the

external force in the following dimensional differential form

$$\begin{aligned}\Delta \bar{\mathbf{r}}_i &= \bar{\mathbf{v}}_i \Delta \bar{t}, \\ \bar{m} \Delta \bar{\mathbf{v}}_i &= \sum_j \bar{a}_{ij} w_C(\bar{r}_{ij}) \mathbf{e}_{ij} \Delta \bar{t} - \sum_j \bar{\gamma} w_D(\bar{r}_{ij}) (\mathbf{e}_{ij} \cdot \bar{\mathbf{v}}_{ij}) \mathbf{e}_{ij} \Delta \bar{t} \\ &\quad + \sum_j \bar{\sigma} w_R(\bar{r}_{ij}) \theta_{ij} \mathbf{e}_{ij} \sqrt{\Delta \bar{t}}.\end{aligned}\tag{3.23}$$

Let's scale length by \bar{r}_c/β_r , mass by \bar{m}/β_m , and time by $\bar{\tau}$ (which later chosen as $(\bar{r}_c/\beta_r)\sqrt{(\bar{m}/\beta_m)/(\bar{k}_B \bar{T}/\beta_T)}$) and define dimensionless variables:

$$m = \frac{\bar{m}}{\bar{m}/\beta_m} = \beta_m, \quad \mathbf{r} = \frac{\bar{\mathbf{r}}}{\bar{r}_c/\beta_r}, \quad t = \frac{\bar{t}}{\bar{\tau}}, \quad \frac{d}{dt} = \frac{d}{\bar{\tau} dt}, \quad \mathbf{v} = \frac{\bar{\mathbf{v}}}{\bar{r}_c/\beta_r}.\tag{3.24}$$

Dimensional equations of motion (3.23) then reduce to

$$\begin{aligned}\Delta \mathbf{r}_i &= \mathbf{v}_i \Delta t, \\ \beta_m \Delta \mathbf{v}_i &= \sum_j \frac{\bar{a}_{ij} \bar{\tau}^2}{(\bar{m}/\beta_m)(\bar{r}_c/\beta_r)} w_C(r_{ij}) \mathbf{e}_{ij} \Delta t - \sum_j \frac{\bar{\gamma} \bar{\tau}}{(\bar{m}/\beta_m)} w_D(r_{ij}) (\mathbf{e}_{ij} \cdot \mathbf{v}_{ij}) \mathbf{e}_{ij} \Delta t \\ &\quad + \sum_j \frac{\bar{\sigma} \bar{\tau}^{3/2}}{(\bar{m}/\beta_m)(\bar{r}_c/\beta_r)} w_R(r_{ij}) \theta_{ij} \mathbf{e}_{ij} \sqrt{\Delta t}.\end{aligned}\tag{3.25}$$

By defining new dimensionless parameters as

$$a_{ij} = \frac{\bar{a}_{ij} \bar{\tau}^2}{(\bar{m}/\beta_m)(\bar{r}_c/\beta_r)}, \quad \gamma = \frac{\bar{\gamma} \bar{\tau}}{(\bar{m}/\beta_m)}, \quad \sigma = \frac{\bar{\sigma} \bar{\tau}^{3/2}}{(\bar{m}/\beta_m)(\bar{r}_c/\beta_r)},\tag{3.26}$$

the dimensionless equations of motion become

$$\begin{aligned}\Delta \mathbf{r}_i &= \mathbf{v}_i \Delta t, \\ \beta_m \Delta \mathbf{v}_i &= \sum_j a_{ij} w_C(r_{ij}) \mathbf{e}_{ij} \Delta t - \sum_j \gamma w_D(r_{ij}) (\mathbf{e}_{ij} \cdot \mathbf{v}_{ij}) \mathbf{e}_{ij} \Delta t \\ &\quad + \sum_j \sigma w_R(r_{ij}) \theta_{ij} \mathbf{e}_{ij} \sqrt{\Delta t}.\end{aligned}\tag{3.27}$$

with the thermal equilibrium requiring

$$2\overline{k_B T} \overline{\gamma} = \overline{\sigma}^2,$$

or

$$2\overline{k_B T} \overline{\gamma} \frac{(\overline{m}/\beta_m)}{\overline{\tau}} = \overline{\sigma}^2 \frac{(\overline{m}/\beta_m)^2 (\overline{r}_c/\beta_r)^2}{\overline{\tau}^3}.$$

Thus the scaling

$$\overline{\tau} = (\overline{r}_c/\beta_r) \sqrt{\frac{(\overline{m}/\beta_m)}{(\overline{k_B T}/\beta_T)}} \quad (3.28)$$

will guarantee the thermal equilibrium of the DPD system (3.27):

$$2\beta_T \overline{\gamma} = \overline{\sigma}^2 \quad \text{or} \quad 2k_B T \gamma = \sigma^2. \quad (3.29)$$

It can be seen that every system with the same values of

$$a_{ij} = \frac{\overline{a}_{ij}(\overline{r}_c/\beta_r)}{(\overline{k_B T}/\beta_T)}, \quad \gamma = \frac{\overline{\gamma}(\overline{r}_c/\beta_r)}{((\overline{m}/\beta_m)(\overline{k_B T}/\beta_T))^{1/2}}, \quad \sigma^2 = \frac{\overline{\sigma}^2(\overline{r}_c/\beta_r)}{(\overline{m}/\beta_m)^{1/2}(\overline{k_B T}/\beta_T)^{3/2}} \quad (3.30)$$

will have the same state space. Making use of (3.22), the three dimensionless parameters scale as

$$\frac{a'_{ij}(r'_c/\beta_r)}{(k_B T'/\beta_T)} = \phi^{2/3+1/3-1} \frac{a_{ij}(r_c/\beta_r)}{(k_B T/\beta_T)} = \frac{a_{ij}(r_c/\beta_r)}{(k_B T/\beta_T)}, \quad (3.31)$$

$$\frac{\gamma'(r'_c/\beta_r)}{((m'/\beta_m)(k_B T'/\beta_T))^{1/2}} = \phi^{2/3+1/3-1/2-1/2} \frac{\gamma(r_c/\beta_r)}{((m/\beta_m)(k_B T/\beta_T))^{1/2}} = \frac{\gamma(r_c/\beta_r)}{((m/\beta_m)(k_B T/\beta_T))^{1/2}}, \quad (3.32)$$

$$\frac{\sigma'^2(r'_c/\beta_r)}{(m'/\beta_m)^{1/2}(k_B T'/\beta_T)^{3/2}} = \phi^{5/3+1/3-1/2-3/2} \frac{\sigma^2(r_c/\beta_r)}{(m/\beta_m)^{1/2}(k_B T/\beta_T)^{3/2}} = \frac{\sigma^2(r_c/\beta_r)}{(m/\beta_m)^{1/2}(k_B T/\beta_T)^{3/2}}, \quad (3.33)$$

indicating that the two coarse-graining systems are stochastically equivalent. Using (3.22), let's examine the relations for the mass density, compressibility and

viscosity, respectively,

$$\rho' = (m'/\beta_m) n' = \phi^{1-1} (m/\beta_m) n = \rho \text{ (invariant)} \quad (3.34)$$

$$\frac{a' n' (r'_c/\beta_r)^4}{(k_B T'/\beta_T)} = \phi^{2/3-1+4/3-1} \frac{a n (r_c/\beta_r)^4}{(k_B T/\beta_T)} = \frac{a n (r_c/\beta_r)^4}{(k_B T/\beta_T)} \text{ (invariant)} \quad (3.35)$$

$$\gamma' n'^2 (r'_c/\beta_r)^5 = \phi^{2/3-2+5/3} \gamma n^2 (r_c/\beta_r)^5 = \phi^{1/3} \gamma n^2 (r_c/\beta_r)^5 \text{ (not invariant)} \quad (3.36)$$

With this scaling scheme, different coarse-graining levels will have the same mass density and compressibility but different viscosities.

In the present DPD formulation, there are two additional parameters, \bar{s} and s , which make the relations for the parameters between two coarse-graining levels generally more complicated than those in (3.22). When the particle number is reduced ($n' = \phi^{-1}n$, $\phi > 1$), we also take ($m' = \phi m$), increase the cut-off radius ($r'_c > r_c$), but keep not only the water compressibility but also the viscosity and the Schmidt number (where appropriate) constant. Values of (a_{ij} , \bar{s} , γ , s) and (a'_{ij} , \bar{s}' , γ' , s') are derived from expressions (3.5), (3.6), (3.9), (3.13) and (3.14) in three dimensions and (3.5), (3.7), (3.10), (3.17) and (3.18) in two dimensions for given sets of ($k_B T$, α , η , (S_c)) and ($k_B T'$, $\alpha' = \alpha$, $\eta' = \eta$, ($S'_c = S_c$)), respectively. These scalings can be easily obtained numerically. Note that (i) \bar{s} is a function of (κ , a_{ij} , n , r_c , $k_B T$), s a function of (S_c , η , m , n , r_c , $k_B T$), a_{ij} a function of (α , r_c , m , γ), and γ a function of (η , s , n , r_c); and (ii) If S_c is not a specified value, the parameter s is taken to be 1/2.

The thermal fluctuations in the present scaling scheme are studied for both simple and complex fluid systems. A consistent scaling of thermal fluctuations means that their magnitude becomes smaller with larger particle volumes [Vázquez-Quesada et al. (2009)].

3.1 Simple fluids

We consider some Newtonian fluid modelled by $\alpha = 1$, $\eta = 30$, $k_B T = 1$, water-like compressibility and constant mass density ($\rho = mn = 8$). Three coarse-graining levels employed with $n = \{8, 6, 4\}$, $m = \{1, 4/3, 2\}$ and $r_c = \{1, 1.1006, 1.2599\}$ are taken to represent the model fluid. Here, β_m , β_r and β_T are chosen to be 1. In this case, the length unit is a force cut-off radius (\bar{r}_c), the mass unit is the mass of a DPD particle (\bar{m}), and the energy unit is the thermal energy ($\bar{k}_B T$) resulting in the time unit $\tau = \bar{r}_c \sqrt{\bar{m}/\bar{k}_B T}$. The domain is chosen as $15 \times 15 \times 15$ (in DPD units). For r_c , the scaling factor used is the same as

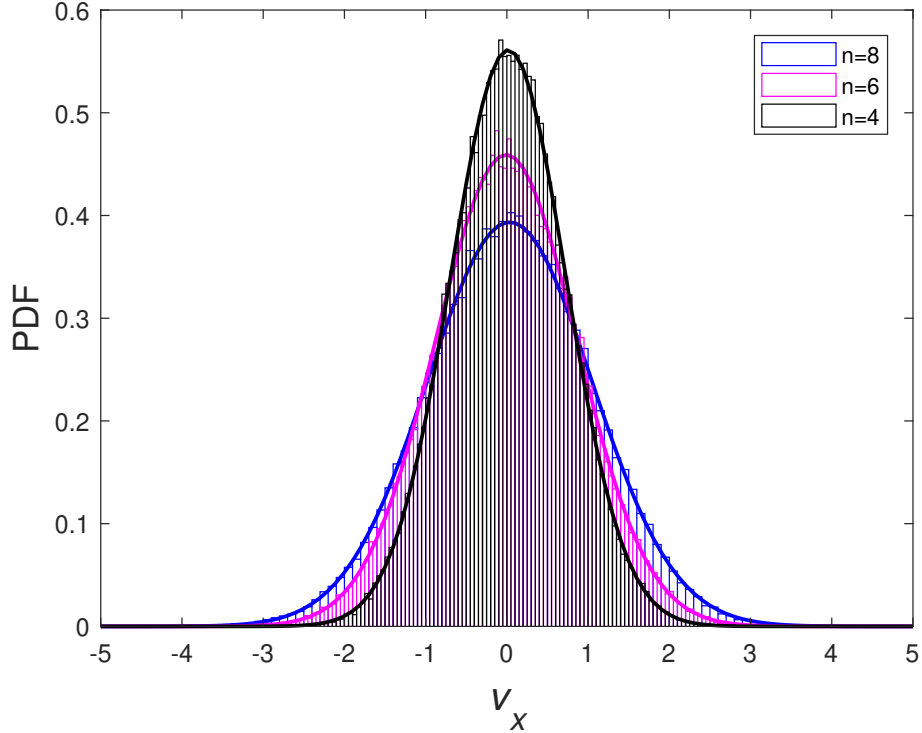


Figure 3.1: Simple fluid with water-like compressibility, $\alpha = 1$, $\eta = 30$ and $\rho = mn = 8$; $L_x \times L_y \times L_z = 15 \times 15 \times 15$; $s = 0.5$; $k_B T = 1$; and $\Delta t = 0.001$: Probability density function (PDF) of v_x of a DPD particle at 3 different coarse-graining levels ($n = \{8, 6, 4\}$; $r_c = \{1, 1.1006, 1.2599\}$; $m = \{1, 4/3, 2\}$). Thermal fluctuations are reduced (variance: 1.0272, 0.7546, 0.5054) with larger particle size.

that in (3.22), i.e. $\phi^{1/3}$. The volume of particles can be regarded as $V_i \sim 1/n$.

The results on the distribution of the velocity component of a DPD particle are shown in Figure 3.1. It can be seen that the thermal fluctuations are reduced with lower number densities (larger particle sizes). Note that from the kinetic theory, the Schmidt number is estimated as 290 for $n = 8$, 319 for $n = 6$ and 365 for $n = 4$.

3.2 Particulate suspensions

We consider the suspension of a single rigid particle in a Newtonian fluid. The solvent phase is modelled with $\alpha = 1$, $\eta = 30$, $\rho = mn = 8$, $k_B T = 1$ and water compressibility, and the colloidal particle is constructed using the spring model [Phan-Thien et al. (2014a)]. The domain is chosen as $15 \times 15 \times 15$ (in DPD units). In the first test, we employ 3 different coarse-graining levels with $n = \{8, 6, 4\}$, $r_c = \{1, 1.1006, 1.2599\}$ and $m = \{1, 4/3, 2\}$ for the solvent and keep the volume fraction of the suspended phase constant. For the spring model, the volume fraction is also the particle fraction because the standard/basic DPD particles are used to represent both the constituent and solvent particles. Let N_C^0 be the number of basic DPD particles used to represent the colloidal phase and N_S be the number of basic particles used for the solvent phase, the volume fraction is computed as $\phi = N_C^0 / (N_C^0 + N_S)$.

In the present problem (one colloidal particle), by taking the number of constituent particles per colloid as the (solvent) particle number density, the volume fraction remains invariant: $\phi = 1 \times n / (1 \times n + Vn) = 1 / (1 + V) = 2.96 \times 10^{-4}$ (V : the box volume) for any value of n . Using the radial distribution function (RDF) to measure the exclusion of the colloidal particle at three coarse-graining levels, they all lead to similar results - the size of the exclusion zone is about 0.475 in DPD units. As in Section 3.1, the standard reduced unit system is employed here, i.e. $\beta_m = \beta_r = \beta_T = 1$. The results are displayed in Figure 3.2, showing the

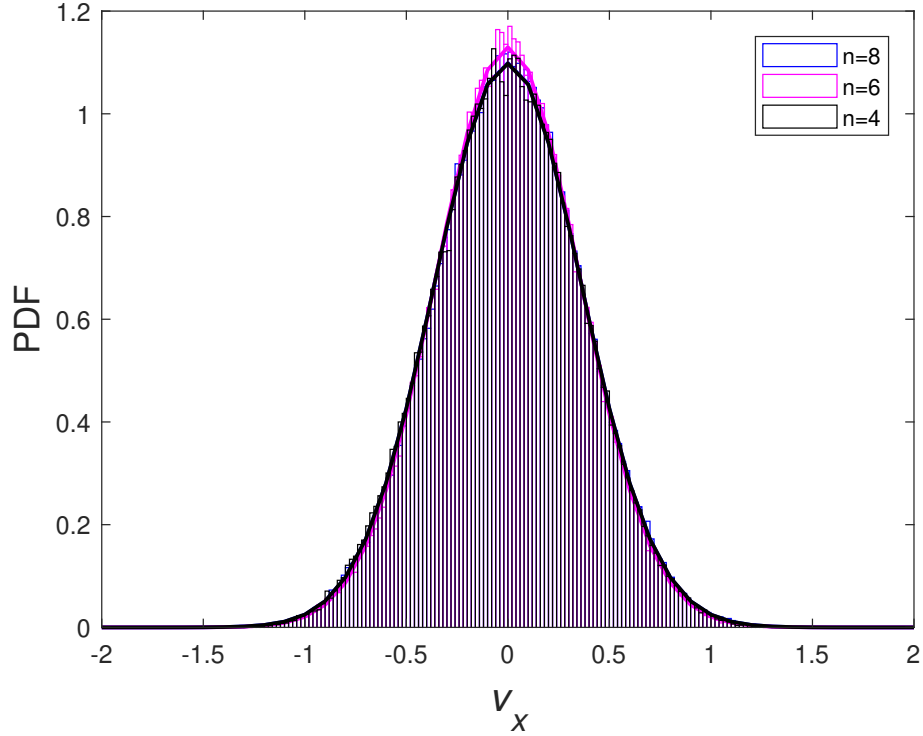


Figure 3.2: Suspension with water-like compressibility, $\alpha = 1$, $\eta = 30$ and $\rho = 8$ for the solvent phase; constant volume fraction for the suspended phase; $L_x \times L_y \times L_z = 15 \times 15 \times 15$; $k_B T = 1$; and $\Delta t = 0.001$: Probability density function (PDF) of v_x of a single colloidal particle in the solvent employed at 3 different coarse-graining levels ($n = \{8, 6, 4\}$; $r_c = \{1, 1.1006, 1.2599\}$; $m = \{1, 4/3, 2\}$). Its computed variances are similar (0.1318, 0.1247, 0.1321).

change of n (solvent particle's size) does not affect the level of thermal fluctuations of the colloidal particle.

In the second test, we employ $n = 8$, $r_c = 1$, $m = 1$ and $S_c = 600$ for the solvent and the colloid of three different sizes, i.e. 6, 12 and 20 DPD particles per colloid (by means of RDF, sizes of exclusion zones are measured as 0.30, 0.36 and 0.51 in DPD units, respectively). The results are displayed in Figure 3.3, indicating that the thermal fluctuations of the colloid are reduced with its larger size.

For the standard DPD method, the exponents of the weighting functions in the dissipative and repulsive forces are fixed. For the present DPD method, these exponents are variables and they are functions of the viscosity, Schmidt num-

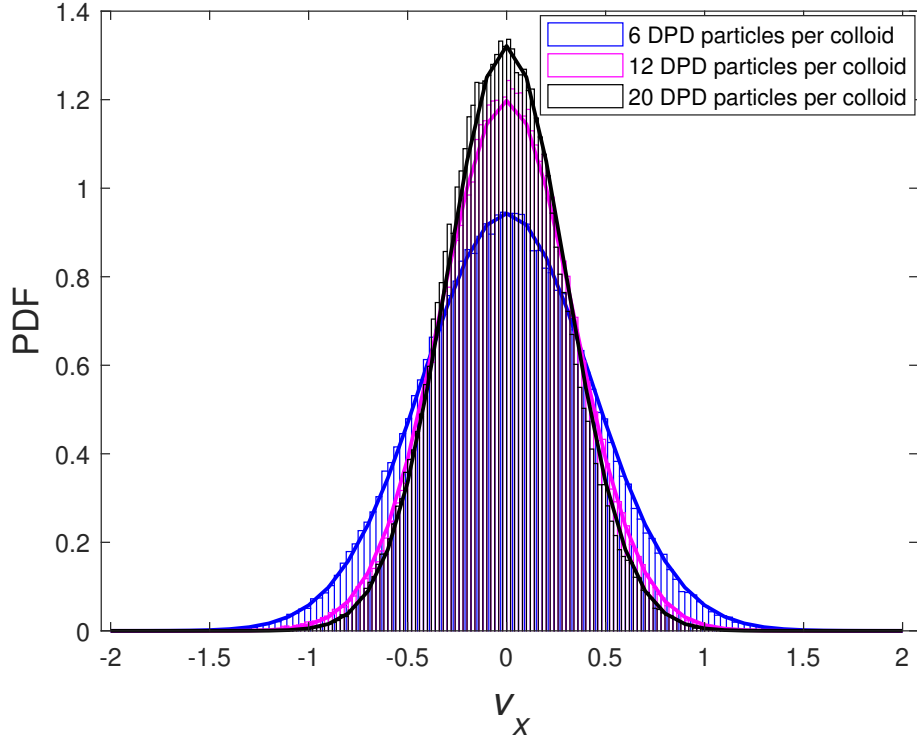


Figure 3.3: Suspension with the solvent phase: water-like compressibility, $\alpha = 1$, $\eta = 30$, $\rho = mn = 8$ and $S_c = 600$; $L_x \times L_y \times L_z = 15 \times 15 \times 15$; $k_B T = 1$; and $\Delta t = 0.001$: Probability density function (PDF) of v_x of a single colloidal particle employed with 3 different sizes at the same solvent coarse graining level ($n = 8$, $r_c = 1$, $m = 1$). Thermal fluctuations of the colloid are reduced (variance: 0.1790, 0.1109, 0.0912) with its larger size.

ber, fluid compressibility and time-scale ratio. For the test in Section 3.1 (simple fluids) and the first test in Section 3.2 (particulate suspensions), different coarse-graining levels are considered. When going from one coarse-graining level to the other, one has different fluids for the standard DPD and the same fluid for the present DPD. The standard DPD is thus not directly applicable to the study of thermal fluctuation scaling for these tests. For the second test, only one coarse-graining level for the solvent is considered. The exponents of the weighting functions in the dissipative and repulsive forces all stay the same when changing the size of the colloid particle. In this regard, the present DPD can be considered as the standard DPD and these two versions are expected to produce similar

results.

Figure 3.4 shows a comparison of thermal fluctuations between the standard

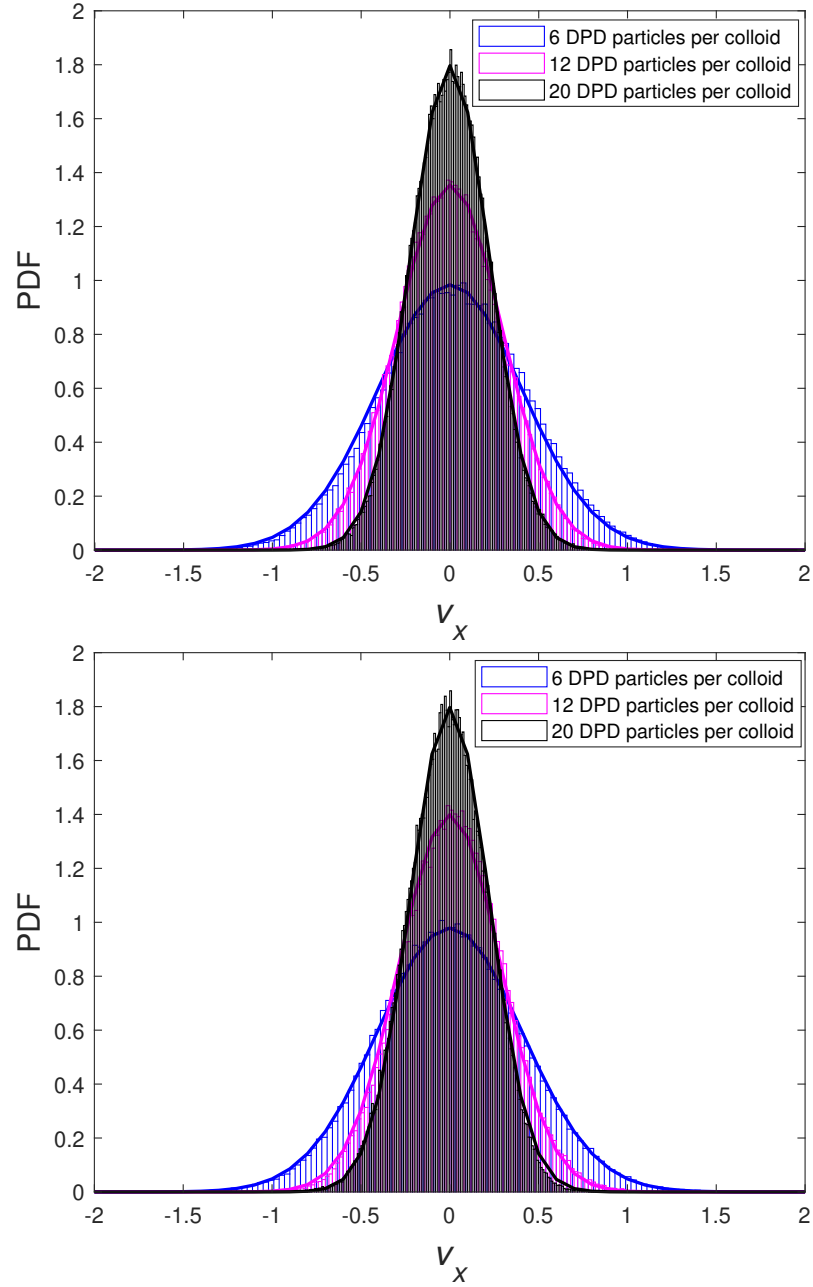


Figure 3.4: Probability density function (PDF) of v_x of a single colloidal particle employed with 3 different sizes at the same solvent coarse graining level by the standard (top) and present (bottom) DPDs. It can be seen that the two methods produce similar behaviours. When the size of the colloidal particle is increased, thermal fluctuations of the colloid are reduced (variance: 0.1643, 0.0867 and 0.0493 for the standard DPD and 0.1661, 0.0812, 0.0492 for the present DPD).

DPD and the present DPD. The former is employed with $n = 4, r_c = 1.5, m = 1, k_B T = 1, \bar{s} = 1, s = 1/2, \sigma = 3$ and $a_{ij} = 3.5320$, which lead to, by means of kinetic theory, $\alpha = 8.5997, \eta = 16.9721$ and $S_c = 1.6452 \times 10^2$. The latter is employed with $n = 4, r_c = 1.5, m = 1, k_B T = 1, \alpha = 8.5997, \eta = 16.9721$ and $S_c = 1.6452 \times 10^2$. Similar behaviours are obtained, and when the size of the colloidal particle is increased, thermal fluctuations of the colloid are reduced (variance: 0.1643, 0.0867 and 0.0493 for the standard DPD and 0.1661, 0.0812, 0.0492 for the present DPD).

These tests demonstrate that the present DPD method has a proper scaling with respect to its thermal fluctuations.

4 Flows of the model fluid at different coarse-graining levels

For the viscosity approximation taken in the form of (3.8), its error depends on the two quantities n and r_c . Using the kinetic theory as a guide, the total viscosity $\bar{\eta}$ of the DPD system is computed as

$$\bar{\eta} = \frac{3}{5} \frac{\rho k_B T n r_c^2}{\eta(s+4)(s+5)} + \eta, \quad (3.37)$$

where η is the input viscosity and ρ is the fluid density. In (3.37), the first term on RHS is the kinetic viscosity, which should be designed to be negligible. As a result, for a given set of η, ρ and $k_B T$, one needs to reduce r_c if there is an increase in n (smaller mean distance between particles). In our numerical experiments conducted in Sections 4.1 and 4.2, the product of n and r_c as well as $k_B T$ are kept constant. For r_c , between two coarse-graining levels, the scaling

factor is chosen as ϕ . For $k_B T$, the scaling factor is chosen as $\phi^{3/2}$ according to

$$k_B T' = k_B T, \quad (3.38)$$

or

$$m' \frac{r_c'^2}{\tau'^2} = m \frac{r_c^2}{\tau^2}, \quad (3.39)$$

or

$$\frac{\tau'}{\tau} = \frac{r_c'}{r_c} \sqrt{\frac{m'}{m}} = \phi \phi^{1/2} = \phi^{3/2}. \quad (3.40)$$

4.1 Double Poiseuille flows

This flow is simulated in two dimensions. By dividing the domain of analysis into two equal regions by the line $y = 0$ and then assigning an acceleration $\mathbf{g} = (F_e/m, 0) = (1, 0)$ to each particle in the upper region ($y > 0$) and $\mathbf{g} = (-1, 0)$ to each particle in the lower region ($y < 0$), a periodic Poiseuille flow is produced with the theoretical values of the velocity and shear stress: $u_x = \rho g_x y (L_y/2 - y)/(2\eta)$ and $\tau_{xy} = \rho g_x (L_y/2 - 2y)/2$, where $0 \leq y \leq L_y/2$. The simulation results for the double Poiseuille flows are shown in Figure 3.5, where three different sets of $\{n, r_c, m\}$ are employed as $\{8, 1, 1\}$, $\{6, 4/3, 4/3\}$ and $\{4, 2, 2\}$ corresponding to 3200, 2400 and 1600 particles, respectively, over the flow domain. Other input parameters are $\eta = 30$, $\alpha = 1$, $k_B T = 1$, $\Delta t = 0.001$ and 300000 time steps. Here, the standard reduced unit system is employed, i.e. $\beta_m = \beta_r = \beta_T = 1$. The domain is chosen as 20×20 (in DPD units). It can be seen from Figure 3.5 that both velocities and shear stresses at the three coarse-graining levels have similar behaviours and they are in a good agreement with the theoretical values.

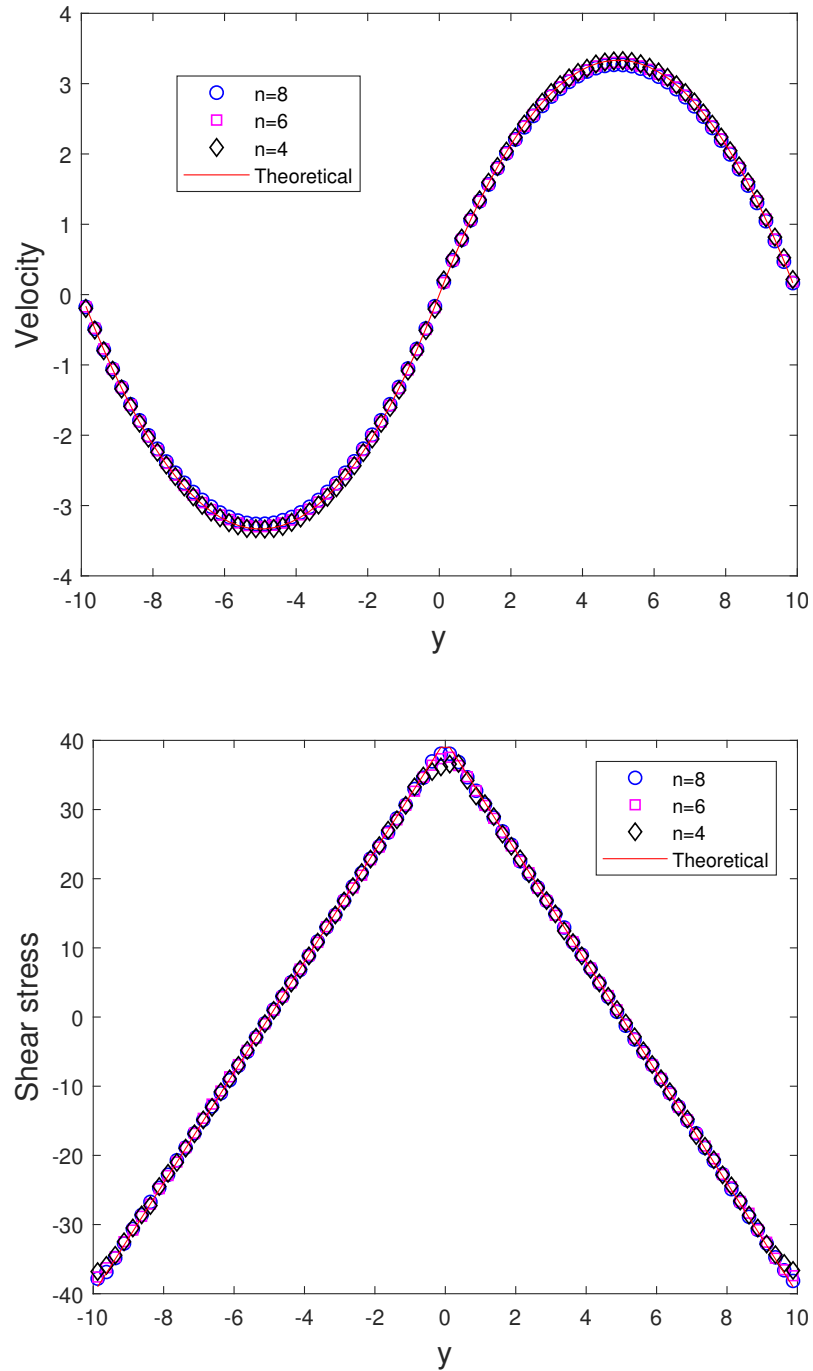


Figure 3.5: Poiseuille flow: Some typical results by the present DPD at $n = \{8, 6, 4\}$. Theoretical values for velocity and shear stress are also included.

4.2 Flow past a periodic square array of fixed cylinders

For this type of flow, the analysis can be carried out in two dimensions. Because of its periodicity, one can replace the infinite domain with a cell volume containing one cylinder. Assume that the motion of a fluid is driven by a pressure drop in the x direction. Consider some Newtonian fluid defined by $\eta = 100$, $\rho = nm = 4$, $nr_c = 16$, $k_B T = 1$ and $\alpha = 1$. Three coarse-graining levels using relatively small values of the number density ($n = \{10, 8, 6\}$) are employed to represent the model fluid. Here, β_m , β_r and β_T are chosen to be 0.4, 1.6 and 1, respectively. In this case, the mass unit is the mass of a DPD particle divided by β_m , i.e. $\bar{m}/0.4$, the length unit is a force cut-off radius divided by β_r , i.e. $\bar{r}_c/1.6$, and the energy unit is the thermal energy $\overline{k_B T}$ resulting in the time unit $\tau = (\bar{r}_c/1.6)\sqrt{(\bar{m}/0.4)/\overline{k_B T}}$. A cell is chosen as $L_x \times L_y = 10 \times 10$ (in DPD units). A cylinder is constructed with the spring model [Phan-Thien et al. (2014a)]. For $n = 8$, as shown in Figure 3.6, the number of constituent particles used to model a cylinder are chosen as 19 and they are located at the cylinder's centre and at the distances $r_1 = 0.1(1/n_x + 1/n_y)/2 = 0.1(1/2 + 1/4)/2 = 0.0375$ ($n_x n_y = n$) and $r_2 = 2r_1$, in which $(1/n_x + 1/n_y)/2$ is regarded as the mean distance between the solvent particles, and the factor 0.1 is introduced to prevent the fluid particles from penetrating the cylinder. For other values of n , cylinders are also constructed in a similar manner, except that the constituent particles are chosen in a way that the ratio of the number of constituent particles to the total number of particles in the system (particle fraction) is kept constant, i.e. 0.0232.

Fluid-fluid and fluid-cylinder radial distribution functions (RDFs) at no-flow conditions for three values of the number density are displayed in Figure 3.7.

If the exclusion zone is defined as an area where the value of RDF is less than 0.01, then the cylinders are of similar sizes (about 0.47) and the sizes of the fluid particles can be negligible. The small (negligible) size of the fluid particle is

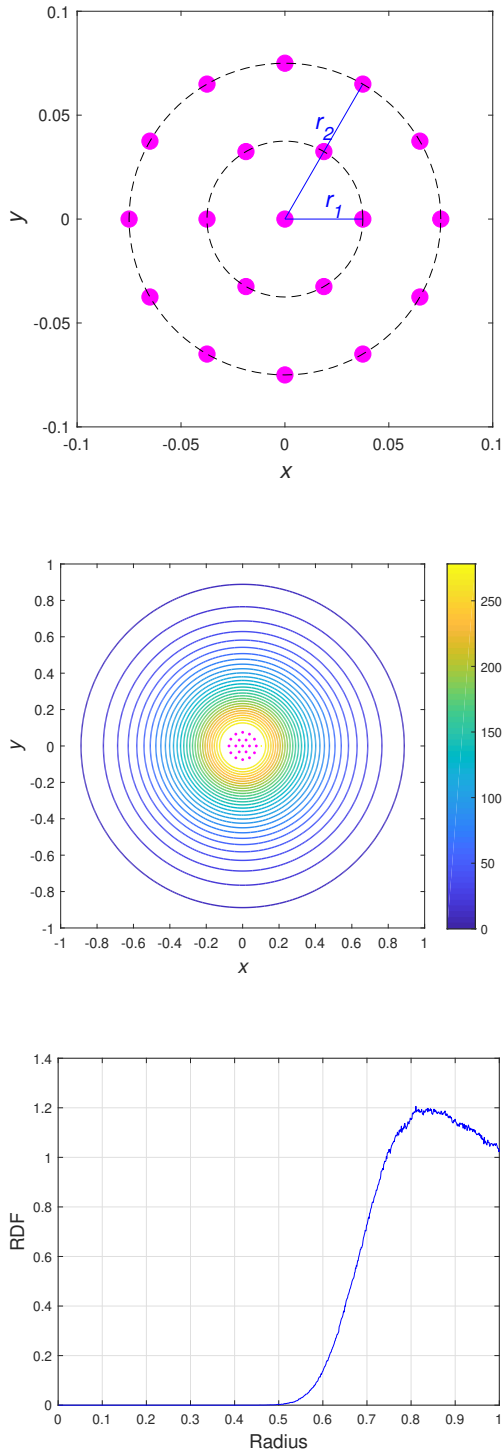


Figure 3.6: Modelling of the fixed cylinder with the surrounding fluid defined by $\{\eta = 100, n = 8, r_c = 2, m = 0.5, k_B T = 1, \alpha = 1\}$: Reference sites of constituent particles of the cylinder (top), its repulsion force field in the radial direction (middle) and fluid-cylinder radial distribution function at no-flow conditions (bottom). Note that, for both constituent and fluid particles, $F_{ij,C} = 23.96(1 - r/r_c)^{6.67}$.

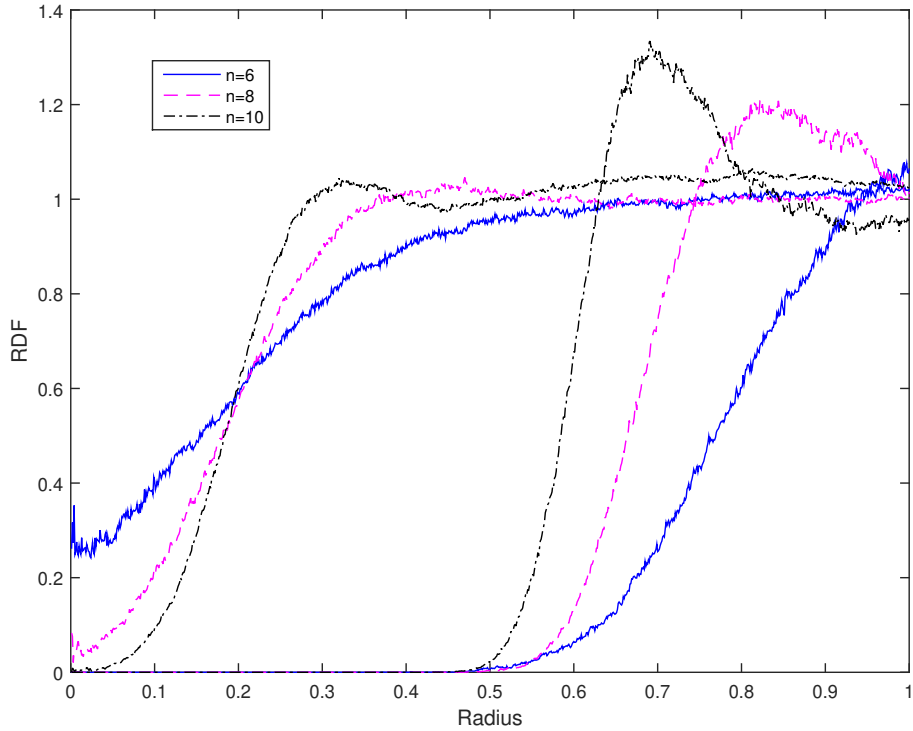


Figure 3.7: Flows past a periodic array of fixed cylinders: Fluid-fluid (left) and fluid-cylinder (right) radial distribution functions for different number densities at no-flow conditions: By defining the exclusion zone as an area where the RDF values are less than 0.01, the cylinders for different resolutions are of similar sizes (about 0.47), and the fluid particle sizes can be negligible.

mainly due to the use of large r_c (greater than 1) as discussed in [Mai-Duy et al. (2015)].

We impose a wide range of the body force ($F_e = \{0.01, 0.02, \dots, 0.10, 0.12, \dots, 0.30\}$) on the fluid particles in the x direction to drive the fluid motion. The flows here are slow flows with their Reynolds numbers ($Re = \rho UL/\eta$) being less than 0.2 (L and U : the distance between the cylinders and mean velocity in the x direction), the diffusion time scale $t = \rho L^2/\eta = 4$ and the convection time scale $t = L/U \simeq 20$ (for the maximum value of U). For these flows ($Re < 0.2$), one can have a wide choice of the size ratio of the cylinder to the solvent particle in the simulation without causing spurious behaviour, and the diffusion time scale is important as the Peclet number, which measures the ratio of the convection

and the diffusion terms, is small, i.e. $Pe = \rho LU/\eta \simeq 0.2$.

Figure 3.8 show the effects of the imposed body force on the cylinder's size and the fluid particle's size. It can be seen that the sizes of the cylinder and fluid particles are not much affected by the change in the imposed fore.

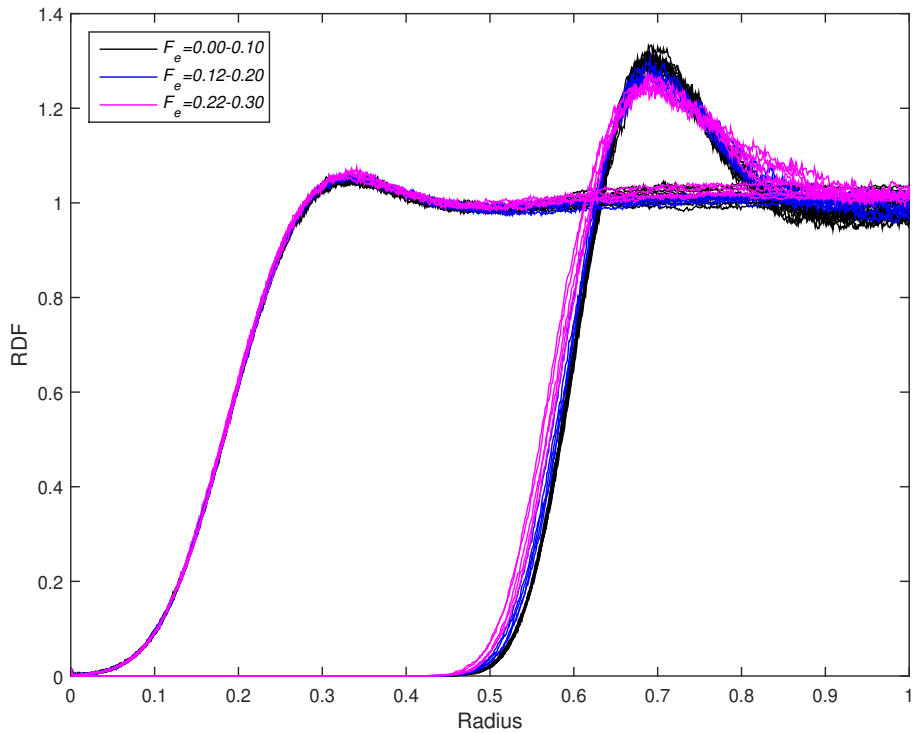


Figure 3.8: Flows past a periodic array of cylinders, $n = 8$: Fluid-fluid (left) and fluid-cylinder (right) radial distribution functions for different imposed body forces $F_e = (0, 0.01, 0.02, \dots, 0.10, 0.12, \dots, 0.30)$. Their sizes are generally well maintained over the range of the body force applied.

Figure 3.9 displays the obtained drag forces on the three coarse-graining levels. It can be seen that their behaviours are similar in trend and their values are in good agreement at low values of the mean flow velocity. As the imposed body force is increased, the compressibility effect of the DPD fluid may be significant and special attention is needed (Figure 3.10). It will be further discussed in Section 5. The analytic results obtained by Hashimoto [Hashimoto (1959)] using Fourier series are also included for comparison purposes. It appears that lower coarse-

graining levels or higher values of n (higher speeds of sound - see equation (3.42), lower Mach numbers) produce better predictions of the drag force as the imposed body force (the mean flow velocity) is reduced.

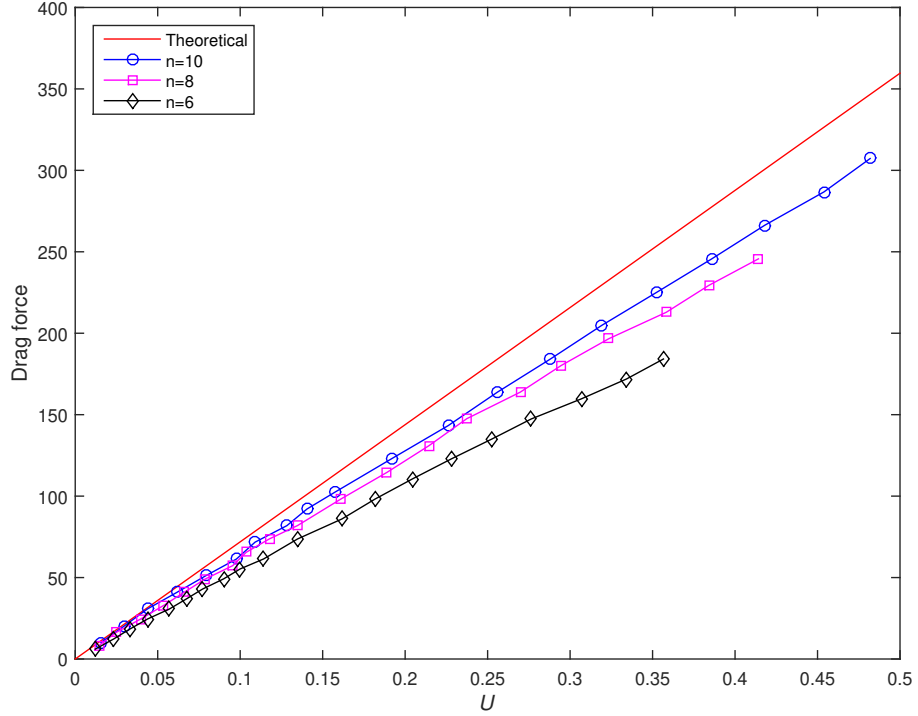


Figure 3.9: Flows past a periodic array of cylinders: Drag forces against the mean flow velocity U for three coarse-graining levels with the body forces imposed as $F_e = (0.01, 0.02, \dots, 0.10, 0.12, \dots, 0.30)$. The three cases have similar behaviours in trend and their values are in better agreement as U is reduced.

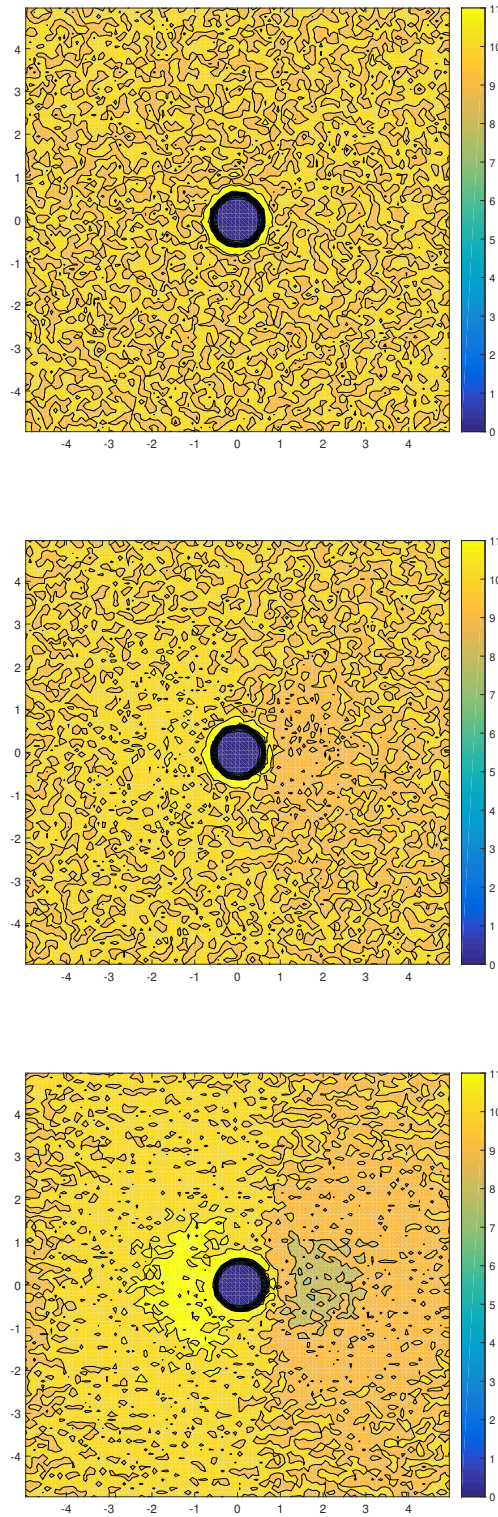


Figure 3.10: Flows past a periodic array of cylinders, $n = 10$: Distribution of the number density in a cell for 3 typical values of the imposed body force ($F_e = 0$ top; $F_e = 0.1$ middle, and $F_e = 0.3$ bottom). Attention is needed with increasing F_e due the effects of compressibility of the model fluid.

5 Reducing unwanted compressibility effects

Like any fluid that is modeled by a set of particles, a DPD fluid is compressible. Special attention is thus needed when simulating incompressible flows. In [Groot and Warren (1997),Phan-Thien et al. (2014b)], water compressibility was enforced in the DPD system. In [Phan-Thien et al. (2014b)], in addition, the particles' mass was proposed to reduce in order to increase the speed of sound. In the present context (DPD with physical inputs), compressibility of the DPD fluid is matched to water. We investigate the effects of using lower mass and also propose a new means that can further reduce unwanted compressibility effects.

We measure compressibility of the DPD fluid by the density residual defined as

$$\Delta n = \sqrt{\frac{\sum_{i=1}^{N_b} (n_i - n)^2}{N_b}}, \quad (3.41)$$

where N_b is the number of bins, n_i the number density of the i th bin and n the reference number density.

5.1 The mass approach

Expression for the speed of sound of the DPD fluid is given by [Marsh (1998)]

$$c_s^2 = \frac{k_B T}{m} + \frac{\pi}{15} \frac{a n r_c^4}{m} \quad (3.42)$$

If the particle's mass is reduced, it leads to a higher speed of sound as well as a lower Reynolds number and a smaller diffusion time scale. When the Mach number ($M = U/c_s$, U is a flow characteristic velocity) is less than 0.3, the flow may be regarded as an incompressible flow. On the other hand, one has to deal with overdamped (stiff) systems, for which much smaller time steps are required for a proper simulation. This can be alleviated by means of the stochastic

exponential time differencing (SETD) scheme [Phan-Thien et al. (2014b)]. For a given number density, reducing m leads to fluids of different mass densities.

5.2 The time-scale ratio approach

The time-scale ratio ($\alpha = \tau/\tau_I$) relates to the conservative and dissipative forces. This dimensionless quantity can thus be used to control the quantitative relation between the two forces. It will be demonstrated that varying α can lead to a significant improvement in the distribution of the number density over the flow domain. Unlike the use of low mass, the mass density of the model fluid will not be affected by the change in α .

First, we examine the performance of the SETD scheme. Consider a Couette

Table 3.1: Couette flows, $U = 1, \eta = 100, n = 10, r_c = 1.6, k_B T = 1, \alpha = 10, L_x \times L_y = 10 \times 10$, 100 bins per unit area and 10^6 time steps: Comparison of the mean thermal energy of the velocity-Verlet and SETD schemes for $m = 0.01$. The former fails to converge at $\Delta t \geq 2.5 \times 10^{-4}$.

Δt	Velocity-Verlet		SETD	
	$\overline{k_B T}$	Error(%)	$\overline{k_B T}$	Error(%)
5.0×10^{-4}	-	-	0.4928	50.7
2.5×10^{-4}	-	-	0.7717	22.8
1.0×10^{-4}	0.8917	10.82	0.9525	4.74
7.5×10^{-5}	0.9164	8.36	0.9723	2.76
5.0×10^{-5}	0.9422	5.78	0.9871	1.28
2.5×10^{-5}	0.9696	3.03	0.9959	0.41
1.0×10^{-5}	0.9872	1.28	0.9984	0.15

flow with the imposed shear rate $\dot{\gamma} = 0.2$. The two plates move with the same velocity U but in opposite direction. The mass is specified as $m = \beta_m = 0.01$ and some other input parameters are $\eta = 100, n = 10, k_B T = \beta_T = 1, \alpha = 10, r_c = \beta_r = 1.6$ and 100 bins per a unit area. Note that the mass unit is the

mass of a DPD particle divided by β_m , i.e. $\bar{m}/0.01$, the length unit is the force cut-off radius divided by β_r , i.e. $\bar{r}_c/1.6$. The simulations are carried out on the domain $L_x \times L_y = 10 \times 10$ (in DPD units) with 10^6 time steps. Table 3.1 displays computed values of the mean thermal energy by the velocity-Verlet and SETD schemes for different times steps, which show that larger time steps and better accuracy are acquired with the latter.

The obtained results concerning the number density by the mass and time-scale approaches are displayed in Figure 3.11 for simple flows and in Figure 3.12 for complex flows. Here, Couette flow is chosen as an example for simple flows.

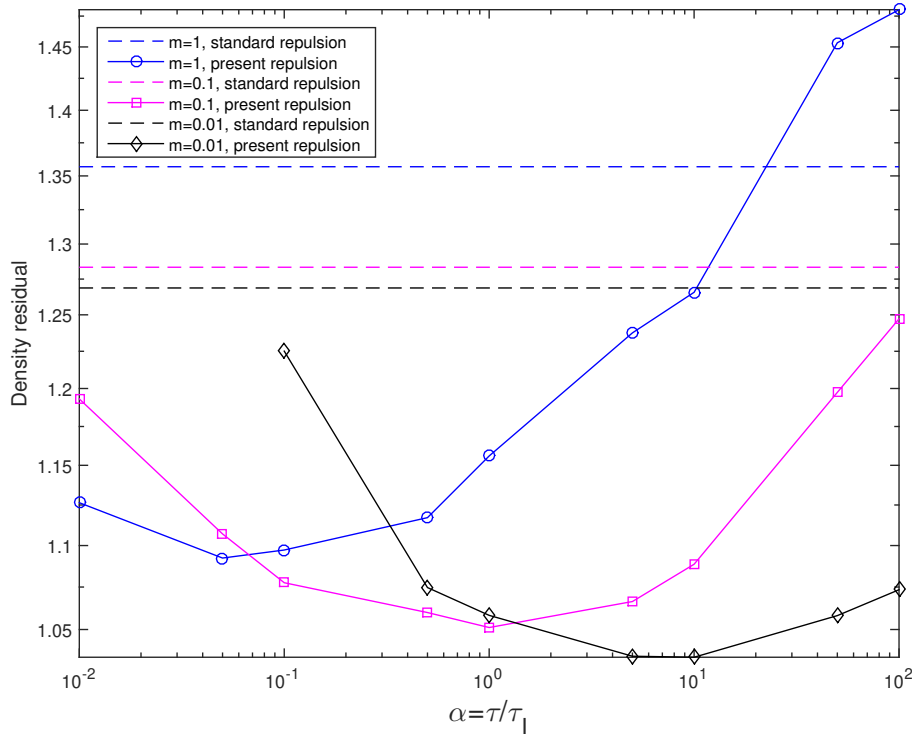


Figure 3.11: Couette flows, $\eta = 100$, $n = 10$, $\Delta t = 0.0001$, $L_x \times L_y = 10 \times 10$, $U = 1$, $r_c = 1.6$, $k_B T = 1$, 100 bins per unit area and 10^6 time steps: Density residual against time-scale ratio for 3 typical values of m . Values of α used are $(10^{-2}, 5 \times 10^{-2}, 10^{-1}, 5 \times 10^{-1}, \dots, 10^2)$. Results with the standard repulsion are also included. Changing the value of α can lead to a significant improvement in the distribution of number density over the flow domain.

The density residual is observed to reduce with a decreasing mass (1.3568 for

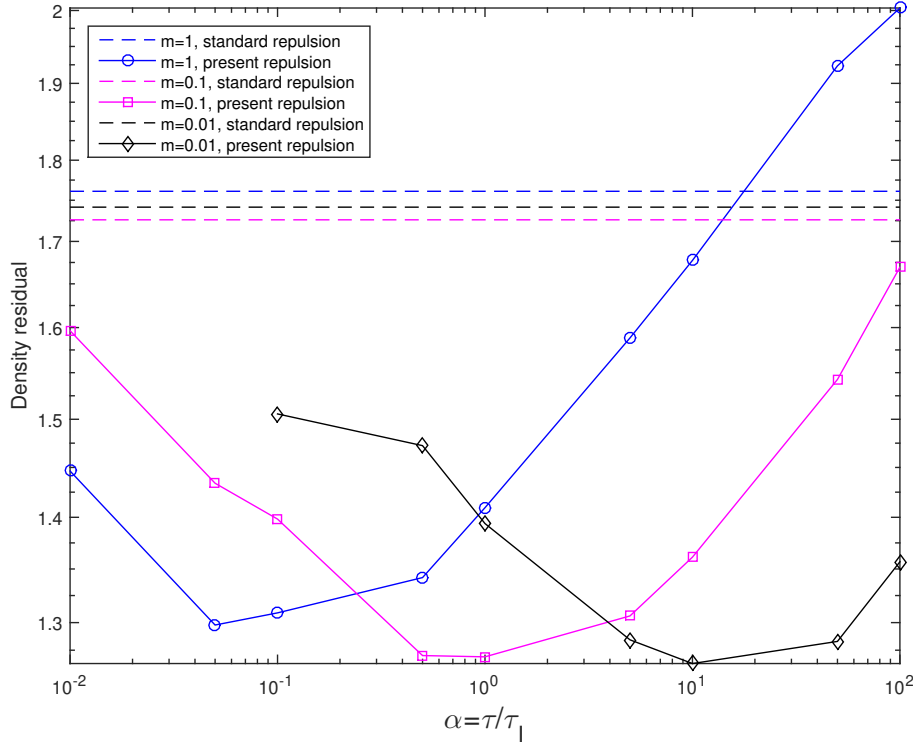


Figure 3.12: Flows past a periodic square of cylinders, $\eta = 100$, $n = 10$, $\Delta t = 0.0001$, $L_x \times L_y = 10 \times 10$, $F_e = 0.3$, $r_c = 1.6$, $k_B T = 1$, 100 bins per unit area and 10^6 time steps: Density residual against time-scale ratio for 3 typical values of m . Values of α used are $(10^{-2}, 5 \times 10^{-2}, 10^{-1}, 5 \times 10^{-1}, \dots, 10^2)$. Results with the standard repulsion are also included. Changing the value of α can lead to a significant improvement in the distribution of number density over the flow domain.

$m = 1$, 1.2833 for $m = 0.1$ and 1.2687 for $m = 0.01$). Taking $U = 1$ and $L = 5$ ($\dot{\gamma} = 0.2$), the Reynolds number is 0.5 for $m = 1$, 0.05 for $m = 0.1$ and 0.005 for $m = 0.01$. For a given m , by changing the value of α , it can be seen that a significant improvement in the number density distribution is achieved without affecting the fluid mass density. Also, varying α for $m = 1$ yields better results than the case of low mass $m = 0.01$ with standard repulsion. As expected, the optimal value of $\alpha = \tau/\tau_I$ increases as the mass is reduced (smaller inertia time). For any mass employed here, a simple selection of $\alpha = 1$ is still able to lead to reasonable results when compared to the case of standard repulsion. Turning to

complex flows: flow past an array of fixed cylinders, similar remarks can be made here. The Reynolds number is approximately 0.2 for $m = 1$, 0.02 for $m = 0.1$ and 0.002 for $m = 0.01$. It appears that varying α is more effective and efficient than reducing the particles' mass.

Figure 3.13 shows that the variations of α for simple and complex flows have similar behaviours. It can be seen that their minimum density residuals all occur in the range $\alpha = 0.01 - 1$. A simple mechanism to find the optimal value of α can thus be suggested. For a given set of DPD input parameters, the simulation is first conducted on some simple flows (*e.g.* Couette flow) and the obtained best value of α can then be utilised in the simulation of the flow of interest.

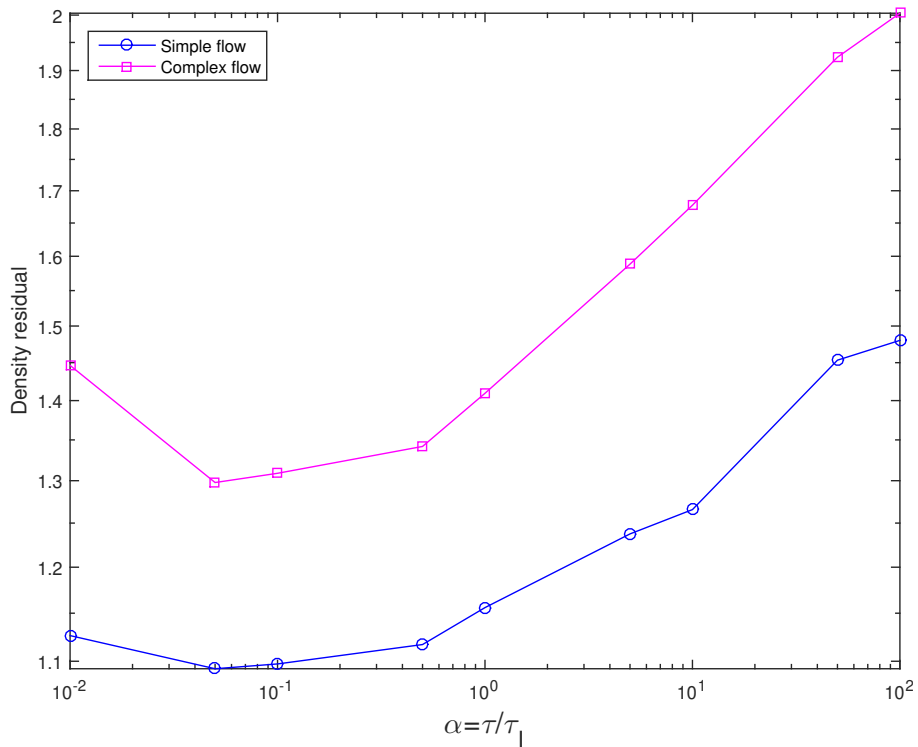


Figure 3.13: Density residual against time-scale ratio for Couette flows ($U = 1$) and flows past a periodic square array of cylinders ($F_e = 0.3$) with $\eta = 100$, $n = 10$, $\Delta t = 0.0001$, $L_x \times L_y = 10 \times 10$, $r_c = 1.6$, $k_B T = 1$, 100 bins per unit area and 10^6 time steps. Values of α used are $(10^{-2}, 5 \times 10^{-2}, 10^{-1}, 5 \times 10^{-1}, \dots, 10^2)$. The two flows have similar optimal values of α .

6 Concluding remarks

In this chapter, the DPD simulations are conducted with the viscosity, compressibility, dynamic response (where appropriate) and time-scale ratio being specified as input parameters, from which a consistent scaling of thermal fluctuations and similar behaviours of the flow at different coarse-graining levels have been demonstrated. The issue of compressibility is also studied. Reducing the particles' mass and/or varying the time-scale ratio can reduce unwanted compressibility effects. The advantages of the time-scale ratio approach over the low mass approach are (i) one still has the same model fluid (constant viscosity, water compressibility and mass density) without the need to change other input parameters; and (ii) a much improved result for the number density distribution can be achieved. Attractive features from the use of physical input parameters are expected to allow an effective DPD scheme to simulate (nearly) incompressible multiphase flows to be developed.

Chapter 4

Proposed DPD method in generalised hydrodynamics

In this chapter, we show that a Dissipative Particle Dynamics (DPD) model of a viscous Newtonian fluid may actually produce a linear viscoelastic fluid. We demonstrate that a single set of DPD particles can be used to model a linear viscoelastic fluid with its physical parameters, namely the dynamical viscosity and the relaxation time in its memory kernel, determined from the DPD system at equilibrium. The emphasis of this study is placed on (i) the estimation of the linear viscoelastic effect from the standard parameter choice; and (ii) the investigation of the dependence of the DPD transport properties on the length and time scales, which are introduced from the physical phenomenon under examination. Transverse-current auto-correlation functions (TCAF) in Fourier space are employed to study the effects of the length scale, while analytic expressions of the shear stress in a simple small amplitude oscillatory shear flow are utilised to study the effects of the time scale. A direct mechanism for imposing the particle diffusion time and fluid viscosity in the hydrodynamic limit on the DPD system is also proposed.

1 Introduction

As already shown in section 2.2, for preceding standard descriptions of the DPD interaction parameters, the DPD system is actually a Newtonian fluid on a long-time average [Marsh (1998)]. In this chapter, we explore the generalised hydrodynamics regime of the DPD fluid that is defined by equations (2.1)-(2.7), where typical length scales include the interaction range r_c and the dynamic correlation length l_0 defined as $l_0 = v_0 t_0$ in which v_0 and t_0 are, respectively, the thermal velocity and collision time (or kinetic time) [Marsh (1998)]

$$v_0 = \sqrt{\frac{k_B T}{m}}, \quad (4.1)$$

$$t_0 = \frac{1}{\omega_0}, \quad \omega_0 = \frac{1}{3} n [w_D] \gamma, \quad [w_D] = 4\pi r_c^3 \left[\frac{1}{1+s} - \frac{2}{2+s} + \frac{1}{3+s} \right]. \quad (4.2)$$

The classification of dynamic regimes in DPD can be based on the two length scales, r_c and l_0 : “particle” regime when $r_c < l_0$ and “collective” regime when $r_c > l_0$. In our study, the focus is on a collective regime. Note that if one takes $n = \{3, 4\}$, $r_c = 1$, $m = 1$, $\sigma = 3$ and $k_B T = 1$ (commonly used input values), then the above estimates yield $l_0 = \{0.5305, 0.3979\}$ for $s = 2$ (standard DPD fluids) and $l_0 = \{0.1161, 0.087\}$ for $s = 1/2$ (modified DPD fluids), all less than $r_c = 1$.

Let λ be the wavelength ($k = 2\pi/\lambda$ is the wave number) of a perturbation in the hydrodynamics, which can be regarded as the length scale on which the physical phenomena under examination occur. On the other hand, the correlation length l_0 forms a scale on which the DPD transport coefficients are defined. As $k \rightarrow 0$ and the observation time scale is large, the system behaves like a continuum (the NS equations/hydrodynamics limit). At finite k , the system can be described by a linearised form of the NS equations, where local deviations of the macroscopic variables (the number density and momentum density) from their average values

are assumed to be small. As discussed in [Ripoll et al. (2001)], a standard hydrodynamic regime occurs on the range $l_0 < r_c < \lambda$ while a mesoscopic hydrodynamic regime on $l_0 < \lambda < r_c$. In addition, there is a smooth transition between these two hydrodynamic regimes, which occurs at about $k_c = 2\pi/r_c$. The generalised hydrodynamics cover both the standard and the mesoscopic hydrodynamics and thus can be probed by considering linearised NS equations induced by perturbations. The transport coefficients are now functions of k , and their values at $k = 0$ can be estimated through extrapolation. In practice, an effective way to predict the DPD transport coefficients over a wide range of k is to employ the transverse-current autocorrelation functions (TCAF) in Fourier space.

Let ω be a characteristic frequency ($T = 1/\omega$ is a characteristic time). Assume that our (non-Newtonian) fluid in question has a characteristic time scale λ_t . If $T \gg \lambda_t$, the observation time scale is large and the material responds like a fluid; otherwise, one may have a solid-like response. For a linear viscoelastic fluid, the stress at the current time is dependent not only on the current strain rate but also the past strain rate; in 1D,

$$S(t) = \int_{\gamma(-\infty)}^{\gamma(t)} G(t-t')d\gamma(t') = \int_{-\infty}^t G(t-t')\dot{\gamma}dt', \quad (4.3)$$

where $\dot{\gamma}$ is the shear rate (γ is the shear strain) and G is a decreasing function of time, the relaxation modulus. In the case of a simple shear flow, the stress analysis can be done in an exact manner. One can utilise its analytic solution to examine the effects of the frequency on the DPD transport properties.

The above discussions on the dependence of DPD transport coefficients on the wavelength and frequency are general. In our study, we restrict our attention to the standard version of DPD (equations (2.1)-(2.7)) in its generalised hydrodynamics.

One particular concern here is how to make a direct link between the fluid physi-

cal parameters and the (input) DPD parameters. We attempt to derive, by means of kinetic theory [Marsh (1998)] and by using generalised forms of the dissipative weighting function, the relation between the particle diffusion time and the viscosity of the fluid (at the hydrodynamic limit), and the DPD parameters. The resultant analytic expressions allow one to specify these two physical parameters as the input parameters.

The remainder of this chapter is organised as follows. In Sections 2 and 3, brief reviews of TCAF and analytic expressions of the shear stress in a simple small amplitude oscillatory shear flow are respectively given. In Section 4, we investigate the dependence of the DPD transport properties on the length scale and time scale on which the physical phenomena occur. In Section 5, we discuss how to impose the particle diffusion time and the viscosity in the hydrodynamic limit on the DPD system, and quantify the linear viscoelastic effect from the standard parameter choice. Numerical experiments are presented in Section 6. Section 7 provides some concluding remarks.

2 Transverse current autocorrelation functions (TCAFs)

The current density is given by

$$\mathbf{j}(\mathbf{r}, t) = \sum_{j=1}^N \mathbf{v}_j \delta(\mathbf{r} - \mathbf{r}_j(t)), \quad (4.4)$$

where N is the number of particles and subscripts j denote particle number. Since there is no overall motion, $\langle \mathbf{j}(\mathbf{r}, t) \rangle = 0$ ($\langle \cdot \rangle$ denoted the average operation). Note that $\mathbf{j}(\mathbf{r}, t)$ is the macroscopic (hydrodynamic) variable and \mathbf{v} the

microscopic variable. The Fourier transformation of (4.4) is

$$\mathbf{J}(\mathbf{k}, t) = \int d\mathbf{r} \exp(i\mathbf{k} \cdot \mathbf{r}) \mathbf{j}(\mathbf{r}, t) = \sum_j \mathbf{v}_j(t) \exp(i\mathbf{k} \cdot \mathbf{r}_j(t)). \quad (4.5)$$

The spatial correlation function is defined as [Boon and Yip (1991), Hansen and McDonald (2006)]

$$C_{\alpha\beta}(\mathbf{k}, t) = \frac{k^2}{N} \langle J_\alpha(-\mathbf{k}, 0) J_\beta(\mathbf{k}, t) \rangle, \quad (4.6)$$

where α and β denote Cartesian indices.

For an isotropic fluid, the correlation function (4.6) depends only on the magnitude of \mathbf{k} and one can decompose it into the longitudinal (\parallel) and transverse (\perp) components relative to \mathbf{k} as

$$C_{\alpha\beta}(k, t) = \frac{k_\alpha k_\beta}{k^2} C_{\parallel}(k, t) + \left(\delta_{\alpha\beta} - \frac{k_\alpha k_\beta}{k^2} \right) C_{\perp}(k, t), \quad (4.7)$$

where $\delta_{\alpha\beta}$ is the Kronecker delta, and

$$C_{\perp}(k, t) = \frac{k^2}{N} \langle J_{\perp}(-\mathbf{k}, 0) J_{\perp}(\mathbf{k}, t) \rangle, \quad (4.8)$$

$$C_{\parallel}(k, t) = \frac{k^2}{N} \langle J_{\parallel}(-\mathbf{k}, 0) J_{\parallel}(\mathbf{k}, t) \rangle. \quad (4.9)$$

In the case of Newtonian fluids, one has the following relation

$$\frac{C_{\perp}(k, t)}{C_{\perp}(k, 0)} = \exp \left[-\frac{\eta_k k^2 t}{\rho} \right], \quad (4.10)$$

from which the viscosity in the Fourier-transformed space can be estimated from equilibrium correlation function data.

3 Analytic solutions for simple shear flows of linear viscoelastic fluids

Here we recall some terminologies by considering a small amplitude oscillatory shear flow of a viscoelastic fluid. The flow is generated between two parallel plates separated by a distance h . The bottom plate is fixed while the top plate is sinusoidally displaced by $\delta \sin(\omega t)$ with $\delta \ll h$ being the small amplitude displacement in the x direction. The top plate velocity is

$$U(t) = \delta \omega \cos \omega t. \quad (4.11)$$

The shear rate and the shear strain experienced by the fluid are, respectively,

$$\dot{\gamma}(t) = \frac{\delta}{h} \omega \cos \omega t = \dot{\gamma}_0 \cos \omega t, \quad (4.12)$$

$$\gamma(t) = \frac{\delta}{h} \sin \omega t = \gamma_0 \sin \omega t, \quad \gamma_0 = \frac{\delta}{h} \ll 1, \quad \dot{\gamma}_0 = \omega \gamma_0. \quad (4.13)$$

For a linear viscoelastic fluid at any arbitrary amplitude δ , or for any viscoelastic fluid at a small enough amplitude δ , the only non-zero component of the stress is the shear stress

$$\begin{aligned} \tau_{xy} &= \int_{-\infty}^t G(t-t') \frac{\partial u_x(y, t')}{\partial y} dt' = \int_{-\infty}^t G(t-t') \dot{\gamma}_0 \cos \omega t' dt', \\ &= \int_0^{\infty} \dot{\gamma}_0 G(s) \cos \omega(t-s) ds, \\ &= \int_0^{\infty} \dot{\gamma}_0 G(s) [\cos \omega t \cos \omega s + \sin \omega t \sin \omega s] ds, \\ &= G'(\omega) \gamma_0 \sin \omega t + \eta'(\omega) \dot{\gamma}_0 \cos \omega t, \\ &= G'(\omega) \gamma + \eta'(\omega) \dot{\gamma} = \text{elastic part} + \text{viscous part}, \end{aligned} \quad (4.14)$$

where $G'(\omega)$ is the storage modulus and $\eta'(\omega)$ is dynamic viscosity; they are related to the relaxation modulus $G(t)$ by

$$G'(\omega) = \int_0^\infty \omega G(s) \sin(\omega s) ds, \quad (4.15)$$

$$\eta'(\omega) = \int_0^\infty G(s) \cos(\omega s) ds. \quad (4.16)$$

By rewriting (4.14) as

$$\tau_{xy} = G'(\omega)\gamma_0 \sin \omega t + \eta'(\omega)\dot{\gamma}_0 \sin\left(\frac{\pi}{2} + \omega t\right), \quad (4.17)$$

the shear stress is shown to have the same phase as the applied strain for the elastic part, but $\pi/2$) out of phase from the applied strain for the viscous part. All of the foregoing are familiar results in continuum mechanics (e.g. [Phan-Thien and Mai-Duy (2017)]).

4 Generalised DPD transport coefficients

The conservation laws for the mass density $\rho(\mathbf{r}, t)$ and momentum density $m\mathbf{u}(\mathbf{r}, t)$ in the continuum description read

$$\frac{\partial \rho(\mathbf{r}, t)}{\partial t} + \nabla \cdot (\rho(\mathbf{r}, t)\mathbf{u}(\mathbf{r}, t)) = 0, \quad (4.18)$$

$$\frac{\partial}{\partial t} \rho(\mathbf{r}, t)\mathbf{u}(\mathbf{r}, t) + \mathbf{u}(\mathbf{r}, t) \cdot \nabla (\rho(\mathbf{r}, t)\mathbf{u}(\mathbf{r}, t)) + \nabla \cdot \mathbf{S}(\mathbf{r}, t) = \mathbf{0}, \quad (4.19)$$

where \mathbf{S} is a stress tensor.

4.1 Newtonian fluids

In this case, the stress tensor is given by

$$S_{\alpha\beta}(\mathbf{r}, t) = \delta_{\alpha\beta}p(\mathbf{r}, t) - \eta \left(\frac{\partial u_{\alpha}(\mathbf{r}, t)}{\partial r_{\beta}} + \frac{\partial u_{\beta}(\mathbf{r}, t)}{\partial r_{\alpha}} \right) - \delta_{\alpha\beta} \nabla \cdot \mathbf{u}(\mathbf{r}, t) \left(\eta_B - \frac{2}{3}\eta \right), \quad (4.20)$$

where p is the local pressure, η the shear viscosity and η_B the bulk viscosity.

Without applied external forces, one has $\langle \mathbf{u}(\mathbf{r}, t) \rangle = 0$. Assume that local deviations of the hydrodynamic variables from their average values are small, the variables in (4.18), (4.19) and (4.20) can be expressed as [Boon and Yip (1991), Hansen and McDonald (2006)]

$$n(\mathbf{r}, t) = n + \delta n(\mathbf{r}, t) \approx n, \quad (4.21)$$

$$\mathbf{u}(\mathbf{r}, t) = \langle \mathbf{u}(\mathbf{r}, t) \rangle + \delta \mathbf{u}(\mathbf{r}, t) = \delta \mathbf{u}(\mathbf{r}, t), \quad (4.22)$$

$$\rho \mathbf{u}(\mathbf{r}, t) = m(n + \delta n(\mathbf{r}, t)) (\langle \mathbf{u}(\mathbf{r}, t) \rangle + \delta \mathbf{u}(\mathbf{r}, t)) \approx mn \delta \mathbf{u}(\mathbf{r}, t) = mn \mathbf{u}(\mathbf{r}, t) = \rho \mathbf{j}(\mathbf{r}, t), \quad (4.23)$$

where high-order terms have been ignored and n is the equilibrium number density of the system. At equilibrium, the variables $\langle \delta n(\mathbf{r}, t) \rangle$ and $\langle \delta \mathbf{u}(\mathbf{r}, t) \rangle$ disappear.

Making use of (4.20) and (4.21)-(4.23), the conservation equations (4.18) and (4.19) reduce to the following linear form of the Navier-Stokes equation

$$\frac{\partial \delta \rho(\mathbf{r}, t)}{\partial t} + \nabla \cdot \rho \mathbf{j}(\mathbf{r}, t) = 0, \quad (4.24)$$

$$\frac{\partial \mathbf{j}(\mathbf{r}, t)}{\partial t} + \frac{1}{\rho} \nabla p(\mathbf{r}, t) - \frac{\eta}{\rho} \nabla^2 \mathbf{j}(\mathbf{r}, t) - \frac{1}{\rho} \left(\eta_B + \frac{1}{3}\eta \right) \nabla \nabla \cdot \mathbf{j}(\mathbf{r}, t) = \mathbf{0}. \quad (4.25)$$

In Fourier space, they become

$$\frac{\partial \delta \rho(\mathbf{k}, t)}{\partial t} + i\mathbf{k} \cdot \rho \mathbf{J}(\mathbf{k}, t) = 0, \quad (4.26)$$

$$\frac{\partial \mathbf{J}(\mathbf{k}, t)}{\partial t} + ic^2 \rho(\mathbf{k}, t) \mathbf{k} + \frac{\eta_k k^2}{\rho} \mathbf{J}(\mathbf{k}, t) + \frac{1}{\rho} \left(\frac{4\eta_k}{3} + \eta_B \right) \mathbf{k} \mathbf{k} \cdot \mathbf{J}(\mathbf{k}, t) = \mathbf{0}, \quad (4.27)$$

where c is the isothermal sound speed, and the viscosity becomes a function of the wave number, denoted by η_k .

For the shear viscosity, one only needs to consider the transverse component of the current density. Equation (4.27) reduces to

$$\frac{\partial J_{\perp}(\mathbf{k}, t)}{\partial t} + \frac{\eta_k k^2}{\rho} J_{\perp}(\mathbf{k}, t) = 0. \quad (4.28)$$

Note that equations (4.24)-(4.27) and (4.28) are valid for slow variations of the hydrodynamic dynamic variables only.

Multiplying both sides of (4.28) with $J_{\perp}(-\mathbf{k}, t)$ and then averaging,

$$\frac{\partial}{\partial t} C_{\perp}(k, t) + \frac{\eta_k k^2}{\rho} C_{\perp}(k, t) = 0, \quad (4.29)$$

whose solution is

$$\frac{C_{\perp}(k, t)}{C_{\perp}(k, 0)} = \exp \left[-\frac{\eta_k k^2 t}{\rho} \right], \quad (4.30)$$

from which the viscosity in the Fourier-transformed space can be estimated from equilibrium correlation function data. With this approximation, the observation time scale is assumed to be large. The stress approximations, which involve an additional characteristic time scale, are discussed in next section.

4.2 Linear viscoelastic fluids

The stress tensor for a linear viscoelastic fluid takes the form

$$S_{\alpha\beta}(\mathbf{r}, t) = \int_{-\infty}^t dt' G(t-t') \left(\frac{\partial u_{\alpha}(\mathbf{r}, t')}{\partial r_{\beta}} + \frac{\partial u_{\beta}(\mathbf{r}, t')}{\partial r_{\alpha}} \right), \quad (4.31)$$

where $G(t)$ is the relaxation modulus, a decreasing function of time. The stress at the current time is thus dependent on both the current and past strain rates. It can be seen that, (i) the contribution of a strain rate at the distant past is weighted by the memory relaxation modulus and is less than that of a more recent strain rate (i.e. the concept of fading memory); and (ii) when the memory function is chosen as a Dirac delta function (i.e. $G(t-t') = \eta\delta(t-t')$), a Newtonian fluid is recovered.

Here, we consider a simple relaxation modulus (the Maxwell relaxation modulus)

$$G(t-t') = \frac{\eta}{\tau} \exp\left(-\frac{t-t'}{\tau}\right), \quad (4.32)$$

where τ is a Maxwell relaxation time/decay constant. A fit to the equilibrium normalised $C_{\perp}(k, t)$ data is now described as a function of not only the viscosity η but also the decay constant of the memory function, τ . From continuum mechanics, a plane wave given by $\mathbf{u} = (u_0 \cos ky, 0, 0)$ will decay according to

$$\frac{\partial u_x(y, t)}{\partial t} = \frac{\eta}{\tau\rho} \int_0^t dt' \exp\left(-\frac{t-t'}{\tau}\right) \frac{\partial^2 u_x(y, t')}{\partial y^2}, \quad (4.33)$$

which can be derived from the NS equations. An exact solution to (4.33) is

$$u_x(y, t) = u_0 \exp\left(-\frac{t}{2\tau}\right) \left(\cosh \frac{\Omega t}{2\tau} + \frac{1}{\Omega} \sinh \frac{\Omega t}{2\tau} \right) \cos ky, \quad (4.34)$$

where

$$\Omega = \sqrt{1 - 4 \frac{\tau \eta k^2}{\rho}}. \quad (4.35)$$

On the other hand, from a DPD point of view and without an initial plane wave applied, thermal fluctuations still occur in a system at a given temperature. Since the response of the system to internal fluctuations is the same as to external perturbations, one can link the TCAF to (4.34), resulting in [Hess (2002)]

$$\frac{C_{\perp}(k, t)}{C_{\perp}(k, 0)} = \exp\left(-\frac{t}{2\tau_k}\right) \left(\cosh \frac{\Omega_k t}{2\tau_k} + \frac{1}{\Omega_k} \sinh \frac{\Omega_k t}{2\tau_k} \right), \quad (4.36)$$

where $\tau_k = \tau(k)$ and Ω_k is defined as in (4.35) with $\tau = \tau_k$ and $\eta = \eta_k$. This model involves two fitting parameters, namely the decay time τ_k and the dynamical viscosity η_k . Alternatively, as discussed in [Vogelsang and Hoheisel (1987)], the two fitting parameters can be chosen as the decay times of the memory function (τ_k) and TCAF (τ_k^*), and the fitting model is also shown to be in the form of (4.36) with Ω_k being defined as $\Omega_k^2 = (1/2\tau_k)^2 - (1/\tau_k\tau_k^*)^2$ and the relation between the viscosity and the decay time of TCAF as $\eta_k = \rho/k^2\tau_k^*$.

For each value of k , we fit the model (4.36) to the equilibrium correlation function data. To examine the dependence of the DPD transport properties on the frequency ω , we now utilise analytical expressions of the shear stress in a simple oscillatory flow with a small applied strain. Using (4.15) and (4.16), the coefficients in the strain, $G'(\omega)$, the storage modulus, and in the strain rate, $\eta'(\omega)$, the dynamic viscosity are computed as

$$G'(\omega) = \int_0^{\infty} \omega G(s) \sin(\omega s) ds = \int_0^{\infty} \omega \frac{\eta_k}{\tau_k} \exp\left(-\frac{s}{\tau_k}\right) \sin(\omega s) ds = \frac{\eta_k \omega^2 \tau_k}{\omega^2 \tau_k^2 + 1}, \quad (4.37)$$

$$\eta'(\omega) = \int_0^{\infty} G(s) \cos(\omega s) ds = \int_0^{\infty} \frac{\eta_k}{\tau_k} \exp\left(-\frac{s}{\tau_k}\right) \cos(\omega s) ds = \frac{\eta_k}{\tau_k^2 \omega^2 + 1}, \quad (4.38)$$

where $s = t - t'$. With the storage modulus and shear viscosity being functions of the frequency, one now has an effective mechanism for investigating the response of the DPD system: purely viscous ($\omega \rightarrow 0$), purely elastic ($\omega \rightarrow \infty$) and viscoelastic (intermediate values of ω).

It can be seen from (4.37) and (4.38) that

$$G'(\omega) \rightarrow 0 \text{ and } \eta'(\omega) \rightarrow \eta_k \text{ as } \omega \rightarrow 0, \quad (4.39)$$

$$G'(\omega) \rightarrow \frac{\eta_k}{\tau_k} \text{ and } \eta'(\omega) \rightarrow 0 \text{ as } \omega \rightarrow \infty. \quad (4.40)$$

5 Imposition of fluid properties

One main drawback of the classical DPD formulation is that there is no direct link between the DPD input parameters and the macroscopic properties of the fluid. Here, we show that it is possible to directly impose the particle diffusion time and the viscosity of the fluid in the hydrodynamic limit on the DPD system with the dissipative weighting function of a generalised form, i.e. $w_D = (1 - r/r_c)^s$. The viscosity of the fluid, η , can be specified as an input parameter by enforcing the following constraint [Mai-Duy et al. (2017b), Mai-Duy et al. (2017a)]

$$\eta = \frac{\gamma n^2 [R^2 w_D]_R}{30} = \frac{\gamma n^2}{30} \frac{96\pi r_c^5}{(s+1)(s+2)(s+3)(s+4)(s+5)}, \quad (4.41)$$

where right hand is the dissipative part of the total viscosity by the kinetic theory [Marsh (1998)]. This equation can be solved for the DPD parameter γ ,

$$\gamma = \frac{5\eta(s+1)(s+2)(s+3)(s+4)(s+5)}{16\pi n^2 r_c^5}, \quad (4.42)$$

which is equation (4.39) in [Mai-Duy et al. (2017a)].

The particle diffusion time can be defined as the time taken by the particle to diffuse a distance equal to its radius (the time to restore the equilibrium

configuration)

$$\tau_P = \frac{R^2}{D}, \quad (4.43)$$

where R is the radius and D the self-diffusion coefficient of a particle.

Consider a tagged particle in a sea of other particles. Its radius can be estimated by the Stokes-Einstein relation

$$R = \frac{k_B T}{6\pi D \eta}. \quad (4.44)$$

Substitution of (4.44) into (4.43) yields

$$\tau_P = \frac{(k_B T)^2}{36\pi^2 D^3 \eta^2}. \quad (4.45)$$

By means of kinetic theory, an analytic expression for the diffusivity can be derived as

$$D = \frac{3mk_B T}{\gamma mn [w_D]_R} = \frac{3mk_B T (s+1)(s+2)(s+3)}{\gamma mn 8\pi r_c^3}, \quad (4.46)$$

(i.e. equation (36) in [9]) and expression (4.45) becomes

$$\tau_P = \frac{(k_B T)^2}{36\pi^2 \eta^2} \left(\frac{8\pi r_c^3 \gamma n}{3k_B T (s+1)(s+2)(s+3)} \right)^3. \quad (4.47)$$

Substitution of (4.42) into (4.47) yields the following quadratic equation

$$s^2 + 9s + 20 - E = 0, \quad E = \frac{6k_B T n r_c^2}{5\eta} \sqrt[3]{\frac{36\pi^2 \eta^2 \tau_P}{k_B T^2}}, \quad (4.48)$$

which always has two real solutions and we are interested in the positive one

$$s = \frac{-9 + \sqrt{1 + 4E}}{2}, \quad E > 20. \quad (4.49)$$

The requirement $E > 20$ leads to

$$\tau_P > \frac{31250}{243\pi^2} \frac{\eta}{k_B T n^3 r_c^6} \text{ for a given } \eta, \quad (4.50)$$

$$\eta < \frac{243\pi^2}{31250} k_B T n^3 r_c^6 \tau_P \text{ for a given } \tau_P. \quad (4.51)$$

For given values of τ_P and η , satisfying the conditions (4.50) and (4.51), values of s and γ can then be computed from (4.49) and (4.42), respectively. According to the kinetic theory, the two physical parameters τ_P and η will take the specified values for the values of r_c , $k_B T$, n and m employed.

The DPD without energy conservation describes an isothermal fluid that can be characterised through the mass density $\rho = mn$, viscosity η and Schmidt number $S_c = \eta/\rho D$. It is convenient to rewrite the particle diffusion time (4.45) in the form

$$\tau_P = \frac{1}{36\pi^2} \frac{\rho^3 S_c^3 (k_B T)^2}{\eta^5}. \quad (4.52)$$

In investigating the effects of τ_P , we keep values of ρ , η and S_c constant. In DPD, $k_B T$ is simply a specific kinetic energy; by changing $k_B T$, one can vary the input τ_P . Here, we are interested the relation between the particle diffusion time and the relaxation time of the memory kernel (4.32) - it will be studied numerically in next section.

6 Numerical results

From the DPD equilibrium state space (time-varying positions and velocities of particles), the viscosity can be extracted for different wave numbers. For each wave number, several sets of values of $C_\perp(k, t)/C_\perp(k, 0)$ can be calculated from the DPD simulation data; these can be employed for fitting and back tracking the physical parameters. We use the fitting model (4.30) and (4.36) for Newtonian

and viscoelastic fluids, respectively.

Consider a DPD system defined on a domain of $15 \times 15 \times 15$ with periodic boundary conditions, and ($a_{ij} = 3.5328$, $n = 4$, $r_c = 1.5$, $k_B T = 1$, $m = 1$, $\Delta t = 0.001$). Its physical input parameters (fluid properties) chosen to be imposed are $\eta = 30$ and $S_c = 500$, which correspond to the original input parameters: $\gamma = 6.97$ and $s = 0.42$ [Mai-Duy et al. (2017a)]. It can be seen that the value of s used here is close to 0.5 (the modified DPD fluid), and the corresponding dynamical correlation length ($l_0 = 0.0149$) is less than $r_c = 1.5$. We apply the modified velocity-Verlet algorithm [Groot and Warren (1997)] to solve the DPD equations of motion. Here, the wave number is chosen in the range of 0.4189 to 7.1209 (i.e. 17 values) and their associated results are obtained from a single run. A run of 5×10^5 , 1.5×10^6 , 2×10^6 time steps produces, respectively, 15, 46 and 62 data sets. For each data set, TCAFs are obtained by averaging 500 overlapping samples in which measurements are made every 5 time steps and there are 1025 measurements per sample. It is observed that using a larger number of data sets make the solution behaviour with respect to the wave number more stable. In the following sections, the obtained results from 62 data sets are presented. Both Newtonian and viscoelastic fitting models are applied to the same TCAF data (i.e. $C_{\perp}(k, t)/C_{\perp}(k, 0)$). Their resultant curve fits are observed to be graphically the same; only those for the Newtonian case are displayed. For a time step, the elapsed CPU time of computing TCAF is insignificant compared to that of solving the DPD equations of motion.

6.1 Newtonian fluids

Some typical variations of TCAF are displayed in Figures 4.1. Since the finite size, defined through wavelength, is taken into account, the Newtonian viscosity estimated from TCAF is a function of the wave number. The obtained results

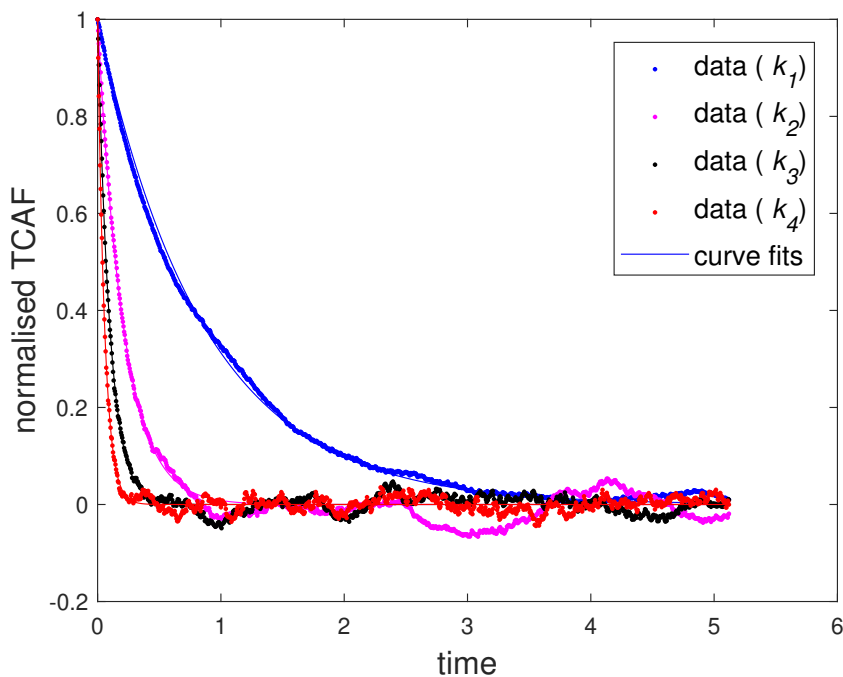


Figure 4.1: Newtonian fluids: Calculated values of TCAF and their curve fits (solid lines) by using (4.30) for the four smallest k values.

are shown in Figures 4.2 and 4.3. One has a wave number-dependent viscosity with the observation time scale being assumed to be large. To obtain the viscosity at $k = 0$ (a continuum), some extrapolation is needed. As discussed in [Palmer (1994)], η_k must be an even function of k and thus may be approximated as

$$\eta_k = \eta_0 + ak^2, \quad (4.53)$$

where η_0 and a are two fitting parameters. Assuming that values of k used for the fitting are sufficiently small, η_0 can be regarded as the viscosity at the hydrodynamic limit. Using the first 4 smallest values of k (i.e. 0.4189, 0.8378, 1.2566 and 1.6755), this leads to $\eta_0 = 29.0214$. On the other hand, from the kinetic theory [Marsh (1998)], the viscosity is estimated as $\eta = 30$. The advantage of the TCAF approach is that it can provide information about the size effect on the transport properties. In addition, one can estimate the transport coefficients

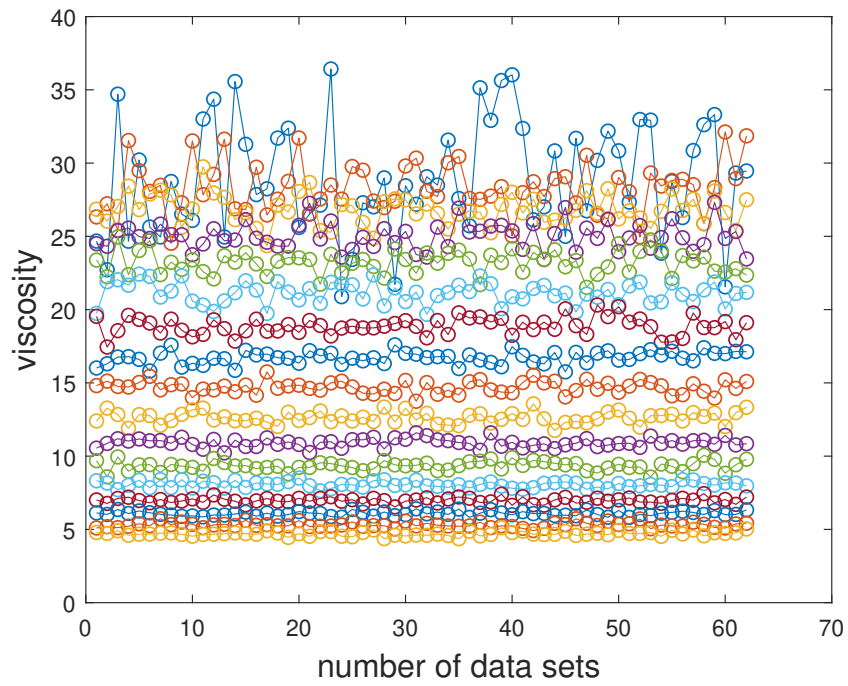


Figure 4.2: Newtonian fluids: Several data sets are used for obtaining the viscosity. Its deviation is generally reduced with increasing k value (i.e. top to bottom).

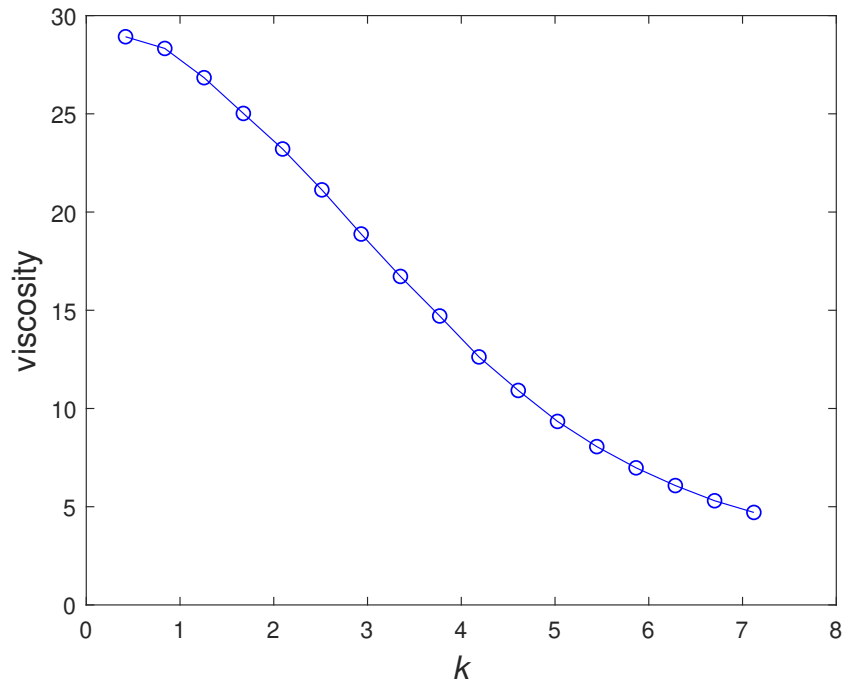


Figure 4.3: Newtonian fluids: Viscosity as a function of the wave number.

at the hydrodynamic limit through extrapolation.

6.2 Linear viscoelastic fluids

6.2.1 Wavelength- and frequency-dependent transport coefficients

The stress approximations involve two parameters, the viscosity and relaxation time, which are wavelength- and frequency-dependent. Figure 4.4 shows plots of the viscosity and the decay constant of the memory function against the wave number k . When k decreases, the decay constant τ_k is seen to increase quickly and is expected to reach its maximum in the hydrodynamic limit. For the shear viscosity η_k , the change is observed to be slow as $k \rightarrow 0$. The obtained values of η_k here are similar to those in the Newtonian case. Figure 4.5 displays the storage modulus and viscosity against the frequency ω , according to (4.37) and (4.38), for the first (smallest) value of k (i.e. $k = k_1 = 0.4189$). At small values of the frequency (i.e. large observation time scale), the system responds like a fluid and at large values of the frequency, one has a solid-like response. The storage modulus provides a convenient means of quantifying the level of elasticity of the fluid.

Figure 4.6 displays the shear viscosity against the frequency ω for the first four values of k (i.e. 0.4189, 0.8378, 1.2566 and 1.6755). It can be seen that $\eta' \rightarrow \eta_k$ as $\omega \rightarrow 0$ and $\eta' \rightarrow 0$ as $\omega \rightarrow \infty$.

Figure 4.7 displays the storage modulus against the frequency ω for the first four values of k (i.e. 0.4189, 0.8378, 1.2566 and 1.6755). It can be seen that $G' \rightarrow 0$ as $\omega \rightarrow 0$ and $G' \rightarrow \eta_k/\tau_k$ (i.e. 1.4175×10^3 , 1.5283×10^4 , 5.0473×10^4 , 6.6011×10^4) as $\omega \rightarrow \infty$.

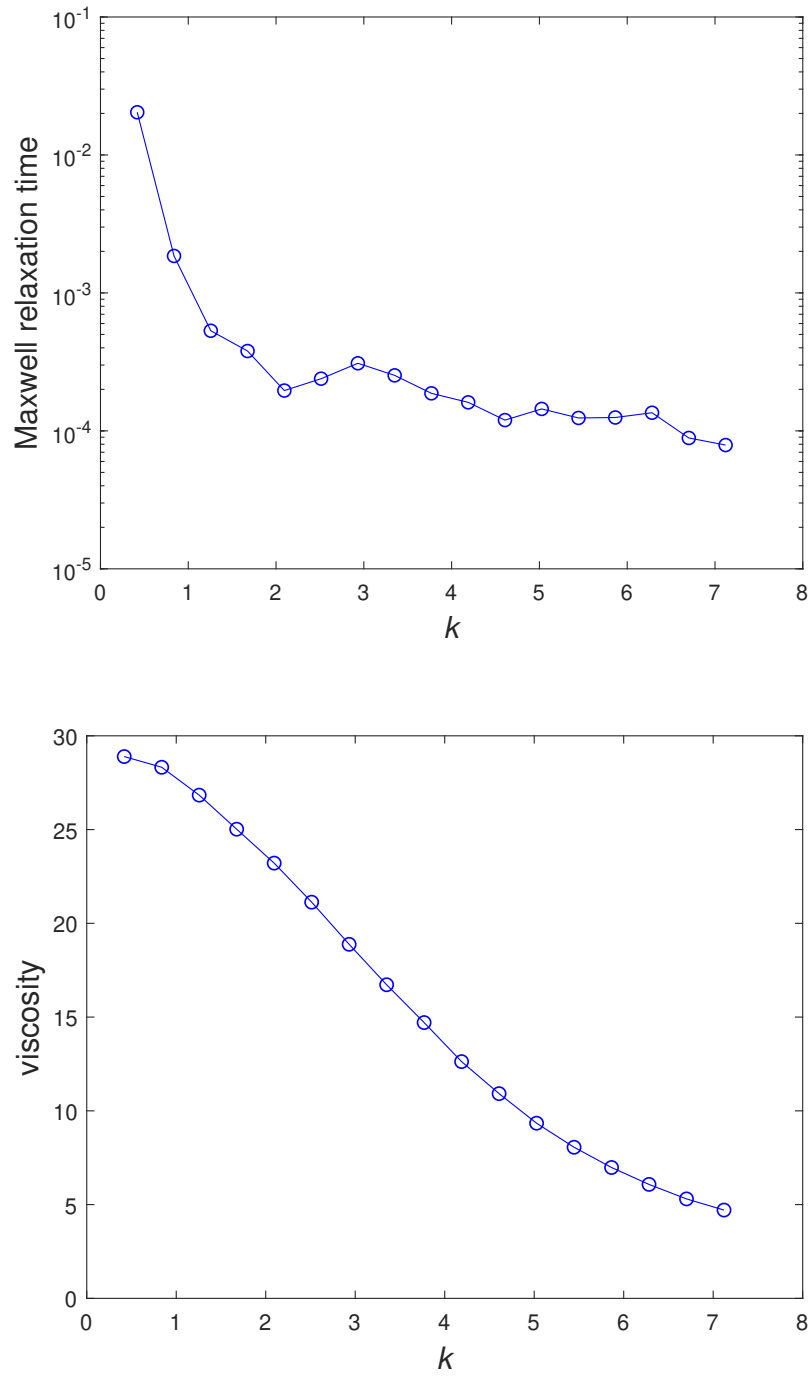


Figure 4.4: Viscoelastic fluids: The decay constant of the relaxation modulus and the viscosity as functions of the wave number. When k decreases, the decay constant has the tendency to increase quickly and is expected to reach its maximum in the hydrodynamic limit. For the shear viscosity η_k , the change is seen to be slow as $k \rightarrow 0$.

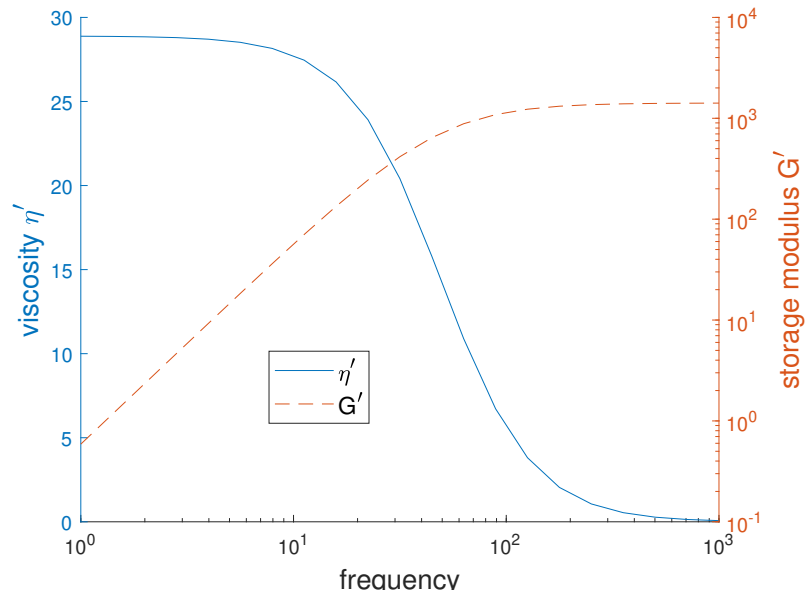


Figure 4.5: Viscoelastic fluids: Storage modulus and viscosity as functions of the frequency for the smallest wave number (i.e. $k = k_1 = 0.4189$). The system responds like a fluid at small values of the frequency (i.e. large observation time scale) and like a solid at large values of the frequency. The storage modulus provides a convenient means of quantifying the level of elasticity of the fluid.

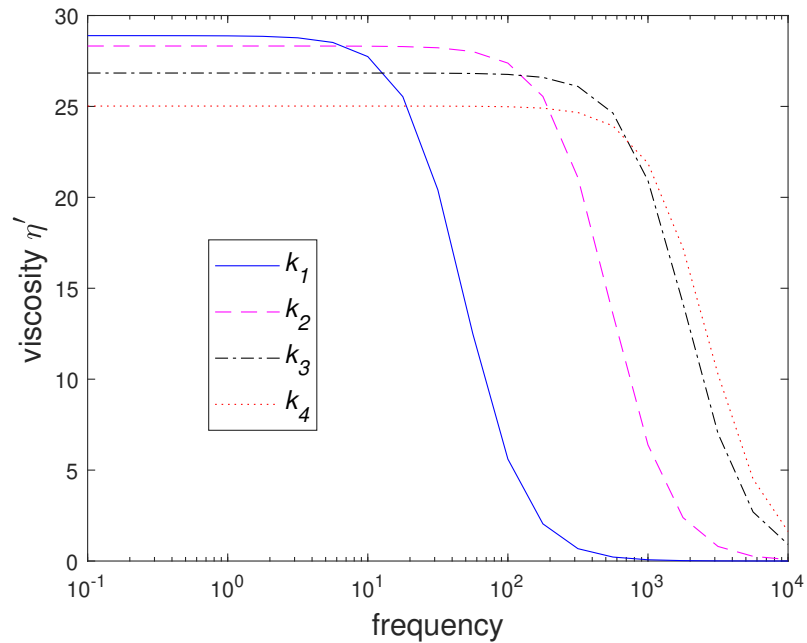


Figure 4.6: Viscoelastic fluids: Viscosity as a function of the frequency for the first four values of k (i.e. 0.4189, 0.8378, 1.2566 and 1.6755). It can be seen that $\eta' \rightarrow \eta_k$ (i.e. 28.8930, 28.3227, 26.8364, 25.0198) as $\omega \rightarrow 0$ and $\eta' \rightarrow 0$ as $\omega \rightarrow \infty$.

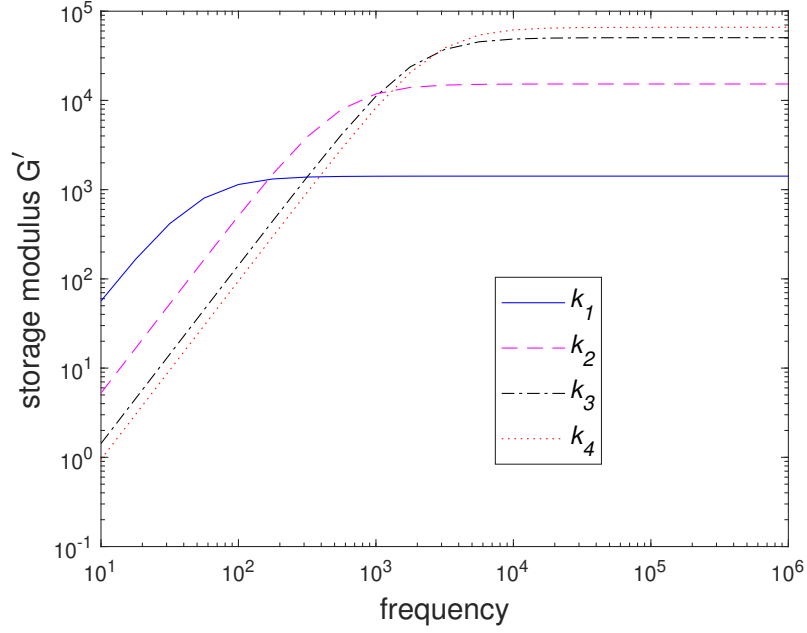


Figure 4.7: Viscoelastic fluids: Storage modulus as a function of the frequency for the first four values of k (i.e. 0.4189, 0.8378, 1.2566 and 1.6755). It can be seen that $G' \rightarrow 0$ as $\omega \rightarrow 0$ and $G' \rightarrow \eta_k/\tau_k$ (i.e. $1.4175 \times 10^3, 1.5283 \times 10^4, 5.0473 \times 10^4, 6.6011 \times 10^4$) as $\omega \rightarrow \infty$. In computing these limit values, the corresponding Maxwell relaxation times are $\tau_k = (2.0383 \times 10^{-2}, 1.8532 \times 10^{-3}, 5.3170 \times 10^{-4}, 3.7902 \times 10^{-4})$.

6.2.2 Linear viscoelastic effect

As shown above, a DPD model using a single set of particles can result in a linear viscoelastic fluid for $k \geq 0$. A concern here is how to quantify the linear viscoelastic effect. Some typical scenarios are studied below and some comments are given at the end of this section. Table 4.1 displays values of the original DPD parameters γ and s that correspond to the input viscosities and Schmidt numbers imposed here.

Same fluid at different imposed $k_B T$ Five values of $k_B T$, (1, 1.1, 1.2, 1.3, 1.4), are employed in conjunction with ($\rho = 4$, $S_c = 500$ and $\eta = 30$). They lead to $\tau_P = (0.93, 1.12, 1.33, 1.57, 1.82)$, respectively, according to (4.52). The obtained results concerning the effects of the particle diffusion time τ_P on the relaxation time of the memory kernel, τ_k , over a wide range of k are shown

Table 4.1: Values of the input viscosity and Schmidt number, and the corresponding original DPD parameters for ($m = 1, n = 4, k_B T = 1, r_c = 1.5$).

Physical inputs		Original DPD parameters	
η	S_c	γ	s
30	500	6.9710	0.4244
28	500	11.7110	0.7727
26	500	19.6042	1.1747
24	500	32.9714	1.6441
30	600	15.0263	0.8898
30	700	27.4087	1.3181
30	800	44.9254	1.7169

in Figure 4.8. The figure indicates that as the wave number k is reduced, the relaxation times τ_k corresponding to different values of the particle diffusion time τ_P apparently converge. At finite k , the obtained results indicate that an increase in τ_P results in a decrease in τ_k . It can also be seen that a change in τ_P can affect the estimated viscosity at the hydrodynamic limit.

Fluids of different viscosities Four values of η , (30, 28, 26, 24), are employed in conjunction with ($\rho = 4, S_c = 500$ and $k_B T = 1$). Figure 4.9 presents the effects of the imposed viscosity η on the relaxation time τ_k over a wide range of k . It shows that as the wave number k is reduced, the relaxation times τ_k corresponding to different values of the imposed (limit) viscosity η apparently converge. At finite k , the obtained results indicate that a decrease in η results in a decrease in τ_k .

Fluids of different Schmidt numbers Four values of S_c , (500, 600, 700, 800), are employed in conjunction with ($\rho = 4, \eta = 30$ and $k_B T = 1$). Figure 4.10 shows the effects of the imposed limit Schmidt number S_c on the relaxation time τ_k over a wide range of k . It indicates that as the wave number k is reduced, the relaxation times τ_k corresponding to different values of the imposed (limit)

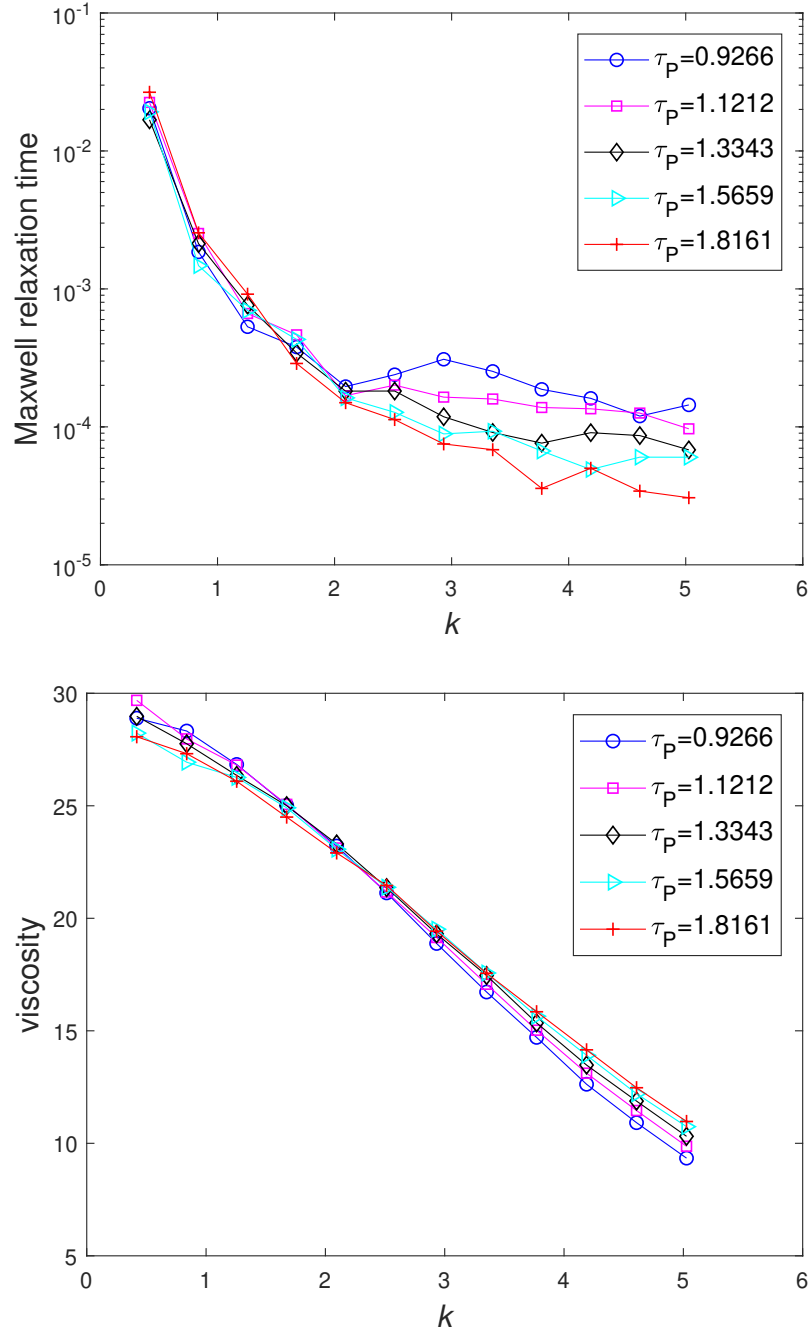


Figure 4.8: Viscoelastic fluids: As the wave number k is reduced, the relaxation times τ_k corresponding to different values of the particle diffusion time τ_P apparently converge. At finite k , the obtained results indicate that an increase in τ_P results in a decrease in τ_k . It can also be seen that a change in τ_P can affect the estimated viscosity at the hydrodynamic limit. All cases take $\rho = 4$, $S_c = 500$ and $\eta = 30$.

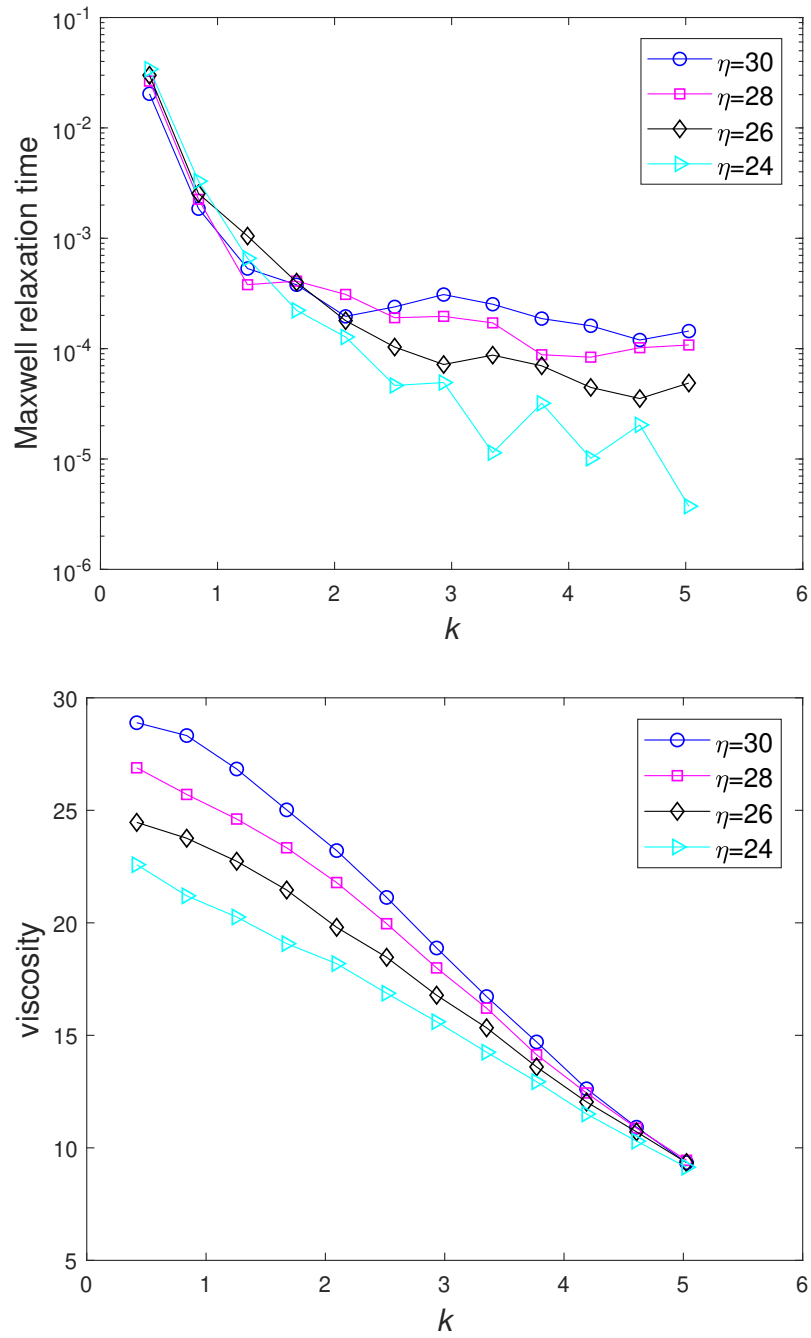


Figure 4.9: Viscoelastic fluids: As the wave number k is reduced, the relaxation times τ_k corresponding to different values of the imposed (limit) viscosity η apparently converge. At finite k , the obtained results indicate that a decrease in η results in a decrease in τ_k . All cases take $\rho = 4$, $S_c = 500$ and $k_B T = 1$.

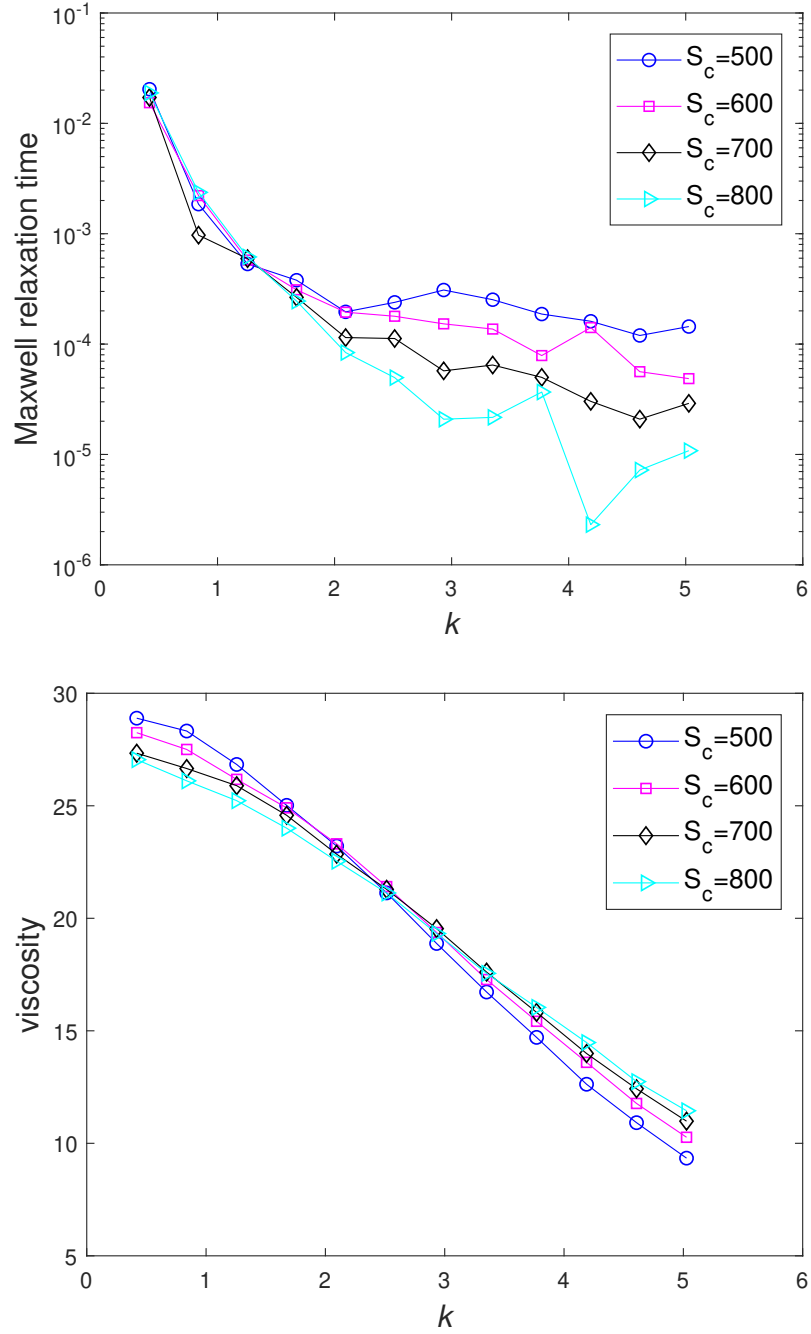


Figure 4.10: Viscoelastic fluids: As the wave number k is reduced, the relaxation times τ_k corresponding to different values of the imposed (limit) Schmidt number S_c apparently converge. At finite k , the obtained results indicate that an increase in S_c results in a decrease in τ_k . It can also be seen that a change in S_c can affect the estimated viscosity at the hydrodynamic limit. All cases take $\rho = 4$, $\eta = 30$ and $k_B T = 1$.

Schmidt number S_c apparently converge. At finite k , the obtained results indicate that an increase in S_c results in a decrease in τ_k . It can also be seen that a change in S_c can affect the estimated viscosity at the hydrodynamic limit.

From the three figures, it can be seen that the relaxation time, corresponding to different values of τ_P , η or S_c , apparently converges as k is reduced, and one would expect that an extrapolation will lead to a similar value for the relaxation time in the limit $k \rightarrow 0$. At finite k , the obtained results suggest that the relaxation time can be strongly affected by the particle diffusion time, viscosity or Schmidt number. An increase in τ_P , a decrease in η or an increase in S_c results in a decrease in τ_k . Differences of τ_k at small k are thus much smaller than those at large k . It can also be seen that a change in S_c or τ_P can affect the estimated viscosity at the hydrodynamic limit.

7 Concluding remarks

In this chapter, DPD in its generalised hydrodynamic regime is considered. For a Newtonian fluid, the stresses are obtained through a large-time averaging process; they involve one fitting parameter, namely the viscosity, which is wavelength-dependent. For a linear viscoelastic fluids, the stresses involve two fitting parameters, namely the viscosity and the relaxation time, which are wavelength- and frequency-dependent. The wavelength dependency of the transport coefficients is obtained numerically while their frequency dependency can be computed analytically, which allow the effects of the length and time scales introduced by physical phenomena to be determined. The DPD input parameters can be determined from the viscosity, mass density, Schmidt number and diffusion time. Numerical experiments indicate that (i) a fluid modelled from a single set of particles may not be Newtonian, but linear viscoelastic, and any time dependent effects must be carefully looked at, and (ii) the relaxation time

measuring the linear viscoelastic effect can be adjusted by means of the input diffusion time, viscosity or Schmidt number at finite wave numbers.

Chapter 5

Application of the proposed DPD to particulate suspensions

In the DPD simulation of particulate suspensions, the viscosity of the solvent phase is typically estimated by a non-equilibrium approach, where the fluid is subjected to a flow process (a shear flow), and the local stress and shear rate tensors are calculated; the obtained values (shear stress/shear rate) are then used in calculating the particulate fluid rheology, for example the ratio of the suspension to the matrix viscosity (reduced/relative viscosity) for a given volume fraction of the suspended phase. However, when suspended particles are added, an additional length scale is introduced into the solvent system and this may affect the solvent macroscopic properties. In this chapter, a particulate suspension is simulated using the spring model, and the solvent viscosity is estimated taking into account the finite-size effect (i.e. in the generalised hydrodynamic regime, as a hydrodynamics of integrable system) to produce improved results. Furthermore, it is observed that the simulation results are also affected by the repulsion strength and an appropriate high value of this coefficient, where the actual solvent viscosity in the hydrodynamic limit is still kept close to the input viscosity, can lead to a further improvement. New results are presented and compared with existing

data.

1 Introduction

Particulate suspensions are widely encountered in natural and industrial processes. They have been intensively investigated, both computationally and experimentally. Particulate suspensions can be characterised by the dependence of their reduced viscosity on the volume fraction and shear rate, their non-zero normal stress differences which are functions of the Peclet number, and their migration of solid particles from high to low shear rate regions [Phan-Thien and Mai-Duy (2017)].

Generalised hydrodynamics is developed for simple fluids, as a formulation of integrable system [Boon and Yip (1991), Hansen and McDonald (2006)]. Their transport coefficients are no longer constant but are functions that can vary in space and time - they are dependent on wavelengths and frequencies of thermal fluctuations occurring at finite temperature. For fluctuations with long wavelengths and low frequencies, the fluid behaves like a continuum (original hydrodynamics). For fluctuations with small wavelengths (molecular scale), the fluid is described by a system of interacting particles (molecular dynamics). From the momenta and coordinates of particles in the system at equilibrium, the dependence of its viscosity on the wavelength can be found, and extrapolation is then carried out to obtain the viscosity in the hydrodynamic limit. With the generalised hydrodynamics theory, finite-size effects are taken into account.

Dissipative Particle Dynamics (DPD) is a popular numerical technique for probing the behaviour of complex-structure fluids [Marsh (1998)]. In DPD, each DPD particle is supposed to represent a group of molecules, and forces acting on a DPD particle include the conservative, dissipative and random forces. The last two forces form a thermostat to keep the mean specific kinetic energy of the system

constant. DPD conserves momentum locally and thus preserves hydrodynamics. In the simulation of suspensions, a solid particle can be modelled by a set of frozen particles [Koelman and Hoogerbrugge (1993)], a single DPD particle [Pan et al. (2010b)] or a few constrained basic DPD particles (spring model) [Phan-Thien et al. (2014a)]. In computing the reduced viscosity, the viscosities of the solvent and the suspension are typically calculated by considering a simple shearing flow of the solvent and the suspension separately, respectively, and the reduced viscosity (suspension viscosity/solvent viscosity) is found. However, for the former, when solid particles are introduced, the solvent viscosity can vary according to the generalised hydrodynamics theory. In this regard (to take into account the size effect due to the presence of solid particles), we attempt to employ DPD in its generalised hydrodynamic regime [Ripoll et al. (2001),Phan-Thien et al. (2018)] to compute the solvent viscosity for a given volume fraction of the suspended phase. A mechanism to approximately estimate the finite size effects (in the context of the spring model) is proposed. Basically, there are two systems of the same base particles, namely a free system and a system with spring constraints as a model for suspension, to be considered. They are all described by the same linear continuum hydrodynamic equations. Due to the spring constraints, the effective length scale of the solvent phase becomes smaller (less than the side of the simulation box), and the viscosity of the constrained system is thus expected to be smaller than that of the free system at a given wavelength/wave number. Based on the difference in the hydrodynamic limit (defined as the limit when the wave number approaches zero), a new length scale of the solvent can be estimated. For the viscosity of the suspension, we are only interested in its values in the hydrodynamic limit, and a non-equilibrium approach (simple shearing) can thus be applied for an efficient estimation.

We also discuss the effect of repulsive forces on the suspension results. In DPD,

a repulsive force is introduced partly to prevent particle overlap, and partly to provide a means to control the compressibility of the model fluid independently of the number density, the cut-off radius and the equilibrium temperature (mean specific kinetic energy). It will be shown that an appropriate high value of the repulsion strength can lead to an improvement in the simulation results compared to the usual case of when water compressibility is enforced.

The remainder of this chapter is organised as follows. Section 2 presents particulate suspensions with the focus on the estimate of the solvent viscosity and the effect of the repulsion strength. Section 3 gives some concluding remarks.

2 Particulate suspensions

The solvent phase is modelled with $\eta = 30$ and $S_c = 500$. Its DPD parameters used are $n = 4$ and

$$\begin{aligned} a_{ij} &= 3.53, & m &= 1, \\ s &= 0.42, & k_B T &= 1, \\ \gamma &= 6.97, & r_c &= 1.5. \end{aligned} \tag{5.1}$$

Here, the units of mass, length and energy are respectively chosen as the mass of a single DPD particle (\overline{m}), the force cut-off radius divided by 1.5 ($\overline{r}_c/1.5$), and the kinetic energy ($\overline{k_B T}$), where the superposed bar is used to denote a dimensional quantity. The repulsion a_{ij} in (5.1) is obtained for a liquid with a water-like compressibility [Groot and Warren (1997)]. Figure 5.1 shows the dependence of the solvent viscosity on the wave number k ($k = 2\pi/\lambda$, λ : the wavelength). Components of \mathbf{k} are chosen as the product of an integer and $2\pi/L$ for periodic boundaries over a cubic region $L \times L \times L$. The present simulation periodic domain is taken as $15 \times 15 \times 15$ (in DPD units).

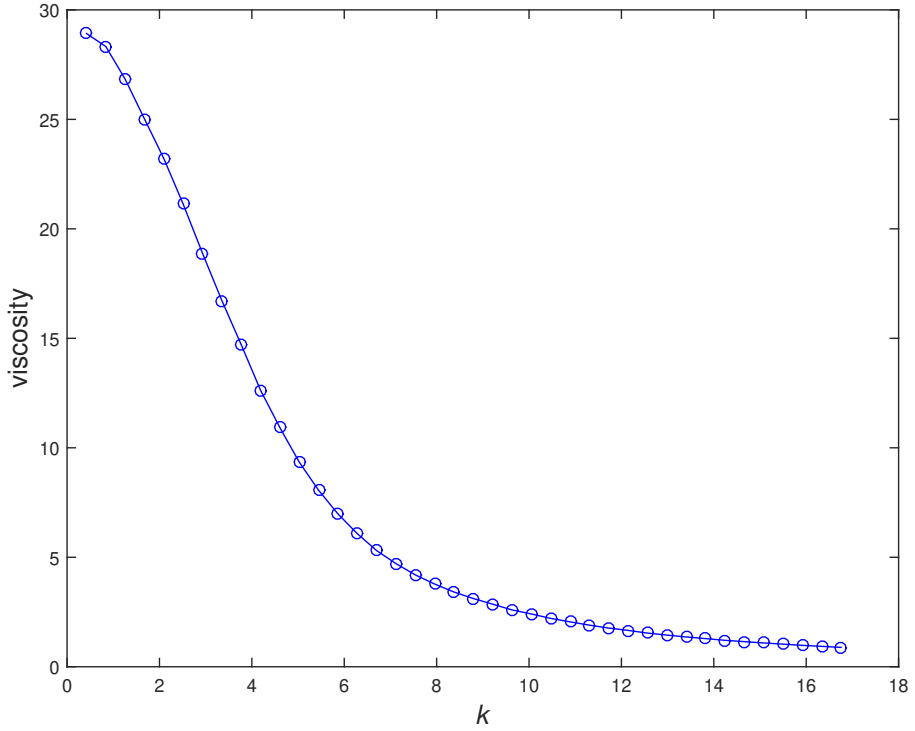


Figure 5.1: Solvent phase ($a_{ij} = 3.53$ (water compressibility), $n = 4$, $m = 1$, $k_B T = 1$, $r_c = 1.5$, $\eta = 30$, $S_c = 500$): the viscosity is a decreasing function of the wave number k (or an increasing function of the wavelength $\lambda = 2\pi/k$).

2.1 Spring model for suspended particles

The multiphase nature of the suspensions may be modelled by using more than one DPD species. In the spring model [Phan-Thien et al. (2014a)], a suspended particle is represented by a set of p basic DPD particles (p is small) that are connected, through stiff springs, to some reference sites collectively moving as a rigid body. For example, a spherical particle can be modelled using 6 or 8 basic DPD particles with their reference sites at the vertices of either an octahedron or a cube, respectively. The shape and size of a suspended particle are actually defined by the repulsive force field generated by the constituent particles of a suspended particle (not by their locations).

The forces on constituent particles of the k th suspended particle are

$$\mathbf{F}_i^k(t) = \sum_{j=1, j \neq i}^N [\mathbf{F}_{ij,C}^k(t) + \mathbf{F}_{ij,D}^k(t) + \mathbf{F}_{ij,R}^k(t)] + \mathbf{F}_{i,S}^k(t), \quad i = (1, 2, \dots, p), \quad (5.2)$$

where $\mathbf{F}_{i,S}^k(t) = -H [\mathbf{r}_i^k(t) - \bar{\mathbf{r}}_i^k(t)]$ is the spring force with H being the stiffness of the spring and $\bar{\mathbf{r}}_i^k(t)$ the position of the reference site.

It should be pointed out that the sum of the spring forces on the constituent particles of the suspended particle has a zero mean. The reference sites are calculated through their Newton-Euler equations, using data from the previous time step, while the velocities of their associated DPD particles are found by solving the DPD equations at the current time step.

2.2 Finding a length scale introduced into the solvent system due to the presence of suspended particles

Three approaches are presented. In the first two, the mean distance between the suspended particles is taken as a new length scale to the solvent system. In the third approach, transverse-current autocorrelation functions (TCAFs) are used to estimate a new length scale.

2.2.1 Approach 1

A length scale that is introduced into the solvent system can be regarded as the mean distance between the suspended particles; a convenient distance is an estimate of a side of the cube of a particle,

$$\lambda = \frac{1}{n_c^{1/3}}, \quad (5.3)$$

where n_c is the number density of the colloidal (particulate) phase.

2.2.2 Approach 2

The mean inter-colloid distance is estimated as the radius of the sphere of the volume per particle (the Wigner-Seitz radius [Girifalco (2000)])

$$\lambda = \left(\frac{3}{4\pi n_c} \right)^{1/3}. \quad (5.4)$$

2.2.3 Approach 3: TCAF

Here, we propose a scheme, based on TCAFs, to estimate a length scale introduced into the solvent system from the spring constraints. For a given volume fraction of the suspended phase, two corresponding systems, containing all the solvent particles and the constituent particles of the suspended phase, are considered. Note that the solvent and the constituent particles are all subjected to the same DPD parameters, i.e. those defined in (5.1). In the first system, all the particles are acted on by DPD forces and are not under any other constraints. In the second system, some of the particles (constituent particles) are constrained by the springs to form suspended particles. The two systems are assumed to represent some simple fluids. Results concerning the dependence of the viscosity on the wave number (wavelength) by the TCAF approach for the two systems are shown Figure 5.2. Extrapolations are then conducted to obtain the viscosities in the hydrodynamic limit ($k \rightarrow 0$). Due to the presence of springs, an effective length scale of the constrained system is less than the side of the simulation box, and its viscosity is seen to be lower. The constrained system in the hydrodynamic limit can thus be considered as the free system at the wave number (wavelength) that corresponds to the hydrodynamic-limit viscosity of the constrained system. This wavelength is taken as a new length scale in the solvent phase.

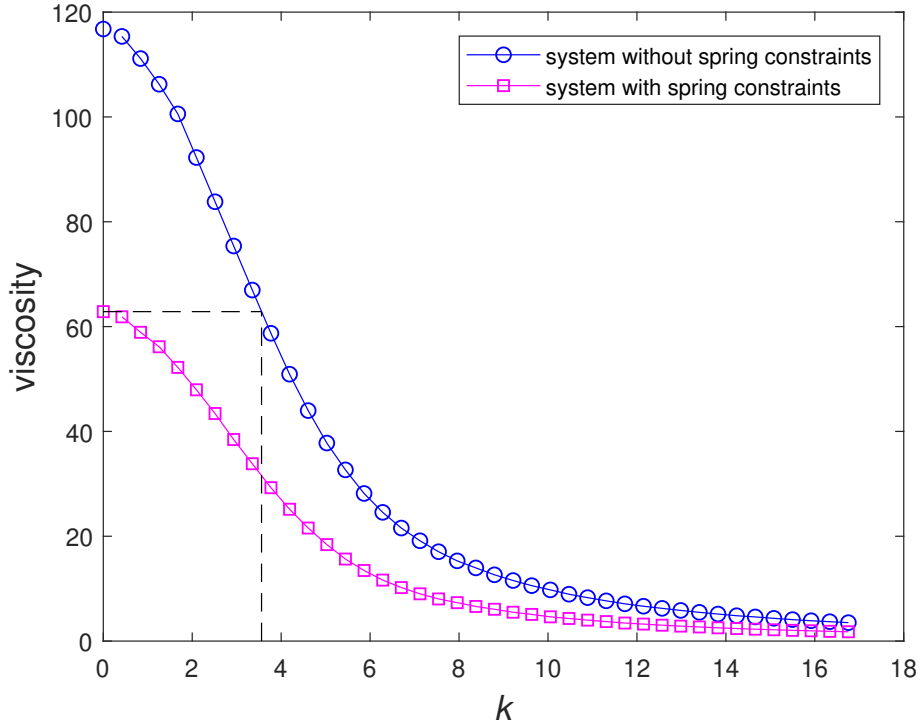


Figure 5.2: Process of finding a new length scale that is introduced into the solvent system due to the presence of suspended particles. For a given volume fraction, two corresponding systems (one without any spring constraints and the other with some spring constraints as a model for suspension) are considered; they have the same total numbers of the base particles and employ the same associated DPD parameters. The two systems are assumed to represent simple fluids; through the TCAF approach, their viscosities are shown to depend on the wave numbers (wavelengths). Extrapolations are then conducted to obtain the viscosities in the hydrodynamic limit ($k \rightarrow 0$). With springs, the effective length scale of the constrained system is less than the system size L , and its viscosity is seen to be lower. The constrained system in the hydrodynamic limit can be considered as the free system at the wave number (wavelength) that corresponds to the hydrodynamic-limit viscosity of the constrained system. This wavelength is taken as a new length scale in the solvent phase.

Table 5.1 displays the effective wavelength of the solvent phase against the volume fraction of the suspended phase by the three approaches, while Table 5.2 details the corresponding effective wave numbers and effective viscosities in the TCAF case. Note that compressibility of the solvent is matched to that of water, i.e. $a_{ij} = 3.53$, and the simulation box is taken as $15 \times 15 \times 15$ (in DPD units).

Table 5.1: Effective wavelength of the solvent phase against volume fraction of the suspended phase by the three approaches. Compressibility of the solvent is matched to that of water, i.e. $a_{ij} = 3.53$, and the simulation box is taken as $15 \times 15 \times 15$ (in DPD units).

ϕ	Effective wavelengths		
	Sphere-based mean distance	Cube-based mean distance	TCAF
0.0119	3.1018	5.0000	12.8671
0.0277	2.3263	3.7500	9.4465
0.0526	1.8611	3.0000	5.3996
0.0876	1.5509	2.5000	4.7463
0.1323	1.3293	2.1429	3.8475
0.1854	1.1632	1.8750	3.2045
0.2447	1.0339	1.6667	2.7583
0.3077	0.9305	1.5000	2.4303
0.3717	0.8459	1.3636	2.1586
0.4344	0.7754	1.2500	1.9544
0.4940	0.7158	1.1538	1.7431

Table 5.2: Effective wave number, wavelength and viscosity of the solvent phase against volume fraction of the suspended phase by the TCAF approach. Compressibility of the solvent is matched to that of water, i.e. $a_{ij} = 3.53$, and the simulation box is taken as $15 \times 15 \times 15$ (in DPD units).

ϕ	Effective k	Effective λ	Effective η
0.0119	0.4883	12.8671	28.9109
0.0277	0.6651	9.4465	28.7144
0.0526	1.1636	5.3996	27.2179
0.0876	1.3238	4.7463	26.5560
0.1323	1.6331	3.8475	25.2043
0.1854	1.9608	3.2045	23.8032
0.2447	2.2779	2.7583	22.3348
0.3077	2.5853	2.4303	20.7466
0.3717	2.9108	2.1586	18.9952
0.4344	3.2149	1.9544	17.4017
0.4940	3.6047	1.7431	15.5091

2.3 Effect of the repulsion coefficient

It will be shown that the input repulsion strength can affect the system viscosity. In the present study, the input viscosity of the solvent phase is specified as 30. Water-compressibility matching leads to $a_{ij} = 3.53$. By simulating Couette flow (a non-equilibrium approach), the solvent viscosity is estimated as 29.08, close to the input value. Increasing a_{ij} , the solvent viscosity is observed to have a larger value, e.g. (29.66, 30.22, 30.66) for $a_{ij} = (6.50, 9.50, 18.50)$, which correspond to a positive change of 1.99%, 3.92% and 5.45%, respectively. Increasing a_{ij} produces a less compressible fluid and is more effective in preventing particle overlap. However, at large values, the conservative force can be dominant and the DPD system has a solid-like behaviour (particles do not move, just oscillate about their positions). Here, we limit our attention to the change within about

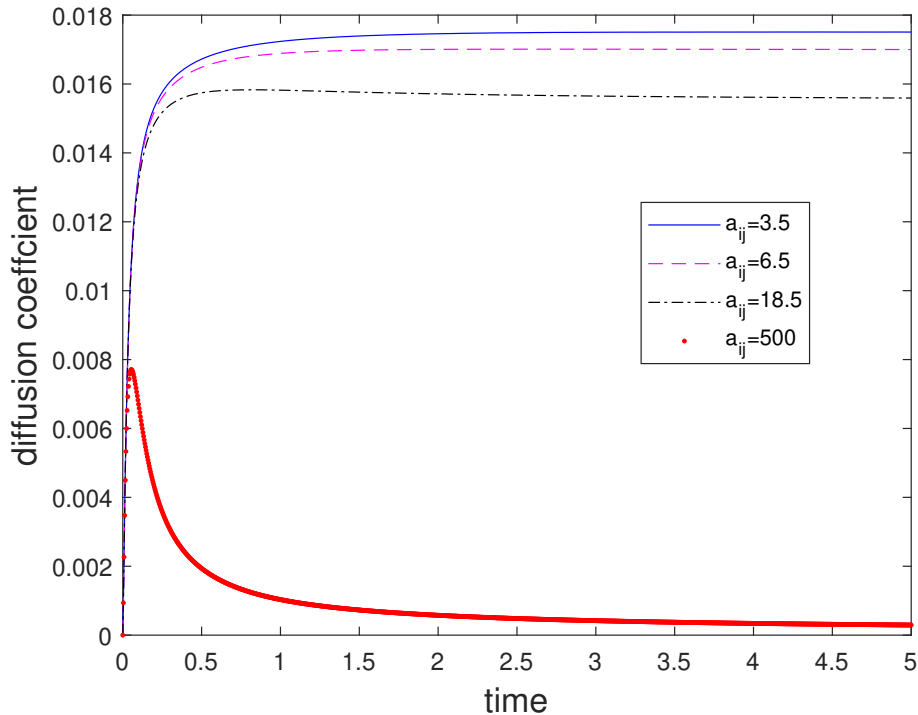


Figure 5.3: Diffusion coefficient against time for several values of the repulsion. For $a_{ij} = (3.53, 6.50)$, the diffusion coefficients are observed to stay constant at large times. For larger a_{ij} , there is some reduction in the coefficient and no significant diffusion at $a_{ij} = 500$.

2 %, where the diffusion coefficient is observed to stay constant at large times as shown in Figure 5.3.

2.4 Numerical results

The suspension viscosity is now calculated by the non-equilibrium approach (simple shearing) at a small shear rate of 0.01, while the solvent viscosity is estimated taking into account the finite-size effect due to the presence of the suspended particles. Two solvent fluids with $a_{ij} = 3.53$ (water compressibility) and $a_{ij} = 6.50$ (a fluid less compressible than water) are considered. The relationship between reduced viscosity of the suspension and volume fraction of the suspended phase can be divided in 3 regimes: dilute ($\phi \lesssim 0.02$, linear dependence), semi-dilute ($\phi \lesssim 0.25$, visible higher-order effects) and concentrated ($\phi \gtrsim 0.25$, rapid growth). The obtained DPD results are shown in Figure 5.4 for $a_{ij} = 3.53$ and in Figure 5.5 for $a_{ij} = 6.50$. Theoretical results in the dilute regime (Einstein, 1906) and empirical results (Quemada, 1977), which have found widespread application, are also included for comparison purposes. It can be seen that (i) the original hydrodynamic DPD produces improved reduced viscosities against volume fraction with increasing a_{ij} (with respect to improved agreement with Einstein's relation at the dilute limit); (ii) the generalised hydrodynamic DPD (TCAF) yields a better behaviour than the original hydrodynamic DPD in all three regimes for both fluids considered (with respect to agreement with Quemada's); (iii) the generalised hydrodynamic DPD based on sphere/cube mean distance overestimates the reduced viscosity in every case studied.

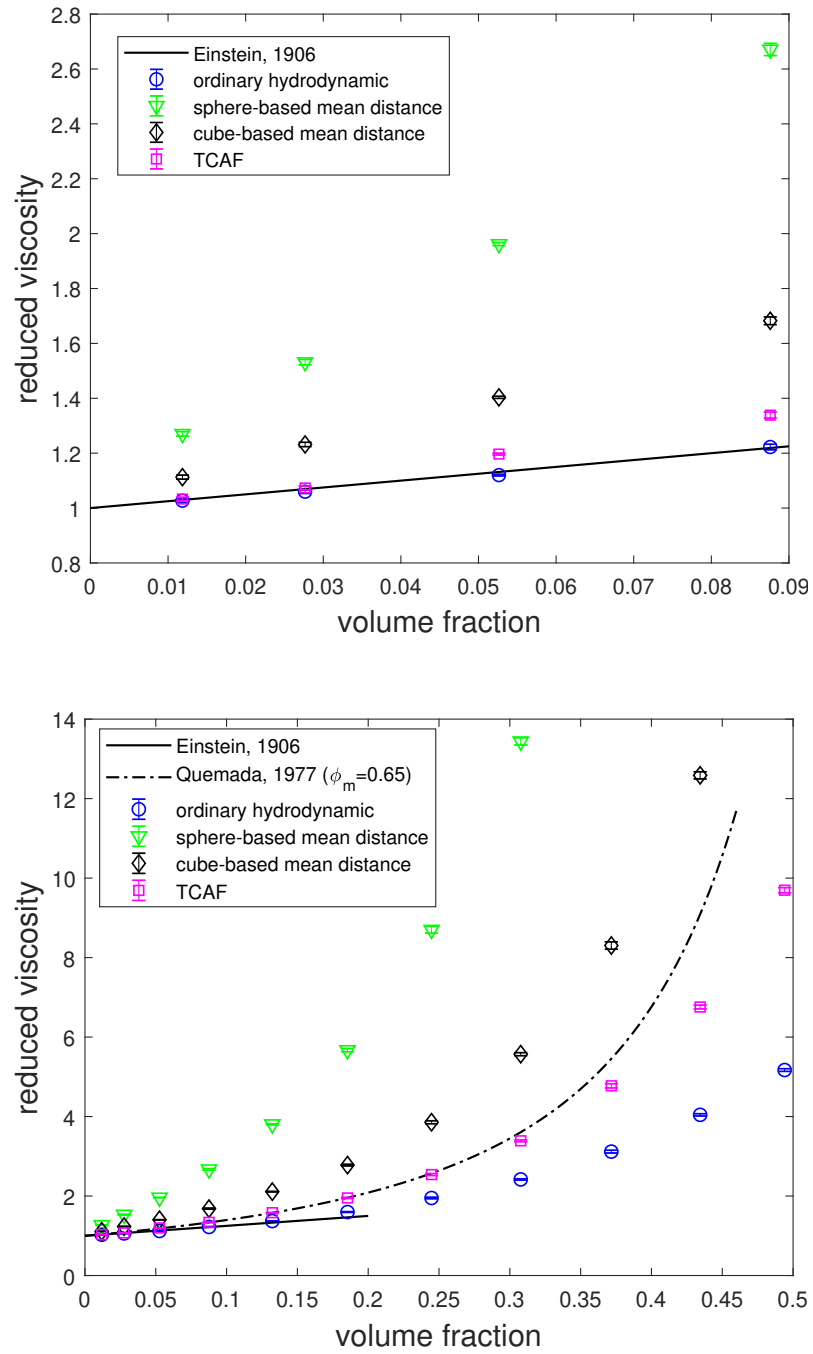


Figure 5.4: Reduced viscosity by original and generalised hydrodynamic DPD using the same repulsion $a_{ij} = 3.53$ (water compressibility). The latter (TCAF) is seen to have a better performance than the former in the dilute ($\phi \lesssim 0.02$, linear dependence), semi-dilute ($\phi \lesssim 0.25$, visible higher-order effects) and concentrated ($\phi \gtrsim 0.25$, rapid growth) regimes. It appears that the generalised hydrodynamic DPD based on sphere/cube mean distance overestimates the reduced viscosity in every regime. Theoretical results in the dilute regime (Einstein, 1906) and empirical results (Quemada, 1977), which have found widespread application, are also included for comparison purposes.

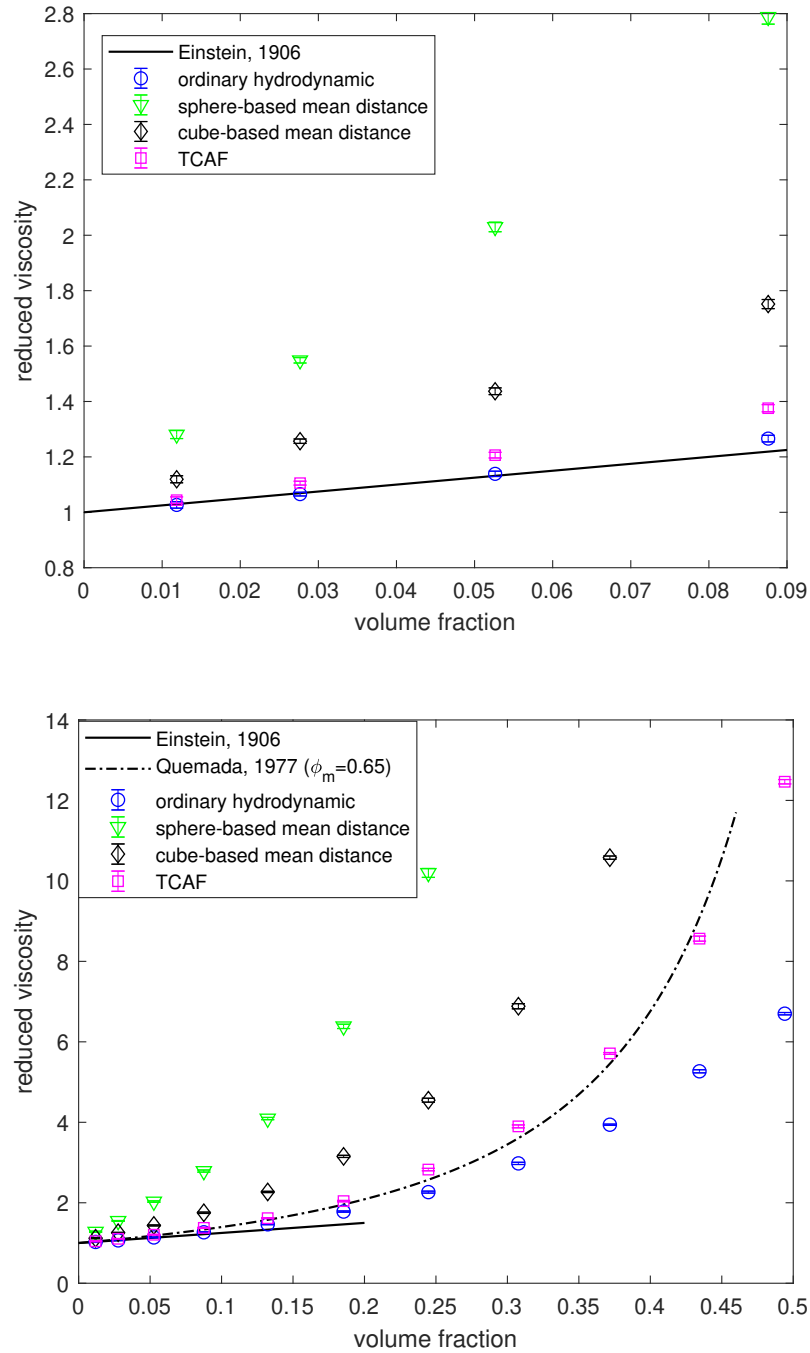


Figure 5.5: Reduced viscosity by original and generalised hydrodynamic DPD using the same repulsion $a_{ij} = 6.50$ (a fluid is less compressible than water). The latter (TCAF) is seen to have a better performance than the former in the dilute ($\phi \lesssim 0.02$, linear dependence), semi-dilute ($\phi \lesssim 0.25$, visible higher-order effects) and concentrated ($\phi \gtrsim 0.25$, rapid growth) regimes. It appears that the generalised hydrodynamic DPD based on sphere/cube mean distance overestimates the reduced viscosity in every regime. Theoretical results in the dilute regime (Einstein, 1906) and empirical results (Quemada, 1977), which have found widespread application, are also included for comparison purposes.

3 Concluding remarks

In this chapter, particulate suspensions are simulated with the dissipative particle dynamics (DPD) method, in which the spring model is used to model suspended particles. In estimating the solvent viscosity, DPD is employed in its generalised hydrodynamic regime to take into account the finite size effect due to the presence of suspended particles. The effective sizes (wavelengths) are predicted by several approaches, and the transverse current autocorrelation functions (TCAFs) approach is shown to yield the most reasonable results. Improved reduced viscosities of the suspension are clearly observed in the dilute ($\phi \lesssim 0.02$, linear dependence), semi-dilute ($\phi \lesssim 0.25$, visible higher-order effects) and concentrated ($\phi \gtrsim 0.25$, rapid growth) regimes, compared to the theoretical dilute limit, and the best know empirical results at non-dilute regime. Further improvement can also be acquired by increasing the repulsion to an appropriate value, where the actual solvent viscosity in the hydrodynamic limit is still kept close to the input viscosity and the diffusion coefficient of the solvent still stays constant at large times.

Chapter 6

Conclusion and future work

Conclusion

In this thesis, a new version of DPD for investigating complex fluids at the mesoscale has been developed successfully. Key developments include

- Providing a mapping between the DPD space (repulsion parameter, noise level, weighted functions) and the physical space (fluid properties). The mapping is based on the utilisation of the virial theorem and the kinetic theory in junction with the employment of new forms of the weighting functions. The inputs to the DPD system are now the viscosity, the Schmidt number, the mass density, the time-scale ratio and the water-like compressibility.
- Expanding the working range of the DPD. This expansion is based on the use of transverse current auto-correlation functions (TCAFs) to express the transport coefficients as functions of wavelengths and frequencies of thermal fluctuations. The proposed DPD method can now be applied to investigate the model fluid in both regimes: the hydrodynamic limit and the generalised hydrodynamics.

- Developing a simple treatment based on the time-scale ratio to reduce the compressibility effects of the DPD fluid in simulating incompressible flows.

The proposed method has been successfully applied to simulate various fluid systems. Typical applications presented include

- Modelling of a single phase system (e.g. flows of a simple fluid between two parallel plates, flows of a simple fluid past through a periodic array of fixed cylinders, and equilibrium systems), where a consistent scaling of thermal fluctuations is demonstrated, similar behaviours of the flow at different coarse-graining levels are observed, a single set of particles is shown to have the ability to model some linear viscoelastic fluids, and a new scheme of promoting incompressibility to the flow is shown to be effective.
- Modelling of multi-phase systems (e.g. the suspension of spherical particles in a fluid), where a consistent scaling of thermal fluctuations is also demonstrated, and similar behaviours of the flow at different coarse-graining levels are observed.
- Modelling of particulate suspensions, where improved results of viscosities are obtained when compared to those by the original spring model.

Limitations of this research and Future work

The proposed DPD scheme is currently verified on benchmark test problems only. Complex/extension flows are still not considered yet, and the effect of Schmidt number on the solution accuracy is still not studied in detail.

In future work, we aim to address these limitations. In addition, the proposed DPD scheme can be further developed to model other forms of particulate sus-

pensions such as monodispersed suspensions of very high concentration, non-Newtonian suspensions and polydispersed suspensions. For high concentration suspensions, the level of hardness of the suspended particles can be improved by increasing the number density of the solvent phase. For non-Newtonian suspensions, the suspending phase can be modelled by two sets or more of DPD particles or by a single set of DPD particles in the generalised hydrodynamics. For polydispersed suspensions, the spring model can be modified to represent suspended particles of different sizes and different shapes.

References

- Alder, B. J. and Wainwright, T. E. (1957). Phase transition for a hard sphere system. *The Journal of chemical physics*, 27(5):1208–1209.
- Alder, B. J. and Wainwright, T. E. (1959). Studies in molecular dynamics. i. general method. *The Journal of Chemical Physics*, 31(2):459–466.
- Alik Ismail-Zadeh, P. T. (2010). *Computational Methods for Geodynamics*. Cambridge University Press, 1 edition.
- Allen, M. P. and Tildesley, D. J. (1987). *Computer simulation of liquids*. Oxford University Press.
- Anand, D. V., Patnaik, B. S. V., and Vedantam, S. (2017). Dissipative particle dynamics study of a flexible filament in confined shear flow. *Soft Matter*.
- Argyris, J. and Scharpf, D. (1969). Some general considerations on the natural mode technique: Part i. small displacements. *The Aeronautical Journal*, 73(699):218–226.
- Argyris, J. H. and Kelsey, S. (1960). *Energy theorems and structural analysis*, volume 60. Springer.
- Arienti, M., Pan, W., Li, X., and Karniadakis, G. (2011). Many-body dissipative particle dynamics simulation of liquid/vapor and liquid/solid interactions. *The Journal of Chemical Physics*, 134:204114.
- Avalos, J. B. and Mackie, A. D. (1997). Dissipative particle dynamics with energy conservation. *EPL (Europhysics Letters)*, 40:141–146.
- Barbu, A. and Zhu, S.-C. (2020). *Monte Carlo Methods*, volume 35. Springer.
- Bedrov, D., Piquemal, J.-P., Borodin, O., MacKerell Jr, A. D., Roux, B., and Schröder, C. (2019). Molecular dynamics simulations of ionic liquids and electrolytes using polarizable force fields. *Chemical reviews*, 119(13):7940–7995.
- Beer, G., Marussig, B., and Duenser, C. (2020). *The Isogeometric Boundary Element Method*. Springer.
- Bian, X., Litvinov, S., Qian, R., Ellero, M., and Adams, N. A. (2012). Multiscale modeling of particle in suspension with smoothed dissipative particle dynamics. *Physics of Fluids*, 24:012002.
- Bidokhti, P. S. (2019). *Theory, Application, and Implementation of Monte Carlo Method in Science and Technology*. BoD–Books on Demand.

- Binder, K., Baumgärtner, A., Burkitt, A., Ceperley, D., De Raedt, H., Ferrenberg, A., Heermann, D., Herrmann, H., Landau, D., Levesque, D., et al. (1995). *The Monte Carlo Method in Condensed Matter Physics*. Topics in Applied Physics 71. Springer-Verlag Berlin Heidelberg, 2 edition.
- Blazek, J. (2015). *Computational Fluid Dynamics: Principles and Applications*. Butterworth-Heinemann, 3 edition.
- Boek, E. S., Coveney, P. V., Lekkerkerker, H. N. N., and van der Schoot, P. (1997). Simulating the rheology of dense colloidal suspensions using dissipative particle dynamics. *Physical Review E*, 55:3124–3133.
- Boon, J. P. and Yip, S. (1991). *Molecular Hydrodynamics*. Dover Publications.
- Boromand, A., Jamali, S., and Maia, J. M. (2017). Structural fingerprints of yielding mechanisms in attractive colloidal gels. *Soft matter*, 13(2):458–473.
- Bossis, G. and Brady, J. F. (1984). Dynamic simulation of sheared suspensions. i. general method. *The Journal of chemical physics*, 80(10):5141–5154.
- Brachet, M. and Croisille, J.-P. (2021). Spherical shallow-water wave simulation by a cubed-sphere finite-difference solver. *Quarterly Journal of the Royal Meteorological Society*.
- Brebbia, C. A. (2010). *Boundary Elements and Other Mesh Reduction Methods XXXII (Wit Transactions on Modelling and Simulation)*. Wit Transactions on Modelling and Simulation 32. WIT Press, 1 edition.
- Brebbia, C. A. (2017). The birth of the boundary element method from conception to application. *Engineering Analysis with Boundary Elements*, 77:iii–x.
- Brebbia, C. A. and Katsikadelis, J. T. (2006). *Boundary Elements And Other Mesh Reduction Methods XXVIII (v. 28)*. WIT Press, illustrated edition edition.
- Brebbia, C. A. and Poljak, D. (2012). *Boundary Elements and Other Mesh Reduction Methods XXXIV*, volume 53. Wit Press.
- Brebbia, C. A., Poljak, D., and Popov, V. (2007). *Boundary Elements and Other Mesh Reduction Methods XXIX (Wit Transactions on Modelling and Simulation)*. Wit Transactions on Modelling and Simulation. WIT Press, 1 edition.
- Brebbia, C. A. and Popov, V. (2011). *Boundary Elements and Other Mesh Reduction Methods XXXIII (Wit Transactions on Modelling and Simulation)*. Wit Transactions on Modelling and Simulation. WIT Press / Computational Mechanics.
- Brebbia, C. A. and Skerget, L. (2008). *Boundary Elements and Other Mesh Reduction Methods XXX (Wit Transactions on Modelling and Simulation)*. Wit Transactions on Modelling and Simulation. WIT Press.

- Brebbia, C. A., Telles, J. C. F., and (auth.), L. C. W. (1984). *Boundary Element Techniques: Theory and Applications in Engineering*. Springer-Verlag Berlin Heidelberg, 1 edition.
- Brebbia, C. A. and Wrobel, L. C. (1992). *Boundary Element Methods in Heat Transfer*. Springer Netherlands.
- Canuto, C., Hussaini, M. Y., Quarteroni, A., Thomas Jr, A., et al. (1988). *Spectral methods in fluid dynamics*. Springer Science & Business Media.
- Catala, A. (2019). *Liposomes - Advances and Perspectives — Dissipative Particle Dynamics Simulations of Self-Assemblies of Liposomes for Drug Delivery Applications*, volume 10.5772/intechopen.77926.
- Chen, S., Phan-Thien, N., Khoo, B. C., and Fan, X.-J. (2006). Flow around spheres by dissipative particle dynamics. *Physics of Fluids*, 18:103605.
- Chen, S. and Yong, X. (2018). Dissipative particle dynamics modeling of hydrogel swelling by osmotic ensemble method. *The Journal of Chemical Physics*, 149(9):094904.
- Cheng, A. H.-D. and Cheng, D. T. (2005). Heritage and early history of the boundary element method. *Engineering Analysis with Boundary Elements*, 29(3):268–302.
- Ciccotti, G., Ferrario, M., Schuette, C., et al. (2014). *Molecular dynamics simulation*, volume 16. MDPI Books Basel, Beijing.
- Courant, R. (1943). Variational methods for the solution of problems of equilibrium and vibrations. *Bulletin of the American Mathematical Society*, 49:1–23.
- Deganutti, G., Moro, S., and Reynolds, C. A. (2020). A supervised molecular dynamics approach to unbiased ligand–protein unbinding. *Journal of chemical information and modeling*, 60(3):1804–1817.
- Deng, M., Li, Z., Borodin, O., and Karniadakis, G. E. (2016). CDPD: A new dissipative particle dynamics method for modeling electrokinetic phenomena at the mesoscale. *Journal of Chemical Physics*, 145:144109.
- Deville, M. O., Fischer, P. F., Fischer, P. F., Mund, E., et al. (2002). *High-order methods for incompressible fluid flow*. Number 9. Cambridge university press.
- Doormaal, M. A. V. and Pharoah, J. G. (2009). Determination of permeability in fibrous porous media using the lattice boltzmann method with application to pem fuel cells. *International Journal for Numerical Methods in Fluids*, 59:75–89.
- Dzwinel, W., Alda, W., Kitowski, J., Moscinski, J., Wcislo, R., and Yuen, D. (1995). Applications of molecular dynamics method for simulation in macroscale. *Molecular Simulation*, 15:343–360.

- Dzwinel, W. and Yuen, D. A. (2000). A two-level, discrete-particle approach for simulating ordered colloidal structures. *Journal of Colloid and Interface Science*, 225:179–190.
- Ellero, M. and Español, P. (2018). Everything you always wanted to know about SDPD* (*but were afraid to ask). *Applied Mathematics and Mechanics*, 39:103–124.
- Ellero, M. and Tanner, R. (2005). Sph simulations of transient viscoelastic flows at low reynolds number. *Journal of Non-Newtonian Fluid Mechanics*, 132(1-3):61–72.
- Español, P. (1995). Hydrodynamics from dissipative particle dynamics. *Physical Review E*, 52:1734–1742.
- Español, P. (1997). Dissipative particle dynamics with energy conservation. *EPL (Europhysics Letters)*, 40:631–636.
- Español, P. and Revenga, M. (2003). Smoothed dissipative particle dynamics. *Physical Review E*, 67:026705.
- Español, P. and Warren, P. (1995). Statistical mechanics of dissipative particle dynamics. *Europhysics Letters*, 30:191–196.
- Español, P. and Warren, P. B. (2017). Perspective: Dissipative particle dynamics. *The Journal of Chemical Physics*, 146:150901.
- Fan, X., Phan-Thien, N., Chen, S., Wu, X., and Ng, T. Y. (2006). Simulating flow of dna suspension using dissipative particle dynamics. *Physics of Fluids*, 18:063102.
- Fan, X.-J., Phan-Thien, N., and Zheng, R. (1999). Simulation of fibre suspension flows by the brownian configuration field method. *Journal of Non-Newtonian Fluid Mechanics*, 84:257–274.
- Feng, Y. H., Zhang, X. P., Zhao, Z. Q., and Guo, X. D. (2020). Dissipative particle dynamics aided design of drug delivery systems: a review. *Molecular Pharmaceutics*, 17(6):1778–1799.
- Foss, D. R. and Brady, J. F. (2000). Structure, diffusion and rheology of brownian suspensions by stokesian dynamics simulation. *Journal of Fluid Mechanics*, 407:167–200.
- Frisch, U., Hasslacher, B., and Pomeau, Y. (1986). Lattice-gas automata for the navier-stokes equation. *Physical Review Letters*, 56:1505–1508.
- Füchslin, R. M., Fellermann, H., Eriksson, A., and Ziock, H.-J. (2009). Coarse graining and scaling in dissipative particle dynamics. *Journal of Chemical Physics*, 130:214102.

- Galvin, C., Grimes, R., and Burr, P. (2021). A molecular dynamics method to identify the liquidus and solidus in a binary phase diagram. *Computational Materials Science*, 186:110016.
- Ganesan, A., Coote, M. L., and Barakat, K. (2017). Molecular dynamics-driven drug discovery: leaping forward with confidence. *Drug discovery today*, 22(2):249–269.
- Gavrilov, A., Chertovich, A., and Kramarenko, E. Y. (2016). Dissipative particle dynamics for systems with high density of charges: Implementation of electrostatic interactions. *The Journal of chemical physics*, 145(17):174101.
- Gavrilov, A. A. (2020). Dissipative particle dynamics for systems with polar species: Interactions in dielectric media. *The Journal of Chemical Physics*, 152(16):164101.
- Gibson, T. H., McRae, A. T., Cotter, C. J., Mitchell, L., and Ham, D. A. (2019). *Compatible Finite Element Methods for Geophysical Flows: Automation and Implementation Using Firedrake*. Springer Nature.
- Girifalco, L. A. (2000). *Statistical Mechanics of Solids*. Monographs on the physics and chemistry of materials 58. Oxford University Press.
- Glowinski, R., Pan, T.-W., Hesla, T. I., Joseph, D. D., and Periaux, J. (2001). A fictitious domain approach to the direct numerical simulation of incompressible viscous flow past moving rigid bodies: application to particulate flow. *Journal of Computational Physics*, 169(2):363–426.
- Gottlieb, D. and Orszag, S. A. (1977). *Numerical analysis of spectral methods: theory and applications*. SIAM.
- Gregor, D., Moczo, P., Kristek, J., Mesgouez, A., Lefeuvre-Mesgouez, G., and Kristekova, M. (2021). Subcell-resolution finite-difference modelling of seismic waves in biot and jkd poroelastic media. *Geophysical Journal International*, 224(2):760–794.
- Groot, R. and Rabone, K. (2001). Mesoscopic simulation of cell membrane damage, morphology change and rupture by nonionic surfactants. *Biophysical Journal*, 81:725–736.
- Groot, R. and Warren, P. (1997). Dissipative particle dynamics: Bridging the gap between atomistic and mesoscopic simulation. *Journal of Chemical Physics*, 107:4423–4435.
- Groot, R. D. (2012). How to impose stick boundary conditions in coarse-grained hydrodynamics of brownian colloids and semi-flexible fiber rheology. *Journal of Chemical Physics*, 136:064901.

- Gu, Y., Qu, W., Chen, W., Song, L., and Zhang, C. (2019). The generalized finite difference method for long-time dynamic modeling of three-dimensional coupled thermoelasticity problems. *Journal of Computational Physics*, 384:42–59.
- Guo, X., Li, Y., and Wang, H. (2018). A high order finite difference method for tempered fractional diffusion equations with applications to the cgmy model. *SIAM Journal on Scientific Computing*, 40(5):A3322–A3343.
- Gwinner, J. and Stephan, E. P. (2018). *Advanced boundary element methods*. Springer.
- Habasaki, J. (2020). *Molecular Dynamics of Nanostructures and Nanoionics: Simulations in Complex Systems*. CRC Press.
- Hansen, J.-P. and McDonald, I. (2006). *Theory of Simple Liquids*. Academic Press, 3 edition.
- Hasimoto, H. (1959). On the periodic fundamental solutions of the stokes equations and their application to viscous flow past a cubic array of spheres. *Journal of Fluid Mechanics*, 5:317–328.
- Hernández, E. R. (2008). Molecular dynamics: from basic techniques to applications (a molecular dynamics primer). In *AIP Conference Proceedings*, volume 1077, pages 95–123. American Institute of Physics.
- Herrmann, H. J. (1999). The importance of computer simulations of granular flow. *Computing in Science and Engineering*, 1:72–73.
- Hess, B. (2002). Determining the shear viscosity of model liquids from molecular dynamics simulations. *Journal of Chemical Physics*, 116:209–217.
- Higuera, F. J. and Jiménez, J. (1989). Boltzmann approach to lattice gas simulations. *EPL (Europhysics Letters)*, 9(7):663.
- Hoogerbrugge, P. and Koelman, J. (1992). Simulating microscopic hydrodynamic phenomena with dissipative particle dynamics. *Europhysics Letters*, 19:155–160.
- Hrennikoff, A. (1941). Solution of problems of elasticity by the framework method. *Journal of Applied Mechanics*, 8:169–175.
- Hu, H. H. (1996). Direct simulation of flows of solid-liquid mixtures. *International Journal of Multiphase Flow*, 22(2):335–352.
- Huang, J., McGlinchey, D., Chen, Y., and McMahon, D. (2021). Cross-scale analysis of nickel superalloy fatigue using markov state model-molecular dynamics method. *Materials & Design*, 197:109226.

- Irving, J. H. and Kirkwood, J. G. (1950). The statistical mechanical theory of transport processes. iv. the equations of hydrodynamics. *Journal of Chemical Physics*, 18:817.
- Jamali, S., Armstrong, R. C., and McKinley, G. H. (2019). Multiscale nature of thixotropy and rheological hysteresis in attractive colloidal suspensions under shear. *Physical Review Letters*, 123(24):248003.
- Jamali, S., Boromand, A., Wagner, N., and Maia, J. (2015). Microstructure and rheology of soft to rigid shear-thickening colloidal suspensions. *Journal of Rheology*, 59(6):1377–1395.
- Jamali, S., McKinley, G. H., and Armstrong, R. C. (2017). Microstructural rearrangements and their rheological implications in a model thixotropic elastoviscoplastic fluid. *Physical review letters*, 118(4):048003.
- Jamelot, A., Gailler, A., Heinrich, P., Vallage, A., and Champenois, J. (2019). Tsunami simulations of the sulawesi m w 7.5 event: Comparison of seismic sources issued from a tsunami warning context versus post-event finite source. *Pure and Applied Geophysics*, 176(8):3351–3376.
- Jameson, A. and Caughey, D. A. (1977). A finite volume method for transonic potential flow calculations. In *3rd Computational Fluid Dynamics Conference*, pages 35–54.
- Jiang, W., Huang, J., Yongmei, W., and Laradji, M. (2007). Hydrodynamic interaction in polymer solutions simulated with dissipative particle dynamics. *Journal of Chemical Physics*, 126:044901.
- Kabedev, A., Hossain, S., Hubert, M., Larsson, P., and Bergström, C. A. (2021). Molecular dynamics simulations reveal membrane interactions for poorly water-soluble drugs: impact of bile solubilization and drug aggregation. *Journal of Pharmaceutical Sciences*, 110(1):176–185.
- Kamberaj, H. (2020). *Molecular Dynamics Simulations in Statistical Physics: Theory and Applications*. Springer.
- Kempe, T. and Hantsch, A. (2017). Large-eddy simulation of indoor air flow using an efficient finite-volume method. *Building and Environment*, 115:291–305.
- Kim, J. M. and Phillips, R. J. (2004). Dissipative particle dynamics simulation of flow around spheres and cylinders at finite reynolds numbers. *Chemical Engineering Science*, 59:4155–4168.
- Kirkup, S. M. (2007). *The boundary element method in acoustics*. Integrated sound software.

- Kitamura, K. (2020). *Advancement of Shock Capturing Computational Fluid Dynamics Methods: Numerical Flux Functions in Finite Volume Method*. Springer Nature.
- Kobayashi, Y. and Arai, N. (2018). Janus or homogeneous nanoparticle mediated self-assembly of polymer electrolyte fuel cell membranes. *RSC advances*, 8(33):18568–18575.
- Koelman, J. M. V. A. and Hoogerbrugge, P. J. (1993). Dynamic simulations of hard-sphere suspensions under steady shear. *Europhysics Letters*, 21:363–368.
- Kong, Y., Manke, C. W., Madden, W. G., and Schlijper, A. G. (1997). Effect of solvent quality on the conformation and relaxation of polymers via dissipative particle dynamics. *Journal of Chemical Physics*, 107:592.
- Ladd, A. (1994). Numerical simulations of particulate suspensions via a discretized boltzmann equation. part 1. theoretical foundation. *Journal of Fluid Mechanics*, 271:285.
- Laradji, M. and Hore, M. J. A. (2004). Nanospheres in phase-separating multi-component fluids: A three-dimensional dissipative particle dynamics simulation. *Journal of Chemical Physics*, 121:10641.
- Lavagnini, E., Cook, J. L., Warren, P. B., Williamson, M. J., and Hunter, C. A. (2020). A surface site interaction point method for dissipative particle dynamics parametrization: Application to alkyl ethoxylate surfactant self-assembly. *The Journal of Physical Chemistry B*, page 5047–5055.
- Le-Cao, K., Phan-Thien, N., Khoo, B., and Mai-Duy, N. (2017). A dissipative particle dynamics model for thixotropic materials exhibiting pseudo-yield stress behaviour. *Journal of Non-Newtonian Fluid Mechanics*.
- Lenzi, V., Ramos, M. M., and Marques, L. S. (2020). Dissipative particle dynamics simulations of end-cross-linked nanogels. *Molecular Simulation*, pages 1–10.
- LeVeque, R. J. (2002). *Finite Volume Methods for Hyperbolic Problems*. Cambridge texts in applied mathematics. Cambridge University Press, 1 edition.
- Li, Z., Hu, G.-H., Wang, Z.-L., Ma, Y.-B., and Zhou, Z.-W. (2013). Three dimensional flow structures in a moving droplet on substrate: A dissipative particle dynamics study. *Physics of Fluids*, 25:072103.
- Lindeberg, L., Rydin, Y. L., and Watson, L. M. (2021). A high-order finite-difference scheme to model the fluid-structure interaction in pneumatic seismic sources. *Journal of Computational Physics*, 424:109849.

- Lísal, M., Larentzos, J. P., Sellers, M. S., Schweigert, I. V., and Brennan, J. K. (2019). Dissipative particle dynamics with reactions: Application to rdx decomposition. *The Journal of Chemical Physics*, 151(11):114112.
- Litvinov, S., Ellero, M., Hu, X., and Adams, N. A. (2008). Smoothed dissipative particle dynamics model for polymer molecules in suspension. *Physical Review E*, 77:066703.
- Liu, H., Qian, H.-J., Zhao, Y., and Lu, Z.-Y. (2007). Dissipative particle dynamics simulation study on the binary mixture phase separate coupled with polymerization. *Journal of Chemical Physics*, 127:144903.
- Liu, M. B. and Liu, G. R. (2016). *Particle methods for multi-scale and multi-physics*, volume 400. World Scientific.
- Liu, M. B., Liu, G. R., Zhou, L. W., and Chang, J. Z. (2015). Dissipative particle dynamics (dpd): An overview and recent developments. *Archives of Computational Methods in Engineering*, 22:529–556.
- Liu, X., Feng, X., Xiang, C., and Shen, F. (2019). Hyperbolic cell-centered finite volume method for obtaining potential magnetic field solutions. *The Astrophysical Journal*, 887(1):33.
- Lu, C., Yang, Z., Bai, J., Cao, Y., and He, X. (2020). Three-dimensional immersed finite-element method for anisotropic magnetostatic/electrostatic interface problems with nonhomogeneous flux jump. *International Journal for Numerical Methods in Engineering*, 121(10):2107–2127.
- Luckhurst, G. R. and Veracini, C. A. (2012). *The molecular dynamics of liquid crystals*, volume 431. Springer Science & Business Media.
- Ludwig, A., Kharicha, A., Hölzl, C., Domitner, J., Wu, M., and Pusztai, T. (2014). 3d lattice boltzmann flow simulations through dendritic mushy zones. *Engineering Analysis with Boundary Elements*, 45:29–35.
- Ma, J., Dudeja, R., Xu, J., Maleki, A., and Wang, X. (2021). Spectral method for phase retrieval: an expectation propagation perspective. *IEEE Transactions on Information Theory*, 67(2):1332–1355.
- Mai-Duy, N., Nguyen, T. Y. N., Le-Cao, K., and Phan-Thien, N. (2020). Investigation of particulate suspensions in generalised hydrodynamic dissipative particle dynamics using a spring model. *Applied Mathematical Modelling*, pages 652–662.
- Mai-Duy, N., Pan, D., Phan-Thien, N., and Khoo, B. C. (2013). Dissipative particle dynamics modelling of low reynolds number incompressible flows. *Journal of Rheology*, 57:585.

- Mai-Duy, N., Phan-Thien, N., and Khoo, B. (2015). Investigation of particles size effects in dissipative particle dynamics (DPD) modelling of colloidal suspensions. *Computer Physics Communications*, 189:37–46.
- Mai-Duy, N., Phan-Thien, N., and Tran-Cong, T. (2017a). Imposition of physical parameters in dissipative particle dynamics. *Computer Physics Communications*, 221:290–298.
- Mai-Duy, N., Phan-Thien, N., and Tran-Cong, T. (2017b). An improved dissipative particle dynamics scheme. *Applied Mathematical Modelling*, 46:602–617.
- Mall-Gleissle, S. E., Gleissle, W., McKinley, G. H., and Buggisch, H. (2002). The normal stress behaviour of suspensions with viscoelastic matrix fluids. *Rheologica acta*, 41(1-2):61–76.
- Marsh, C. (1998). *Theoretical Aspects of Dissipative Particle Dynamics*. PhD thesis, University of Oxford.
- Marsh, C., Backx, G., and Ernst, M. (1997). Static and dynamic properties of dissipative particle dynamics. *Physical Review E*, 56:1676–1691.
- Martys, N. S. (2005). Study of a dissipative particle dynamics based approach for modeling suspensions. *Journal of Rheology*, 49:401.
- Mazhdraikov, M., Benov, D., and Valkanov, N. (2018). *The Monte Carlo method: engineering applications*. ACMO Academic Press.
- McCammon, J. A., Gelin, B. R., and Karplus, M. (1977). Dynamics of folded proteins. *Nature*, 267(5612):585–590.
- McNamara, G. R. and Zanetti, G. (1988). Use of the boltzmann equation to simulate lattice-gas automata. *Physical review letters*, 61(20):2332.
- Metropolis, N., Rosenbluth, A. W., Rosenbluth, M. N., Teller, A. H., and Teller, E. (1953). Equation of state calculations by fast computing machines. *The journal of chemical physics*, 21(6):1087–1092.
- Metzner, A. B. (1985). Rheology of suspensions in polymeric liquids. *Journal of Rheology*, 29:739.
- Mewis, J. and Wagner, N. J. (2012). *Colloidal suspension rheology*. Cambridge University Press.
- Minkara, M. S., Hembree, R. H., Jamadagni, S. N., Ghobadi, A. F., Eike, D. M., and Siepmann, J. I. (2019). A new equation of state for homo-polymers in dissipative particle dynamics. *The Journal of chemical physics*, 150(12):124104.
- Mordechai, S. (2011). *Applications of Monte Carlo method in science and engineering*.

- Morin, R. L. (2019). *Monte Carlo simulation in the radiological sciences*. CRC Press.
- Mulligan, R., Franci, A., Celigueta, M., and Take, W. (2020). Simulations of landslide wave generation and propagation using the particle finite element method. *Journal of Geophysical Research: Oceans*, 125(6):e2019JC015873.
- Nie, Q., Zhong, Y., and Fang, H. (2019). Study of a nanodroplet breakup through many-body dissipative particle dynamics. *Physics of Fluids*, 31(4):042007.
- Nikunen, P., Vattulainen, I., and Karttunen, M. (2007). Reptational dynamics in dissipative particle dynamics simulations of polymer melts. *Physical Review E*, 75:036713.
- Novik, L. and Coveney, P. (1997). Using dissipative particle dynamics to model binary immiscible fluids. *International Journal of Modern Physics C*, 08:909–918.
- Özişik, M. N., Orlande, H. R., Colaço, M. J., and Cotta, R. M. (2017). *Finite difference methods in heat transfer*. CRC press.
- Pagonabarraga, I. and Frenkel, D. (2001). Dissipative particle dynamics for interacting systems. *Journal of Chemical Physics*, 115:5015–5026.
- Palkar, V., Choudhury, C. K., and Kuksenok, O. (2020). Development of dissipative particle dynamics framework for modeling hydrogels with degradable bonds. *MRS Advances*, pages 1–8.
- Palmer, B. J. (1994). Transverse-current autocorrelation-function calculations of the shear viscosity for molecular liquids. *Physical Review E*, 49:359–366.
- Pan, D., Phan-Thien, N., Mai-Duy, N., and Khoo, B. C. (2013). Numerical investigations on the compressibility of a dpd fluid. *Journal of Computational Physics*, 242:196–210.
- Pan, W., Caswell, B., and Karniadakis, G. E. (2010a). A low-dimensional model for the red blood cell. *Langmuir*, 6:4366–4376.
- Pan, W., Caswell, B., and Karniadakis, G. E. (2010b). Rheology, microstructure and migration in brownian colloidal suspensions. *Langmuir*, 26:133–142.
- Pan, W., Pivkin, I. V., and Karniadakis, G. E. (2008). Single-particle hydrodynamics in dpd: A new formulation. *Europhysics Letters*, 84:10012.
- Panchenko, A., Hinz, D. F., and Fried, E. (2018). Spatial averaging of a dissipative particle dynamics model for active suspensions. *Physics of Fluids*, 30:033301.

- Panoukidou, M., Wand, C. R., Del Regno, A., Anderson, R. L., and Carbone, P. (2019). Constructing the phase diagram of sodium laurylethoxysulfate using dissipative particle dynamics. *Journal of colloid and interface science*, 557:34–44.
- Petrova, R. (2012). *Finite volume method : powerful means of engineering design*. InTech.
- Phan-Thien, N. and Mai-Duy, N. (2017). *Understanding Viscoelasticity: An Introduction to Rheology*. Springer, 3 edition.
- Phan-Thien, N., Mai-Duy, N., and Khoo, B. (2014a). A spring model for suspended particles in dissipative particle dynamics. *Journal of Rheology*, 58:839–867.
- Phan-Thien, N., Mai-Duy, N., and Nguyen, T. Y. N. (2018). A note on dissipative particle dynamics (dpd) modelling of simple fluids. *Computers and Fluids*, page S0045793018305784.
- Phan-Thien, N., Mai-Duy, N., Pan, D., and Khoo, B. (2014b). Exponential-time differencing schemes for low-mass dpd systems. *Computer Physics Communications*, 185:229–235.
- Pryamitsyn, V. and Ganesan, V. (2005). A coarse-grained explicit solvent simulation of rheology of colloidal suspensions. *Journal of Chemical Physics*, 122:104906.
- Rahman, A. (1964). Correlations in the motion of atoms in liquid argon. *Physical review*, 136(2A):A405.
- Rao, S. S. (2018). *The finite element method in engineering*. Elsevier, 6. ed edition.
- Rapaport, D. C. (2004). *The art of molecular dynamics simulation*. Cambridge University Press, 2 edition.
- Reddy, J. N. and Gartling, D. K. (2010). *The finite element method in heat transfer and fluid dynamics*. CRC press.
- Reichl, L. (2016). *A Modern Course in Statistical Physics*. Wiley-Vch, 4 edition.
- Ripoll, M., Ernst, M. H., and Español, P. (2001). Large scale and mesoscopic hydrodynamics for dissipative particle dynamics. *Journal of Chemical Physics*, 115:7271–7284.
- Rizzi, A. (1976). Transonic solutions of the euler equations by the finite volume method. In *Symposium Transsonicum II*, pages 567–574. Springer Verlag.

- Rong, F. M., Guo, Z. L., Lu, J. H., and Shi, B. C. (2011). Numerical simulation of the flow around a porous covering square cylinder in a channel via lattice boltzmann method. *International Journal for Numerical Methods in Fluids*, 65:1217–1230.
- Sato, A. (2010). *Introduction to practice of molecular simulation : Molecular dynamics, Monte Carlo, Brownian dynamics, Lattice Boltzmann, dissipative particle dynamics*. Elsevier.
- Schröder, J. and de Mattos Pimenta, P. (2020). *Novel Finite Element Technologies for Solids and Structures*. Springer.
- Seco, J. and Verhaegen, F. (2013). *Monte Carlo techniques in radiation therapy*. CRC press.
- Sengupta, S. and Lyulin, A. (2020). Dissipative particle dynamics modeling of polyelectrolyte membrane–water interfaces. *Polymers*, 12(4):907.
- Separdar, L., Rino, J. P., and Zanutto, E. D. (2021). Molecular dynamics simulations of spontaneous and seeded nucleation and theoretical calculations for zinc selenide. *Computational Materials Science*, 187:110124.
- Sivadasan, V., Lorenz, E., Hoekstra, A. G., and Bonn, D. (2019). Shear thickening of dense suspensions: The role of friction. *Physics of Fluids*, 31(10):103103.
- Song, X., Bao, B., Tao, J., Zhao, S., Han, X., and Liu, H. (2018). Deswelling dynamics of thermoresponsive microgel capsules and their ultrasensitive sensing applications: a mesoscopic simulation study. *The Journal of Physical Chemistry C*, 123(3):1828–1838.
- Sowers, T., Yoon, H., and Emelianov, S. (2020). Investigation of light delivery geometries for photoacoustic applications using monte carlo simulations with multiple wavelengths, tissue types, and species characteristics. *Journal of biomedical optics*, 25(1):016005.
- Spaid, M. A. A. and Phelan, F. R. (1997). Lattice boltzmann methods for modeling microscale flow in fibrous porous media. *Physics of Fluids*, 9:2468–2474.
- Stillinger, F. H. and Rahman, A. (1974). Improved simulation of liquid water by molecular dynamics. *The Journal of Chemical Physics*, 60(4):1545–1557.
- Sun, D., Pan, S., Han, Q., and Sun, B. (2016). Numerical simulation of dendritic growth in directional solidification of binary alloys using a lattice boltzmann scheme. *International Journal of Heat and Mass Transfer*, 103:821–831.
- Tanner, R. I. (2000). *Engineering rheology*, volume 52. OUP Oxford.
- Telles, J. C. F. (2012). *The boundary element method applied to inelastic problems*, volume 1. Springer Science & Business Media.

- Terekhov, K. M. and Vassilevski, Y. V. (2019). Finite volume method for coupled subsurface flow problems, i: Darcy problem. *Journal of Computational Physics*, 395:298–306.
- Tran, C.-D., Le-Cao, K., Bui, T. T., et al. (2019). Dielectrophoresis can control the density of cnt membranes as confirmed by experiment and dissipative particle simulation. *Carbon*, 155:279–286.
- Vaiwala, R., Jadhav, S., and Thaokar, R. (2019). Establishing an electrostatics paradigm for membrane electroporation in the framework of dissipative particle dynamics. *Journal of chemical theory and computation*, 15(10):5737–5749.
- Vakhrushev, A. (2018). *Molecular Dynamics*. BoD–Books on Demand.
- van de Meent, J.-W., Morozov, A., Somfai, E., Sultan, E., and van Saarloos, W. (2008). Coherent structures in dissipative particle dynamics simulations of the transition to turbulence in compressible shear flows. *Physical Review E*, 78:015701.
- Vázquez-Cendón, M. E. (2015). *Solving hyperbolic equations with finite volume methods*, volume 90. Springer.
- Vázquez-Quesada, A., Ellero, M., and Español, P. (2009). Consistent scaling of thermal fluctuations in smoothed dissipative particle dynamics. *Journal of Chemical Physics*, 130:034901.
- Venable, R. M., Krämer, A., and Pastor, R. W. (2019). Molecular dynamics simulations of membrane permeability. *Chemical reviews*, 119(9):5954–5997.
- Vogelsang, R. and Hoheisel, C. (1987). Computation and analysis of the transverse current autocorrelation function, $C_t(k,t)$, for small wave vectors: A molecular-dynamics study for a lennard-jones fluid. *Phys Rev A*, 35:1786–1794.
- Waheed, W., Alazzam, A., Al-Khateeb, A. N., and Abu-Nada, E. (2020). Dissipative particle dynamics for modeling micro-objects in microfluidics: application to dielectrophoresis. *Biomechanics and Modeling in Mechanobiology*, 19(1):389–400.
- Wang, K., Peng, S., Lu, Y., and Cui, X. (2020a). The velocity-stress finite-difference method with a rotated staggered grid applied to seismic wave propagation in a fractured medium. *Geophysics*, 85(2):T89–T100.
- Wang, L. (2012). *Molecular dynamics: theoretical developments and applications in nanotechnology and energy*. BoD–Books on Demand.
- Wang, M., Jamali, S., and Brady, J. F. (2020b). A hydrodynamic model for discontinuous shear-thickening in dense suspensions. *Journal of Rheology*, 64:379–394.

- Wang, Y., Gu, Y., and Liu, J. (2020c). A domain-decomposition generalized finite difference method for stress analysis in three-dimensional composite materials. *Applied Mathematics Letters*, 104:106226.
- Wang, Y., Li, Z., Ouyang, J., and Karniadakis, G. E. (2020d). Controlled release of entrapped nanoparticles from thermoresponsive hydrogels with tunable network characteristics. *Soft Matter*, page 10.1039.D0SM00207K.
- Whittle, M. and Travis, K. P. (2010). Dynamic simulations of colloids by core-modified dissipative particle dynamics. *Journal of Chemical Physics*, 132:124906.
- Yamamoto, K. and Takada, N. (2006). Lb simulation on soot combustion in porous media. *Physica A: Statistical Mechanics and its Applications*, 362(1):111–117.
- Yang, Z. L., Dinh, T., Nourgaliev, R., and Sehgal, B. (2000). Numerical investigation of bubble coalescence characteristics under nucleate boiling condition by a lattice-boltzmann model. *International Journal of Thermal Sciences*, 39:1–17.
- Ye, T., Phan-Thien, N., Khoo, B. C., and Lim, C. T. (2013). Stretching and relaxation of malaria-infected red blood cells. *Biophysical Journal*, 105:1103–1109.
- Ye, T., Phan-Thien, N., Khoo, B. C., and Lim, C. T. (2014). Dissipative particle dynamics simulations of deformation and aggregation of healthy and diseased red blood cells in a tube flow. *Physics of Fluids*, 26:111902.
- Yu, X., Jin, Y., Du, L., Sun, M., Wang, J., Li, Q., Zhang, X., Gao, Z., and Ding, P. (2018). Transdermal cubic phases of metformin hydrochloride: In silico and in vitro studies of delivery mechanisms. *Molecular Pharmaceutics*, 15(8):3121–3132.
- Zhang, J., Xu, J., Wen, L., Zhang, F., and Zhang, L. (2020). The self-assembly behavior of polymer brushes induced by the orientational ordering of rod backbones: a dissipative particle dynamics study. *Physical Chemistry Chemical Physics*, 22(9):5229–5241.
- Zhou, B., Luo, W., Yang, J., Duan, X., Wen, Y., Zhou, H., Chen, R., and Shan, B. (2017). Simulation of dispersion and alignment of carbon nanotubes in polymer flow using dissipative particle dynamics. *Computational Materials Science*, 126:35–42.
- Zienkiewicz, O. C. and Taylor, R. L. (2000a). *The finite element method*, volume Volume 1 of *Finite Element Method Ser.* Butterworth-Heinemann, 5th ed edition.

- Zienkiewicz, O. C. and Taylor, R. L. (2000b). *The finite element method*, volume Volume 2 of *Finite Element Method Ser.* Butterworth-Heinemann, 5th ed edition.
- Zienkiewicz, O. C. and Taylor, R. L. (2000c). *The finite element method*, volume Volume 3. Butterworth-Heinemann, 5th ed edition.
- Zienkiewicz, O. C., Taylor, R. L., and (Auth.), D. F. (2014). *The Finite Element Method for Solid and Structural Mechanics*. Butterworth-Heinemann, 7 edition.
- Zienkiewicz, O. C., Taylor, R. L., and (Auth.), P. N. (2013). *The Finite Element Method for Fluid Dynamics*. Butterworth-Heinemann, 7 edition.